Electronic Theses and Dissertations

Theses, Dissertations, and Major Papers

1986

VACUUM ULTRA-VIOLET STUDIES USING ELECTRON IMPACT EXCITATION.

JOHN LUC MACGREGOR. FORAND
University of Windsor

Follow this and additional works at: https://scholar.uwindsor.ca/etd

CANADIAN THESES

THÈSES CANADIENNES

NOTICE

The quality of this microfiche is heavily dependent upon the quality of the original thesis submitted for microfilming. Every effort has been made to ensure the highest quality of reproduction possible.

If pages are missing, contact the university which granted the degree.

Some pages may have indistinct print especially if the original pages were typed with a poor typewriter ribbon or if the university sent us an inferior photocopy.

Previously copyrighted materials (journal articles, published tests, etc.) are not filmed.

Reproduction in full or in part of this film is governed by the Canadian Copyright Act, R.S.C. 1970, c. C-30.

AVIS

La qualité de cette microfiche dépend grandement de la qualité de la thèse soumise au microfilmage. Nous avons tout fait pour assurer une qualité supérieure de reproduction.

S'il manque des pages, veuillez communiquer avec l'université qui a conféré le grade.

La qualité d'impression de certaines pages peut laisser à désirer, surtout si les pages originales ont été dactylographiées à l'aide d'un ruban usé ou si l'université nous a fait parvenir une photocopie de qualité inférieure.

Les documents qui font déjà l'objet d'un droit d'auteur (articles de revue, examens publiés, etc.) ne sont pas microfilmés.

La reproduction, même partielle, de ce microfilm est soumise à la Loi canadienne sur le droit d'auteur, SRC 1970, c. C-30.

THIS DISSERTATION
HAS BEEN MICROFILMED
EXACTLY AS RECEIVED

LA THÈSE A ÉTÉ
MICROFILMÉE TELLE QUE
NOUS L'AVONS REÇUE

Canada

VACUUM ULTRA-VIOLET STUDIES

USING

ELECTRON IMPACT EXCITATION

by

© John Luc MacGregor Porand

A Dissertation
presented to the University of Windsor
in partial fulfillment of the
thesis requirement for the degree of
Doctor of Philosophy
in
Physics

Windsor, Ontario, 1986

860576

ABSTRACT

This work presents emission cross sections following electron-impact on helium, hydrogen, sulfur hexafluoride, nitrogen, and argon. Specifically, we studied the following emissions. The He^+ 2p --> 1s 30.4 nm emission, the numerous emissions from the neutral and singly ionized atomic fragments of SF_6, the 120 nm emission from N_2, and the Lyman series emissions from both atomic and molecular hydrogen. The most important aspect of the hydrogen work was the determination of the H_2 Lyman alpha emission cross section. Use of the Lyman series from atomic hydrogen for the calibration of optical equipment in the 90 to 122 nm region was also investigated. To illustrate the technique, emission cross sections of the argon resonance lines near 105 nm and the argon ion lines near 93 nm were determined. Excitation functions for the He^+ 30.4 nm emission and for various fluorine and sulfur emissions (along with some appearance potentials) were also obtained.

A value of $(7.5 \pm 1.6) \times 10^{-19}$ cm^2 at 200 eV is found for the He^+ 30.4 nm transition. For the dissociative excitation of SF_6 the largest emission cross sections belonged to the FI transitions at 95.5 nm $(2.03 \times 10^{-18}$ cm^2 at 200 eV) and 97.5 nm $(1.46 \times 10^{-18}$ cm^2 at 200 eV). The maximum

SI and SII emission cross sections are approximately 1×10^{-19} cm^2 and the strongest PII emission cross sections are approximately 1×10^{-20} cm^2. The NI 120 nm emission cross section is $(2.98 \pm 0.36) \times 10^{-18}$ cm^2. Our value for the H_2 Lyman alpha emission cross section is $(7.08 \pm 0.58) \times 10^{-18}$ cm^2 at 100 eV. The emission cross sections for the argon resonance lines at 104.8 nm and 106.7 nm are $(12.8 \pm 1.3) \times 10^{-18}$ cm^2 and $(5.5 \pm 0.8) \times 10^{-18}$ cm^2 respectively. For the argon ion lines at 92 nm and 93.5 nm they are $(5.6 \pm 0.5) \times 10^{-18}$ cm^2 and $(2.3 \pm 0.2) \times 10^{-18}$ cm^2 respectively.

ACKNOWLEDGEMENTS

CONTENTS

FIGURES

TABLES

Chapter I

INTRODUCTION

.This thesis presents several studies regarding the emission of vacuum ultraviolet (V.U.V.) radiation from atoms and molecules following their impact with nearly monoenergetic electrons. More precisely, a beam of atoms or molecules is formed by allowing a gas to flow through either a single or multi-capillary orifice. The electron beam is formed using a conventional electron gun and intersects the gas beam at right angles. The emitted radiation is detected in a direction perpendicular to both beams either before or after it is dispersed by a 0.5 m Seya-Namioka mounted monochromator. With this set-up (see Figure 3) one can perform several fundamental studies such as identifying the V.U.V. spectrum for a given gas, determining individual emission cross sections, or measuring excitation functions.

We have used the apparatus to study the following interactions

1. $e^- + He \longrightarrow He^{+*} + 2e^- \longrightarrow He^+ + photon$

2. $e^- + SF_6 \longrightarrow$ excited fragments of $SF_6 + e^-$

3. $e^- + N_2 \longrightarrow N + N^* + e^- \longrightarrow 2N + e^- + photon$

4. $e^- + H \longrightarrow H^* + e^- \longrightarrow H + photons$

5. $e^- + H_2 \longrightarrow H_2^* + e^- \longrightarrow H_2 + photons$

$$\text{--> } H + H^* + e^- \text{ --> } 2H + \text{photons}$$

6. $$e^- + Ar \text{ --> } Ar^* + e^- \text{ --> } Ar + \text{photon}$$

$$\text{--> } Ar^{+*} + 2e^- \text{ --> } Ar^+ + e^- + \text{photon}$$
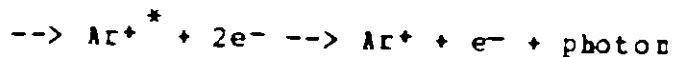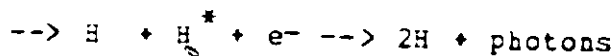
Interaction (1) involved measuring the absolute emission cross section of the He+ 30.4 nm 2^2P --> 1^2S transition following simultaneous ionization-excitation of He by electron impact for electron energies from threshold to 1000 eV. Since the process involves the simultaneous excitation of two atomic electrons, the theoretical treatment is complicated; consequently, few calculations have been performed. Previous work on He+ excitation has largely consisted of cross section and polarization measurements for the He+ n=4 to n=3 manifold at 468.6 nm. A summary of earlier results is given by Heddle and Keesing (1968)[37] and a more recent review by Shemansky et al (1984) [79]. Emission cross sections for the vacuum ultraviolet lines of He+ at 164.0 nm, 121.5 nm and 30.4 nm have been reported by Moustafa Moussa and de Heer (1967) [65]; however, since they estimated the quantum yield of their monochromator-detector system by extrapolation over tens of nanometers, their data at 164.0 and 30.4 nm is questionable. A later measurement by the same group (Bloemen et al 1981 [15]) of the 30.4 nm line using a photoionization chamber found a value 50% higher. The 30.4 nm line is of special interest since it represents the simplest case of simultaneous ionization-excitation by electron impact. Secondly the line is emitted

in the only optically allowed decay channel (2p --> 1s) and is therefore not affected by l-degeneracy. Thus the 30.4 nm line can provide a direct comparison between theory and experiment. It is also an important emission for the calibration of optical instrumentation in the far vacuum ultraviolet.

Interaction (2) involved the study of V.U.V emissions from 40.0 to 180.0 nm due to electron impact on sulfur hexafluoride (SF$_6$) over an electron energy range from threshold to 600 eV. The study of SF$_6$ is of interest due to its chemical and electrical properties. Chemically, it is similar to an inert gas and has a spherically symmetric appearance due to its octahedral structure where the S atom is at the center. Electrically, it is a superior insulator and is used in many high voltage devices. As a result, it has been studied by a variety of experimental techniques such as U.V. [52][70], V.U.V [14], X-ray [47] [48][97][105], photoelectron [31][75] [80], electron-impact [81] [90], and mass [24] spectroscopy. Several time-of-flight studies have also been performed [76] [20]. Theoretical work [35][36] [19][86] has been limited to understanding its electronic structure and its many vibrational modes. However, little effort has gone into investigating the dissociative mechanisms or its radiative emissions following electron impact. Such information should help to further understand the early stages of dielectric breakdown. Hopefully, our study of the production

of V.U.V. radiation from F, F+, S, and S+ atoms due to the dissociative excitation of SF_6 following electron impact will provide a basis for new studies on SF_6.

Interaction (3) was studied due to the importance of N_2 in planetary atmospheres, especially our own. Only the NI emission cross section following electron impact on N_2 at 120 nm is given due to its proximity to H_2 Lyman alpha. Our value for the cross section was determined using our new experimental value for the H_2 Lyman alpha cross section. A number of investigators have studied the emission. They include Aarts and de Heer [2], Mumma and Zipf [68], and Ajello and Shemansky [6].

Interactions (4) and (5) are of importance due to the use of the H_2 Lyman alpha emission from dissociative excitation following electron impact as a calibration standard for optical instruments in the V.U.V.. The H_2 Lyman alpha emission cross section for an electron impact energy of 100 eV has been measured several times. It was first studied experimentally by Fite and Brackmann (1958) [27] using a tungsten furnace to dissociate molecular hydrogen, a lithium fluoride window, and an oxygen filter. A later study by Long, Cox, and Smith (1968) [53] used a similar procedure. However, they did not employ an oxygen filter. The procedure involves using the Born approximation for the Lyman alpha emission cross section following electron impact on atomic hydrogen as a standard to which the H_2 Lyman alpha

cross section can be normalized. Due to the band-pass of both experiments, they actually measured the countable (CUV) radiation produced by molecular hydrogen, not just the Lyman alpha radiation. In 1971, Kauppila et al [43] redetermined the ratio of the CUV cross section at 100 eV to the cross section for excitation of Lyman alpha by 100 eV electron impact on atomic hydrogen. Their apparatus was similar to Fite and Brackmann's. They determined the ratio to be 4.05 ± 0.07. Using data from Carriere and de Heer [19] and McGowan and Williams [60], Mumma and Zipf (1971) [67] allowed that 80% ± 10% of the CUV radiation in the experiment of Kauppila et al was due to Lyman alpha. Allowing for the same polarization of the CUV radiation and of Lyman alpha radiation from atomic hydrogen (Ott et al [71]) and using the cross section for excitation of Lyman alpha on atomic hydrogen from Long, Cox and Smith (1968), Mumma and Zipf calculated the cross section for dissociative excitation of Lyman alpha by 100 eV electron impact to be 1.2 x 10^{-17} cm^2 ± 11%. Until recently it has been the accepted value. However, several recent results by Van Zyl et al (1985)[95], Ligtenberg et al (1985) [50][51], Ajello and Shemansky (1985)[4], Shemansky et al (1985) [78], and Woolsey et al (1986) [104] strongly indicate that the H$_2$ Lyman alpha cross section needs to be lowered by nearly 40%. These new results have used new data concerning the absorption properties of oxygen, models of the H$_2$ molecular spec-

.trum, and other optical calibration procedures for the V.U.V. such as employing a synchrotron radiation source. Due to our recent acquisition of an rf-discharge source (Slevin and Sterling , 1981 [82]) we are capable of performing a direct measurement of the H_2 Lyman alpha cross section by using the Lyman alpha cross section for atomic hydrogen as the primary standard. The advantage to our technique is that we do not have to employ either an oxygen filter or a lithium fluoride window. Instead, we disperse the radiation using a vacuum monochromator with which a FWHM of 0.1 nm is obtainable. In this way we can remove most of the molecular radiation from the Lyman alpha signals. Secondly, by measuring the amount of molecular radiation, with the discharge alternately on and off, the dissociation fraction for the discharge source can be accurately determined. Also, since identical source and detection geometries are used (discharge on or off) many of the systematic errors are automatically eliminated.

Interaction (6) was studied in order to determine the emission cross sections for the argon resonance lines and ion lines near 105 nm and 93 nm, respectively, for an electron impact energy of 200 eV using the Lyman beta and Lyman epsilon Born cross sections for atomic hydrogen as the primary standards. These cross sections are important for several reasons. Firstly, they are often used as secondary standards in the V.U.V.; consequently, reducing the present

uncertainties in their absolute cross sections is of vital
importance. Secondly, since Ar is one of the noble gases
its cross sections are important both theoretically and
experimentally in many branches of physics. Previous work
on the two resonance cross sections near 105 nm have been
performed by de Jongh (1971) [23], Ganas and Green (1971)
[30], McConkey and Donaldson (1973) [53], Mentall and and
Morgan [63], and Ajello (1984) [5]. The two ion lines near
93 nm have been investigated by McGuire (1971) [61], and Tan
et al (1974) [85].

Chapter II

THEORY

2.1   Electron-Atom(Molecule) Collisions

When electrons and ground state atoms interact many scattering channels are opened. The electrons can scatter elastically or inelastically. If they scatter inelastically energy will be transferred to the atom. At low electron impact energies the electron can be captured and at sufficiently high impact energies the atom may be excited or even ionized. At even higher energies the atoms may be both ionized and excited or even doubly or triply ionized.

$$
\begin{aligned}
e + A &\longrightarrow e + A \text{ (elastic process)} \\
&\qquad\qquad\qquad\qquad \text{(inelastic processes)} \\
&\longrightarrow A^- \text{ (electron capture)} \\
&\longrightarrow e + A^* \text{ (excitation)} \\
&\longrightarrow e + e + A^+ \text{ (ionization)} \\
&\longrightarrow e + e + A^{+*} \text{ (ionization-excitation)} \\
&\text{etc.}
\end{aligned}
$$
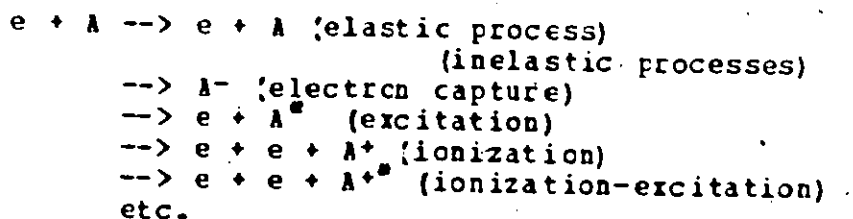
When electrons and molecules collide, additional scattering channels are available. The molecule may be electronically, vibrationally, or rotationally excited, or ionized, or dissociated. As well dissociation can be accompanied by excitation of the molecular fragments. Consider the case of a two atom molecule (AB). The following electron impact processes are possible:

```
e + AB --> e + AB  (elastic process)
                          (inelastic processes)
        -->  AB-  (electron capture)
        -->  e + AB*  (excitation)
        -->  e + e + AB+  (ionization)
        -->  e + A + B  (dissociation)
        -->  e + A + B*  (dissociative excitation)
        -->  2e + A + B+  (dissociative ionization)
        etc.
```
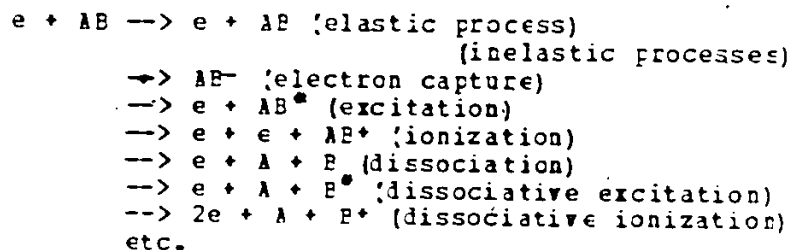
In the series of experiments to be discussed in this the-
sis we are only concerned with those collisions which
produce excitation. Several techniques are frequently
employed in order to study them. Two common techniques are
electron energy-loss spectroscopy and photon spectroscopy.
Only photon spectroscopy will be discussed.

2.2   Photon Spectroscopy

By studying the emission spectrum from an atom (molecule),
it is possible, in principle, to determine the cross sec-
tions for excitation to the different energy levels in the
atom (molecule). To accomplish this, it is necessary to mod-
el the process.

2.2.1   Excitation Cross-Section

Assume $n(j)$ is the number of excited atoms (molecules) in
the state j produced per unit volume by an electron beam.
Secondary processes such as collisional population and depo-
pulation, and resonance absorption can be neglected if one
works at sufficiently low gas pressures and electron cur-
rents. Under such conditions the following equation is val-
id.

$$dn(j)/dt = -n(j) \sum_{\substack{k \\ k<j}} A(jk) + NQ(j)vn_e + \sum_{\substack{i \\ i>j}} A(ij)n(i) \quad (1)$$

$A(ij)$ are the Einstein A coefficients for transitions from the i state to the j state, $Q(j)$ is the cross section for excitation to the j state, v is the electron velocity, n_e is the electron number density and N is the atom (molecule) number density. Thus equation (1) tells us that the rate of change of $n(j)$ is equal to the rate at which excited atoms (molecules) are leaving the state j through the emission of radiation (first term on the right), plus the rate at which atoms (molecules) are entering state j through the process of cascade (third term) plus the rate at which ground state atoms (molecules) are being excited to the j state by electron impact (second term). See Figure 1. In equilibrium, $dn(j)/dt = 0$, and equation (1) reduces to:

$$n(j) = [NQ(j)vn_e + \sum_{\substack{i \\ i>j}} A(ij)n(i)]/ \sum_{\substack{k \\ k<j}} A(jk) \quad (2)$$

Defining $J(jk)$ to be the rate at which atoms (molecules) in state j decay to state k per unit length of the electron beam, equation (2) can be written as:

$$J(jk) = [NQ(j)Svn_e + \sum_{\substack{i \\ i>j}} J(ij)]A(jk)/\sum_{\substack{k' \\ k'<j}} A(jk') \quad (3)$$

where S is the cross sectional area of the electron beam. Using

$$I = Sven_e \quad (4)$$

where I is the electron current and e the electron charge,
equation (3) can be written as:

$$J(jk) = [NQ(j)I/e + \sum_{\substack{i \\ i>j}} J(ij)]A(jk)/\sum_{\substack{k' \\ k'<j}} A(jk') \qquad (5)$$

In terms of the excitation cross section, $Q(j)$, equation (5)
becomes:

$$Q(j) = [J(jk)/B(jk) - \sum_{\substack{i \\ i>j}} J(ij)]e/IN \qquad (6)$$

where $\qquad B(jk) = A(jk)/\sum_{\substack{k' \\ k'<j}} A(jk') \qquad (7a)$

$$= J(jk)/\sum_{\substack{k' \\ k'<j}} J(jk') \qquad (7b)$$

$B(jk)$ is the branching ratio for the j-k transition. Thus,
if one measures the amount of radiation emitted in tran-
sitions to and from state j, the excitation cross section
$Q(j)$ can be determined.   Note that if cascade can be neg-
lected, then

$$Q(j) = J(jk)/B(jk) \times e/IN \qquad (8a)$$

$$= \sum_{\substack{k' \\ k'<j}} J(jk') \times e/IN \qquad (8b)$$
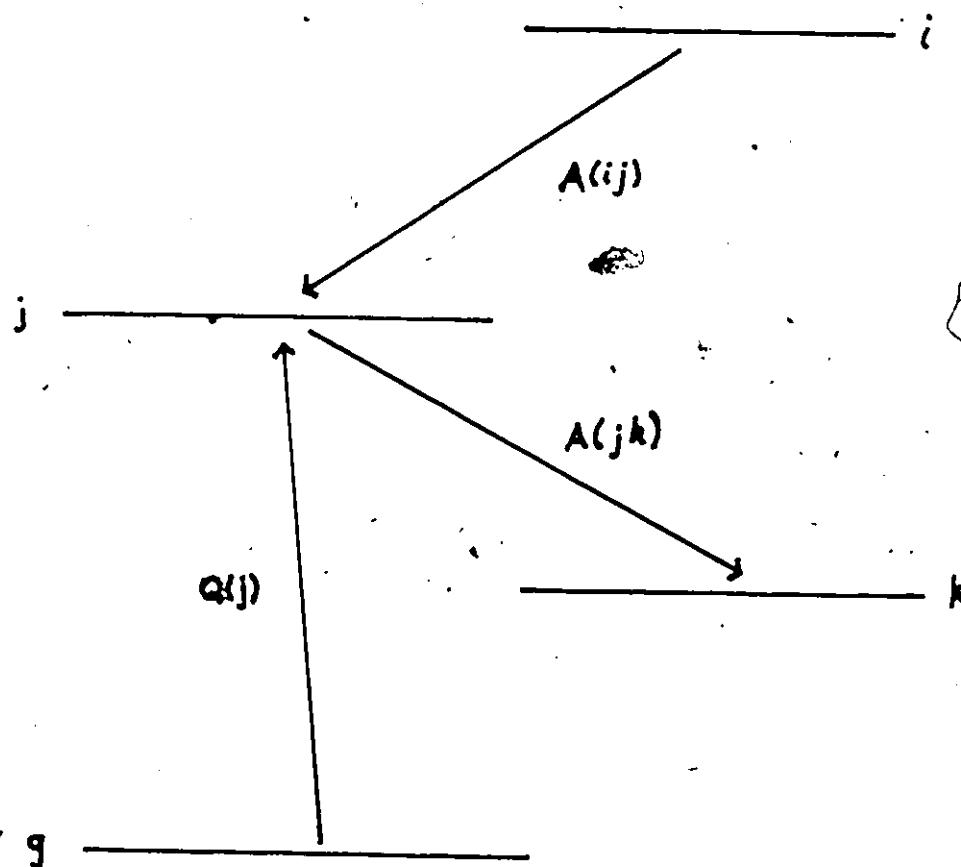
Figure 1: Schematic energy level diagram showing
excitation and deexcitation processes.

2.2.2　Effective Cross Section

Often one measures the intensity of only one spectral line as a function of the electron impact energy (E). In other words $J(jk,E)$ is measured. Normally, these measurements are given in terms of an effective cross section, $Q(jk)$, which is defined as:

$$Q(jk) = J(jk)\ \epsilon/IN \qquad (9a)$$

$$= E(jk)[Q(j) + \sum_{i} Q(ij)] \qquad (9b)$$
$$i>j$$

2.2.2.1　Polarization

The radiation produced can be resolved into 3 components. Defining the electron beam axis as the z-axis, the intensity of the radiation observed perpendicular to the electron beam and with its electric vector parallel to the z-axis is called I_{11}. The two components with their electric vectors perpendicular to the z-axis are rotationally invariant and hence equal. They are denoted by I_1.

The polarization, p, of the radiation is defined by

$$p = (I_{11} - I_1)/(I_{11} + I_1) \qquad (10)$$

The flux of photons emitted into unit solid angle at an angle, θ, to the electron beam, for the j-k transition, is given by

$$J(jk,\theta) = I(jk)_{11}\sin^2\theta + I(jk)_1\cos^2\theta + I(jk)_1 \qquad (11)$$

Thus the total flux is found by integrating over all solid angles

$$J(jk) = \int J(jk,\theta)\, dw \qquad (12a)$$
$$= 8\pi/3\, [\, I(jk)_{11} + 2I(jk)_{1}\,] \qquad (12b)$$

and the effective cross section is given by equation (9). Therefore, by measuring I_{11} and I_{1}, one can also determine the effective cross section.

2.2.3 Differential Cross Section

In many experiments, ours included, the intensity of radiation emitted per unit solid angle at some angle, θ, with respect to the electron beam is measured. In this case, one is making a measurement of a differential cross section $(g(jk,\theta))$. For dipole radiation the angular distribution of the radiation is of the form

$$g(jk,\theta) = a(jk)\,(1 - p\cos^2\theta) \qquad (13a)$$
$$= J(jk,\theta)\, e/IN \qquad (13b)$$

where p is the polarization of the radiation, and p and $a(jk)$ are independent of θ but are functions of the electron impact energy. The effective cross section is therefore the integral of the differential cross section over all solid angles.

$$Q(jk) = \int q(jk)\, dw = 4\pi(1 - p/3)a(jk) \qquad (14)$$

Thus, for measurements at 90°

$$Q(jk) = 4\pi(1 - p/3)q(jk,90°) \tag{15}$$

However, if the angle, θ, is chosen such that $\cos^2\theta$ equals $1/3$ then

$$\text{and} \quad q(jk) = a(jk)(1 - p/3) \tag{16}$$

$$Q(jk) = 4\pi q(jk) \tag{17}$$

This angle is known as the magic angle and equals 54°44'. Thus, if one measures J(jk) at the magic angle, no polarization corrections are needed as at, say 90°, and the differential cross section is proportional to the effective cross section.

2.2.3.1 Polarization

However, this is only true if the detection system is not polarization sensitive. If it is, the detection system must be corrected for differences in its detection sensitivity. Assuming that the radiation passes through a slit, which defines the solid angle, then the detection system has sensitivities $k_\perp$ and $k_{\parallel}$ to radiation polarized with its electric vector respectively perpendicular and parallel to the slit. Consequently, the observed photon flux at the magic angle may no longer be proportional to the effective cross section.

Consider observing the radiation at an angle, θ, to the electron beam and at an orientation, X (see Figure 2), such that the slit is at an angle, 90° - X, to the plane defined

by the electron beam and the optic axis (line connecting the interaction volume to the center of the slit). Then the observed signal is given by (for clarity the state indicators j,k are not shown):

$$S(\theta,X) = I_{11}(k_{11}\sin^2 X \sin^2\theta + k_1\cos^2 X \sin^2\theta) +$$
$$I_1(k_{11}(\cos^2 X + \sin^2 X \cos^2\theta)$$
$$+ k_1(\sin^2 X + \cos^2 X \cos^2\theta)) \qquad (18)$$

However, if one sets $X = 45^o$ and $\theta = 54^o44'$ then

$$S(\theta,45) = 1/3[k_{11} + k_1][I_{11} + 2I_1] \qquad (19a)$$
$$= (k_{11} + k_1)J(jk)/8 \qquad (19b)$$
$$= IN(k_{11} + k_1)Q(jk)/8\ e \qquad (19c)$$

Thus, by suitably orienting the detection system with respect to the electron beam, the observed signal is proportional to the effective cross section.

A second common orientation uses $\theta = 90^o$ and $X = 45^o$. For this case S equals

$$S(90,45) = (k_{11} + k_1)(I_{11} + I_1)/2 \qquad (20a)$$
$$= 1/2\ [k_{11} + k_1]\ J(jk,90) \qquad (20b)$$
$$= [k_{11} + k_1]\ \frac{I\ N\ Q(jk)}{8\ e(1 - p/3)} \qquad (20c)$$

and Q(jk) is proportional to $(1 - p/3)\ S(90,45)$.

A third common orientation uses $\theta = 90^o$ and $X = 0^o$. For this case S equals

a)

b)
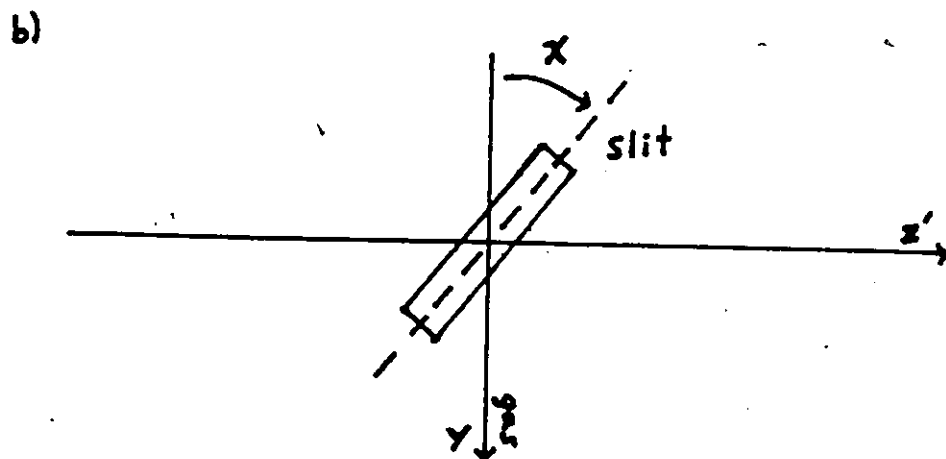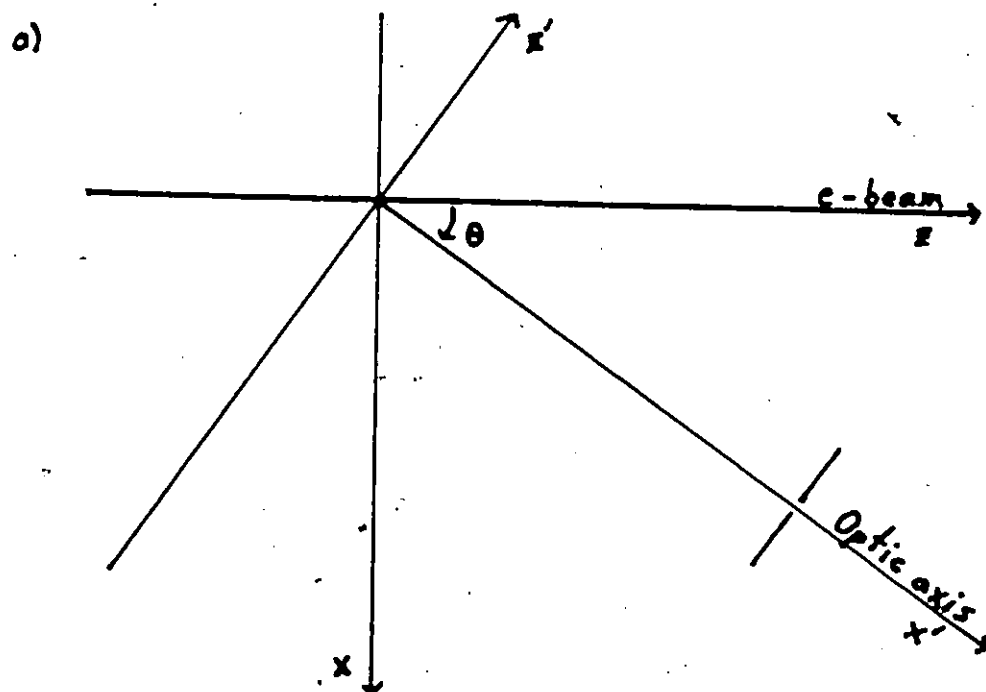
Figure 2: Illustration of the relevant experimental
angles, θ and χ.

$$S(90,0) = k_\perp I_{\perp\perp} + k_{\perp\perp} I_\perp \qquad (21a)$$

$$= k [I_{\perp\perp} + I_\perp] \quad \text{if } k_{\perp\perp} = k_\perp = k \qquad (21b)$$

and $Q(jk)$ is proportional to $(1 - p/3)$ $S(90,0)$. However, this is only true if $k_\perp$ equals $k_{\perp\perp}$. However, if the radiation has zero polarization $(I_{\perp\perp} = I_\perp)$, then

$$S(90,0) = (k_{\perp\perp} + k_\perp) I_\perp \qquad (21c)$$

and $Q(jk)$ is proportional to $S(90,0)$.

2.3 Quantum Mechanical Theory

The following discussion will deal only with the excitation of a target atom or molecule at rest, and in it's ground state, by a beam of monoenergetic electrons. In the center of mass frame, the effective cross section for scattering into the volume, Δ', in the space of the final relative momenta is given by (see [86])

$$\sigma(\Delta'\alpha' \leftarrow \vec{p}\alpha) = \frac{(2\pi)^4 m}{p} \int_{\Delta'} d\underline{p}' \ \delta(E'-E) |t(\underline{p}'\alpha' \leftarrow \vec{p}\alpha)| \qquad (22)$$

where α' and α represent the set of quantum numbers representing the ground (initial) state and final state, respectively. $\vec{p}$ is the relative momenta of the incident electron, m is the reduced mass of the electron and target, $\underline{p}'$ represents the set of final relative momenta after the collision, $d\underline{p}'$ an element of volume in the final relative momentum

space, E the initial energy, E' the final energy, and t the
t-matrix. The t-matrix is given by

$$t(\underline{p}'\alpha' \leftarrow \vec{p}\alpha) = \langle \underline{p}'\alpha' - |V^{\alpha}|\vec{p}\alpha \rangle \qquad (23)$$

where V^{α} is the interaction term of the Hamiltonian for the
incident electron with the target. $|\vec{p}\alpha\rangle$ is the incident
"free" particle state and $|\underline{p}'\alpha-\rangle$ is the stationary scattering
state given by

$$|\underline{p}'\alpha'-\rangle = \Omega_{-}^{\alpha'}|\underline{p}'\alpha'\rangle \qquad (24)$$

where $|\underline{p}\alpha'\rangle$ is the final "free" particle state and $\Omega_{-}^{\alpha'}$ is the
α' channel Møller operator which is defined as

$$\Omega_{-}^{\alpha'} = \lim_{t \to \infty} e^{iHt} e^{-iH^{\alpha'}t} \qquad (25)$$

where $\qquad H = H^{\alpha'} + V^{\alpha'} \qquad (26)$

where H is the Hamiltonian and $V^{\alpha'}$ is that part of the
potential linking the final particles.

As we do not detect any of the scattered particles, we
are interested in the total effective cross section. It is
given by performing the integration of equation (23) over
the entire final relative momentum space. Equation (27)
shows the result.

$$\sigma(\alpha' \leftarrow \vec{p}\alpha) = \frac{(2\pi)^4 m}{p} \int d\underline{p}' \; \delta(E'-E)|t(\underline{p}'\alpha' \leftarrow \vec{p}\alpha)|^2 \qquad (27)$$

It is equal to the effective cross section for excitation, as in the previous section, provided their is no cascade.

2.3.1 Born Approximation

The Born approximation is derived by making the following approximation to the t-matrix. The approximation assumes that the effect of the scattering potential, v^α, is small such that

$$|\underline{p}'\alpha'-\rangle \simeq |\underline{p}'\alpha'\rangle \tag{28}$$

and $$t(\underline{p}'\alpha' \leftarrow \vec{p}\alpha) = \langle \underline{p}'\alpha'|v^\alpha|\vec{p}\alpha\rangle \tag{29}$$

Consequently, the total effective cross section becomes

$$\sigma(\alpha' \leftarrow \vec{p}\alpha) = \frac{(2\pi)^4 m}{p} \int d\underline{p}' \ \delta(E'-E)|\langle \underline{p}'\alpha'|v^\alpha|\vec{p}\alpha\rangle|^2 \tag{30}$$

Equation (30) is the Born approximation. If the two final particles consist of the incident electron and the target atom (molecule) then equation (30) reduces to the common expression.

$$d\sigma(\alpha' \leftarrow \vec{p}\alpha) = (2\pi)^4 \ \frac{m}{p} \ |\langle \vec{p}'\alpha'|v^\alpha|\vec{p}\alpha\rangle|^2 \ d\Omega \tag{31a}$$

$$= \frac{p'}{p} \ |f(\vec{p}'\alpha' \leftarrow \vec{p}\alpha)|^2 \ d\Omega \tag{31b}$$

$d\Omega$ is the solid angle into which the electron is scattered, $\vec{p}'$ is the final relative momenta of the electron, and f is the scattering amplitude.

$$f(\vec{p}'\alpha' \leftarrow \vec{p}\alpha) = (2\pi)^2 \, m \langle \vec{p}'\alpha' | V^\alpha | \vec{p}\alpha \rangle \tag{32}$$

2.3.2 Electron-Atom Collisions

To evaluate the matrix element in equation (31) we represent the initial and final "free" particle wavefunctions by

$$|\vec{p}\alpha\rangle = (2\pi)^{-3/2} \, e^{i\vec{k}\cdot\vec{r}} \, \Psi_\alpha(\vec{r}_1,\ldots,\vec{r}_n) \tag{33a}$$

and

$$|\vec{p}'\alpha'\rangle = (2\pi)^{-3/2} \, e^{i\vec{k}'\cdot\vec{r}} \, \Psi_{\alpha'}(\vec{r}_1,\ldots,\vec{r}_n) \quad . \tag{33b}$$

where $\vec{p}$ and $\vec{p}'$ are the initial and final relative momenta of the incident electron, $\vec{k}$ equals $\vec{p}/\hbar$, $\vec{k}'$ equals $\vec{p}'/\hbar$, Ψ_α is the initial (ground) state of the atom, and $\Psi_{\alpha'}$ is the final state of the atom. $\vec{r}$ is the space coordinate of the electron in the center of mass frame and $\vec{r}_1$ to $\vec{r}_n$ are the coordinates of the n atomic electrons. Substituting equation (33a) and (33b) into the matrix element of equation (31) gives

$$\tag{34}$$

$$\langle \vec{p}'\alpha' | V^\alpha | \vec{p}\alpha \rangle = \int e^{i\vec{k}\cdot\vec{r}} \, \Psi_{\alpha'}^*(\vec{r}_1,\ldots,\vec{r}_n) V^\alpha \Psi_\alpha(\vec{r}_1,\ldots,\vec{r}_n) d\vec{r}_1,\ldots,d\vec{r}_n$$

$\hbar\vec{K} = \hbar(\vec{k} - \vec{k}')$ is the momentum transfer.

For a Coulomb interaction between the incident electron and the "Z" atomic electrons

$$V^\alpha = \sum_{j=1}^{Z} e^2 / |\vec{r} - \vec{r}_j| \quad . \tag{35}$$

and using Bethe's integration formula (1930) [13], the integration over the incident electrons coordinate can be performed.

$$e^2 \int d\vec{r}\ e^{i\vec{K}\cdot\vec{r}} / |\vec{r} - \vec{r}_j| = \frac{4\pi e^2}{K^2}\ e^{i\vec{K}\cdot\vec{r}_j} \tag{36}$$

Upon substituting equation (36) into equation (34) we get

$$\langle \vec{p}'\alpha' | v^\alpha | \vec{p}\alpha \rangle = \frac{4\pi e^2}{K^2}\ \epsilon_{\alpha'\alpha}(\vec{K}) \tag{37}$$

where

$$\epsilon_{\alpha'\alpha}(\vec{K}) = \int \Psi_{\alpha'}^{*}(\vec{r}_1,..,\vec{r}_n) \sum_{j=1}^{Z} \Psi_\alpha(\vec{r}_1,..,\vec{r}_n)d\vec{r}_1,..,d\vec{r}_n \tag{38}$$

$\epsilon_{\alpha'\alpha}(\vec{K})$ is the atomic matrix element. Taking the average over all atomic orientations and summing over all degenerate substates of the state α' results in the atomic matrix element being dependent upon the scalar K. In other words it is independent of orientation. Thus equation (31) can be expressed as

$$d\sigma(\alpha' \leftarrow \vec{p}\alpha) = \frac{4e^4 m^2}{K^4}\ \frac{p'}{p}\ |\epsilon_{\alpha'\alpha}(K)|^2\ d\Omega \tag{39}$$

Using $KdK = kk'\sin\theta\ d\theta$ we can rewrite equation (39) as

$$d\sigma(\alpha' \leftarrow \vec{p}\alpha) = \frac{8\pi e^4 m^2}{K^3 k^2}\ |\epsilon_{\alpha'\alpha}(K)|^2\ dK \tag{40}$$

Using the variable $W = (\hbar K)^2/2m$, with the dimension of energy, changes equation (40) to

$$d\sigma(\alpha' \leftarrow \vec{p}\alpha) = \frac{\pi e^4}{EW} \; |\epsilon_{\alpha'\alpha}(K)|^2 \; d(\ln W) \qquad (41)$$

where E is the energy of the incident electron. Another way of writing equation (41) is in terms of the generalized oscillator strength $f_{\alpha'\alpha}(K)$. It is given by

$$f_{\alpha'\alpha}(K) = \frac{E_{\alpha'\alpha}}{W} \; |\epsilon_{\alpha'\alpha}(K)|^2 = \frac{E_{\alpha'\alpha}}{R(Ka_0)^2} \; |\epsilon_{\alpha'\alpha}(K)|^2 \qquad (42)$$

where a_0 is the Bohr radius, $E_{\alpha'\alpha}$ the excitation energy, and R the Rydberg energy. Thus equation (41) becomes

$$d\sigma(\alpha' \leftarrow \vec{p}\alpha) = \frac{4\pi a_0^2}{E/R \; E_{\alpha'\alpha}/R} \; f_{\alpha'\alpha}(K) \; d(\ln(Ka_0)^2) \qquad (43)$$

and

$$\sigma(\alpha' \leftarrow \vec{p}\alpha) = \frac{4\pi a_0^2}{E/R} \int \frac{f_{\alpha'\alpha}(K)}{E_{\alpha'\alpha}/R} \; \frac{d(Ka_0)^2}{(Ka_0)^2} \qquad (44)$$

where the integral extends over all possible values of $(Ka_0)^2$.

2.3.3   Bethe Approximation

Bethe (1930) [13] showed that if the total effective cross section is expanded in inverse powers of E, that the resulting expression contains coefficients which are completely determined from the generalized oscillator strength. For an optically allowed transition the result is

$$\sigma(\alpha' \leftarrow \vec{p}\alpha) = \frac{4\pi a_0^2}{E/R} \left[M_{\alpha'\alpha}^2 \ln\left(4 c_{\alpha'\alpha} \frac{E}{R}\right) + \frac{g_{\alpha'\alpha}}{E/R} + 0\left(\frac{E_{\alpha'\alpha}^2}{E^2}\right) \right] \tag{45}$$

The leading term is known as Bethe's asymptotic cross section. $M_{\alpha'\alpha}$ is the dipole matrix element between states α' and α, and is related to the optical oscillator strength, $f_{\alpha'\alpha}(=E_{\alpha'\alpha}M_{\alpha'\alpha}/R)$. $c_{\alpha'\alpha}$ is a constant depending on $E_{\alpha'\alpha}$ and is a property of the transition to state α'. $g_{\alpha'\alpha}$ depends upon the reduced mass and may have either sign. For an optically forbidden transition the cross section is given by

$$\sigma(\alpha' \leftarrow \vec{p}\alpha) = \frac{4\pi a_0^2}{E/R} \left[b_{\alpha'\alpha} + \frac{g_{\alpha'\alpha}}{E/R} + 0\left(\frac{E_{\alpha'\alpha}^2}{E^2}\right) \right] \tag{46}$$

where

$$b_{\alpha'\alpha} = \int_{-\infty}^{\infty} \frac{f_{\alpha'\alpha}(K)}{E/R} \, d[\ln(Ka_0)^2] \, . \tag{47}$$

In the high energy limit ($E \longrightarrow \infty$) equations (45) and (46) are reduced to

$$\sigma(\alpha' \leftarrow \vec{p}\alpha) \simeq 4\pi a_0^2 R M_{\alpha'\alpha}^2 \ln E/E \quad \text{(allowed)} \tag{48}$$

$$\simeq 4\pi a_0^2 R b_{\alpha'\alpha} 1/E \quad \text{(forbidden)} \tag{49}$$

In other words for an optically allowed transition the total effective cross section falls off as $(\ln E)/E$; whereas, for an optically forbidden transition it falls off as $1/E$ at sufficiently high impact energies.

2.4 Gas Flow at Low Pressures

2.4.1 Introductory Concepts

The manner in which gas flows through a tube is commonly divided into three regimes.

1) $K = D/\lambda > 10^2$ Viscous flow
2) $1 < D/\lambda < 10^2$ Intermediate flow
3) $D/\lambda < 1$ Molecular flow

K is called the Knudsen number, D is the diameter of the tube, and λ is the mean free path. The rate at which a volume of gas flows through a plane at a pressure P, is given by

$$P = P \, dV/dt \qquad (50)$$

where P is called the throughput and dV is an element of volume. Upon using the ideal gas law equation (50) becomes

$$P = kT \, dN/dt = nkT \, dV/dt$$
$$= nkT \, S = kT \, nvA = PvA \qquad (51)$$

where k is Boltzmann's constant, T the absolute temperature, dN/dt the rate at which molecules cross the plane, n the number density, S (=dV/dt) the pumping speed, v the flow velocity, and A the area of the plane. As long as P and T remain constant at the plane, the number density will be constant and the throughput will be directly proportional to a molecular current (dN/dt = n dV/dt). If the system is in equilibrium (gas flow in equals gas flow out) the molecular

current across every cross section (plane) must be equal. Consequently, the throughput must be the same throughout the system.

The conductance between two points of the system is defined as

$$C_{12} = F/(P_1 - P_2) \qquad (52)$$

where "1" and "2" denote the respective points. Using equation (51) and (52) the pressures (or number densities) at two different points of the system can be related as follows.

$$P_2 = P_1[1 - vA/C_{12}] \qquad (53a)$$

or

$$n_2 = n_1[1 - vA/C_{12}]T_1/T_2 \qquad (53b)$$

$$= n_1[1 - vA/C_{12}] \quad \text{if } T_1 = T_2 \qquad (53c)$$

Note, vA is the pumping speed at point "1".

2.4.2 General Flow

The conductance of a tube can be written as follows:

$$C = C_m J \qquad (54)$$

where C_m is the conductance for molecular flow and J is given by (see [76])

$$J = \frac{C_m}{C_v} \cdot \frac{1 + (M/R_0T)^{\frac{1}{2}} D\bar{P}/\eta}{1 + 1.24(M/R_0T)^{\frac{1}{2}} D\bar{P}/\eta} \qquad (55a)$$

and

$$C_v = \pi D^4 \bar{P}/128 \eta L \qquad (55b)$$

$$C_m = (D^3/6L)[2\pi R_0 T/M]^{\frac{1}{2}} \qquad (55c)$$

$\overline{P}$ is the average pressure between two points, R_0 equals kN_a, N_a is Avogadro's number, D is the diameter of the tube, L is the length of the tube, η is the coefficient of viscosity, and C_v is the conductance for viscous flow. The above equations are in cgs units.

A pressure of interest, $\overline{P}_i$, is called the molecular-viscous intersection pressure. It corresponds to the case where C_v equals C_m. In other words,

$$C_v/C_m = 1 = [6\pi/128\,\eta][M/2\pi R_0 T]^{\frac{1}{2}}\ D\overline{P}_i \qquad (56a)$$

or

$$D\overline{P}_i = 116\,(T/M)^{\frac{1}{2}}\,\eta \quad \text{Torr-cm} \qquad (56b)$$

$$= 3.1 \times 10^{-19}\ T/\xi^2 \quad \text{Torr-cm} \qquad (56c)$$

where ξ is the molecular diameter. Defining a new variable, δ, equation (55b) can be written as

$$J = \delta + (1 + 17\delta)/(1 + 21\delta) \qquad (57)$$

where $\qquad \delta = \overline{P}/\overline{P}_i \qquad (58)$

Equation (57) is valid for any gas at any temperature. However, it is only valid in cases where the flow is the same over the entire length of the tube. For the general case, we can consider intervals dL over which the same flow exists and across which there is a pressure variation dP. Then the throughput is given by

$$F = C_{12}\ (P_1 - P_2) = C\ dP \qquad (59a)$$

$$= L\ C_m\ J\ dP/dL \qquad (59b)$$

where C_{12} is the conductance across the tube and C is the conductance across the interval dL. Integrating equation (59b), and assuming constant throughput, gives

$$P = C_m \bar{P}_i (\delta^2/2 + 17\delta/21 + (4/21\delta)\ln(1 + 21\delta)) \qquad (60)$$

Now consider the number density which exists at some place in the vacuum system. In our case the important place is the interaction region. Using equations (51) and (60) one can derive

$$n_t = \frac{C_m \bar{P}_i}{kT \ v\lambda}[\delta^2/2 + 17\delta/21 + (4/21\delta)\ln(1 + 21\delta)] \quad (61a)$$

$$= H \ f(\bar{P},\bar{P}_i)/kT \qquad (61b)$$

where
and
$$H = C_m /v\lambda \qquad (62)$$

$$f(\bar{P},\bar{P}_i) = \bar{P}_i[\delta^2/2 + 17\delta/21 + (4/21\delta)\ln(1 + 21\delta)] \quad (63)$$

Equation (61) is important as it describes how the number density in the interaction region changes as a function of pressure. It depends on two quantities; the molecular-viscous intersection pressure, and H, the ratio of the conductance for molecular flow to the pumping speed at the interaction region. Since the radiation which we detect, $J(jk)$, is proportional to the target number density, we can determine $\bar{P}_i$ by plotting the detected signal as a function of pressure. From equations (9) and (61) we have

$$J(jk,P) = \frac{IQ(jk)}{e} n_t = \frac{IQ(jk) H}{e \ kT} f(\bar{P},\bar{P}_i) \qquad (64)$$

Thus, if the first set of variables are constant, the detected signal will follow the form of $f(\bar{P}, \bar{P}_i)$, and a determination of the molecular-viscous intersection pressure can be made.

2.4.3 Molecular Flow

When molecular flow conditions prevail the conductance of a system is independent of pressure. The general expression is

$$C_m = G \ (2kT/m)^{\frac{1}{2}} \tag{65}$$

where G is a factor which is solely dependent upon the geometry of the system. In other words, it is gas independent. Assuming our gas beam is thermal, we can equate the flow velocity to the arithmetic average given by the Maxwell-Boltzmann velocity distribution. Then the ratio, H, becomes

$$H = C_m / \bar{v}A = G \ (2kT/m)^{\frac{1}{2}}/1.128A(2kT/m)^{\frac{1}{2}} \tag{66a}$$
$$= G/1.128A \tag{66b}$$

Thus, H is solely dependent upon the geometry of the system and using this result in equations (61) and (64) we arrive at the following important result.

$$n_t = \frac{G}{1.128 \ kTA} \ f(\bar{P}, \bar{P}_i) \tag{67}$$

and

$$J(jk) = \frac{IQ(jk)G}{1.128 \ ekTA} \ f(\bar{P}, \bar{P}_i) \tag{68}$$

Since the term in front is constant the detected signal (and the number density) follow the functional form, $f(\overline{P}, \overline{P}_i)$. By determining $f(\overline{P}, \overline{P}_i)$ one can determine the molecular-viscous intersection pressure. Further details concerning the procedure are given in Appendix A. It is important to note that the dependence of n and $J(jk)$ on $\overline{P}$, $\overline{P}_i$, and T have not been explicitly shown in the above equations.

A final observation regarding molecular flow should be made. Since molecular flow corresponds to the condition ($\overline{P} \ll \overline{P}_i$) the function $f(\overline{P}, \overline{P}_i)$ reduces to

$$f(\overline{P}, \overline{P}_i) = \overline{P} \qquad \text{for} \qquad \overline{P} \ll \overline{P}_i \qquad (69)$$

Thus, for small pressures (molecular flow), both n and $J(jk)$ are directly proportional to the pressure.

Chapter III

EXPERIMENTAL SETUP

A schematic of the general setup is shown in Figure 3.
The dashed blocks indicate items which were either not
always available or were not always used. More specific
layouts will be given in the relevant chapters if necessary.
This chapter will only consider the basic components.
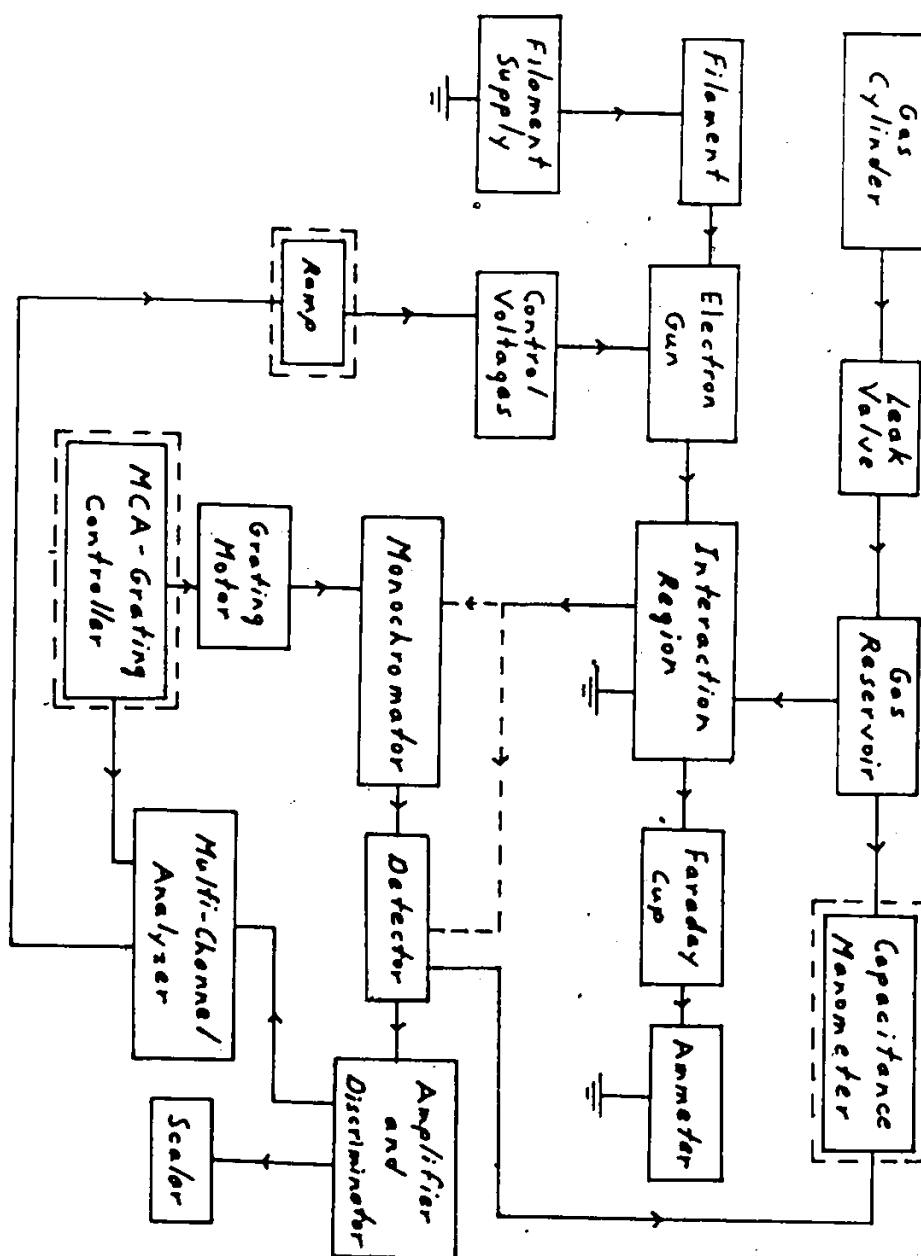
Figure 3: Block diagram of experimental setup.

3.1 Vacuum System

The system is pumped down by three oil diffusion pumps whose forelines are pumped by a common rotary pump. Two of the diffusion pumps employ water cooled baffles and cold traps. Freon 11 is used as their refrigerant. These systems are used on the main chamber (interaction region) and the monochromator. They are required in order to pump the higher gas loads in the main chamber and to attain lower base pressures (6 x 10^{-7} torr), and in the case of the monochromator, to prevent any oil contamination of the diffraction grating. The third diffusion pump is cooled by a water cooled baffle and is used to evacuate the chamber housing the detector connected to the exit port of the monochromator. Consequently, it only attains base pressures near 1 x 10^{-5} torr.

3.2 Interaction Region

The main chamber (interaction region) was common to all our experiments although different configurations were employed. The different configurations will be discussed in the relevant chapters. It is constructed of non-magnetic stainless steel and has nine ports. The axis of eight of the ports have a common intersection point (center of the interaction region). Six of the ports are mutually orthogonal while two other ports are oriented such that the monochromator can be employed at the magic angle and such that the

signal is corrected for any instrumental polarization. The remaining port is often used for an ionization gauge or as an auxiliary pumping port.

3.3 Gas Beams

Gas beams were produced from high purity gas supplies (≥ 99.95%) and entered the interaction chamber through either a multi-capillary array or a single capillary. In most cases the gas source was operated near the molecular flow regime, and when necessary, at low enough driving pressures such that radiation trapping was not too significant. These conditions could be determined by plotting the observed signal for a spectral line versus the source (back) pressure, which could be accurately determined by a capacitance manometer (see Figure 21 to Figure 28).

For the hydrogen experiment a paladium leak was used in order to assure even greater purity of the gas.

3.4 Electrons Source and Collector

Electrons are produced by using the cathode voltage supply to heat a thoriated tungsten filament. Normal operating conditions are approximately 6 volts at 2 amperes. A series of lenses and apertures (see Figure 4) accelerate the electrons to the desired energy and focus them into the interaction region. After traversing the interaction region they are collected by a faraday cup from which they pass to

ground through a picoammeter.   Electron currents between 20
and 125 microamperes with energies between 20 and 1000 eV
(FWHM = 0.8 eV) were used under single collision conditions.
Figure 8 shows an example of photon counts versus electron
. current.
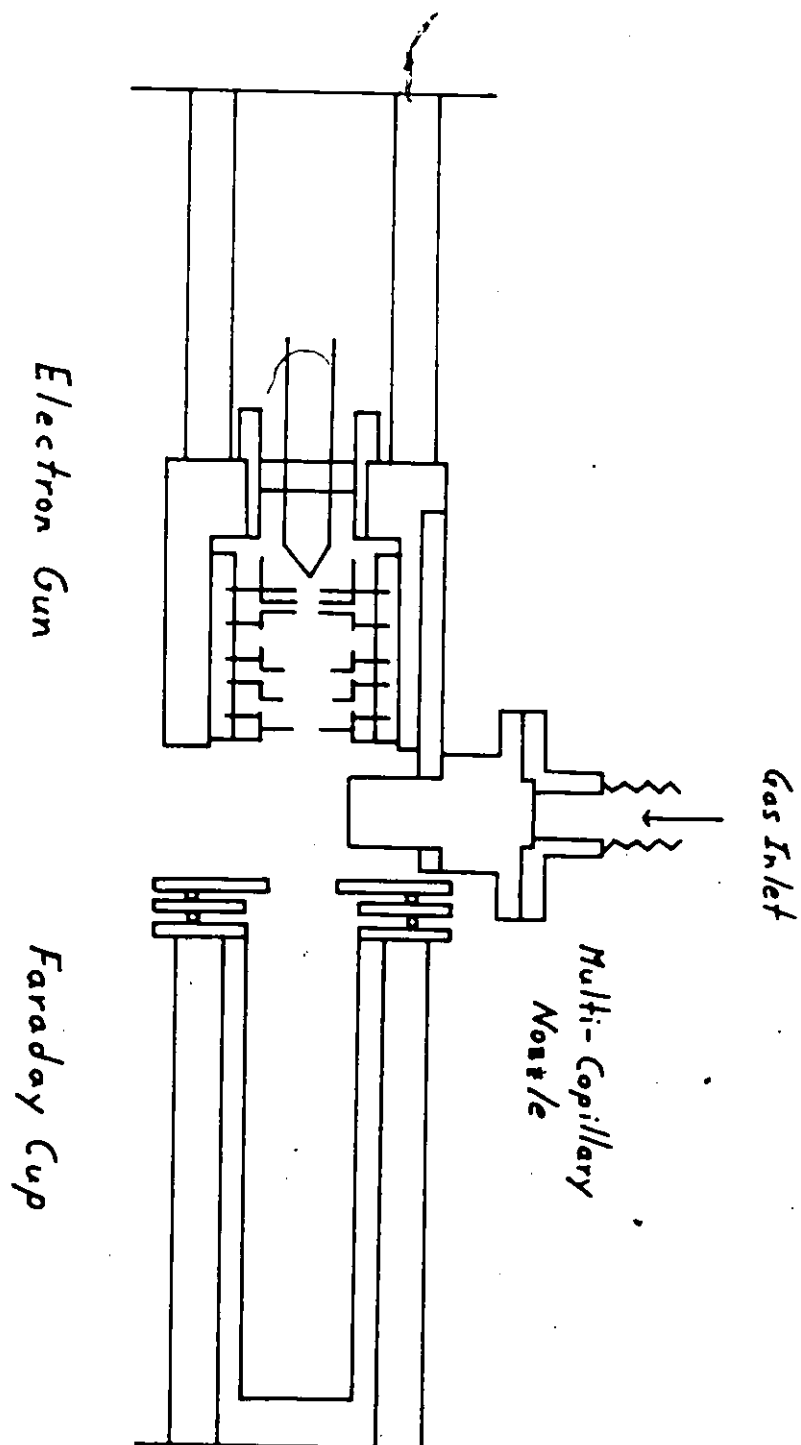
Figure 4: Schematic of the electron gun and faraday cup. A multi-capillary array source can be attached to the housing of the electron gun.

3.5 Monochromator

It is a half-meter Seya-Namioka mounted V.U.V. spectrometer. Two different concave gratings were used. One was gold-coated and blazed at 70 nm, and the other, blazed at 150 nm, had an aluminum and MgF_2 coating. Both gratings have 1200 grooves/mm and linear reciprocal dispersions of 1.7 nm/mm. Entrance and exit slit widths between 0.1 mm and 1 mm were commonly used.

3.6 Photon Detectors

Two detectors were used. Generally, when using the grating blazed at 150 nm a caesium iodide coated Galileo Electro Optics BX 7600-4413 or 4039C channel electron multiplier was employed, whereas for the grating blazed at 70 nm a Mullard 419 BL channel electron multiplier was used. The "70 nm" system was generally used for wavelengths less than 130 nm and the "150 nm" system for wavelengths greater than 110 nm. Of course other combinations are possible and were occasionally used.

3.7 Counting System

The pulses from the detectors were processed by a standard pulse counting system (i.e. amplifier, discriminator) and displayed on either a single channel analyzer (SCA) or displayed and stored on either a TN 1710 or a TN 1705 multichannel analyzer (MCA). Either MCA could be connected to an

IBM 9C01 computer, to which the data was sent for further analysis and storage.

3.8   Auxiliary Controls

Excitation functions and wavelength scans are the two general types of experiments performed with our apparatus. For excitation functions, the monochromator is set such that only the desired spectral line is detected while the electron energy is varied, whereas; for a wavelength scan, the electron energy is fixed while the grating is rotated. In order to facilitate many of our threshold measurements a ramp was used to vary the electron energy. It was connected to the MCA such that each channel on the MCA corresponded to' a different unique electron energy. For our wavelength scans we used two different systems. For our earlier measurements the grating was driven by a continuous DC motor which was not connected to the MCA. Hence, in order to obtain a wavelength scan, the MCA was manually started at the wavelength at which the scan was to begin. After a given period of time (determined by the MCA) the scan would be finished and the motor manually stopped. To obtain more scans the motor would be rewound to the starting wavelength and the procedure performed again. More recently an MCA-Grating Controller was built. It controls both the dwell time of the MCA and the stepping speed of a Superior Electric stepping motor. Also the starting wavelength and num-

ber of scans to be performed are programmable.   Thus it can

collect a wavelength scan without continucus supervision.

Chapter IV

HELIUM EXCITATION

The purpose of this experiment was to determine the absolute cross section for the simultaneous ionization-excitation of the helium ion line at 30.4 nm following electron impact. The cross section was determined for electron impact energies from threshold to 1000 electron-volts. Figure 5 shows the energy level diagram, the relevant excitation process and all relevant emissions.
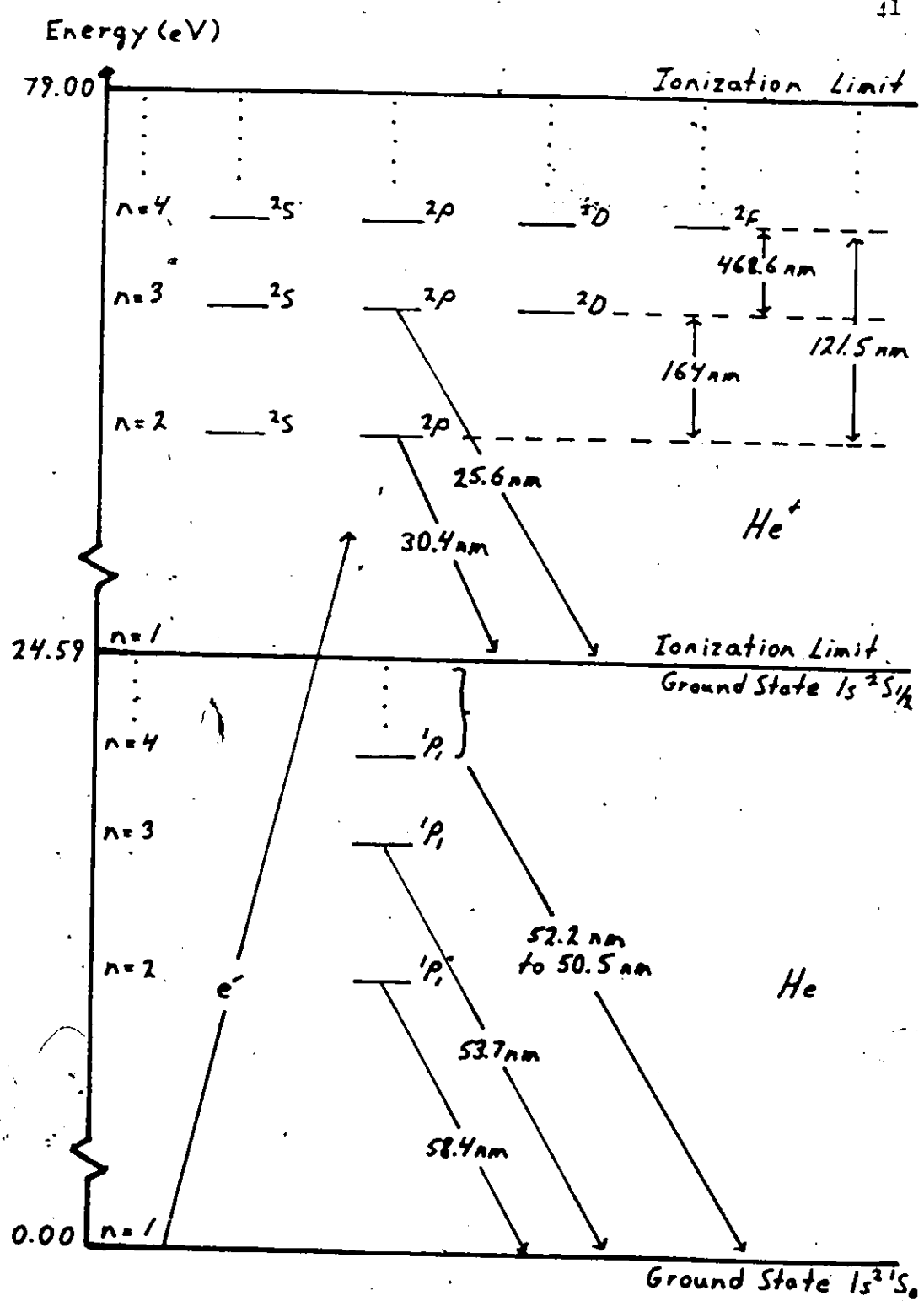
Figure 5: Helium energy level diagram.

4.1 Procedure

The experimental method which we used has the advantage of being relatively straightforward. The unresolved He and He⁺ radiation produced following electron impact on helium was detected by a channel electron multiplier (CEM) mutually perpendicular to both the electron beam and the gas beam after passing through an extreme ultraviolet (XUV) filter. Since the filter transmittance is negligible above 60 nm, the cross section for the helium ion line at 30.4 nm can be extracted utilizing the well known emission cross sections for the helium resonance lines ($n^1P_1 \longrightarrow 1^1S_0$, 58.4-50.5 nm), the transmission properties of the XUV filter, and the wavelength dependent response of the CEM. This procedure was restricted to electron impact energies less than 250 eV due to field penetration effects into the interaction region. These effects were a result of the bias voltage (-250 V) which had to be applied to the cone of the channel electron multiplier in order to prevent the detection of stray electrons. For electron impact energies above 250 eV a monochromator was used to disperse the 30.4 nm radiation. The results from the two different procedures were normalized to each other at 200 eV. However, the final results were not corrected for either cascade or the possible polarization of the observed radiation.

4.2 Theoretical Considerations

From Chapter 2 we know that the rate at which photons, corresponding to decay from a state j to a lower state k, are emitted perpendicular to an electron beam of energy, E, is given by

$$S(jk;90;E) = s(jk;E) = J(jk;90;E)L = j(jk;E)L \qquad (1)$$

where L is the length of the interaction region and J is the photon rate per unit length. However, the actual measured photon rate also depends on the efficiency of the detectors.

For this experiment two different cases must be considered. The first concerns the use of a channel electron multiplier and an XUV filter as our detection system. This is required for the low energy region (E≤250 eV). The second concerns the high energy region (E≥200 eV) where a monochromator and a CEM are employed as our detection system.

For the remainder of the discussion, the functional dependences on E and 90° will be suppressed for convenience unless it is felt to be necessary. Likewise, the functional dependence on gas pressure will also be suppressed.

4.2.1 Case 1 (E ≤ 250 eV)

When the XUV filter and CEM are used only a fraction of the emitted photons are detected. The actual photon rate (B¹; 1 indicates case 1) is given by

$$B^1(jk;E) = S(jk;E)T(jk)C(jk) \qquad (2)$$

where $T(jk)$ is the transmission of the XUV filter and $C(jk)$ is the quantum efficiency of the CEM for light of frequency $v(jk)$ [= $(E(j) - E(k))/h$].

Using equations (13b) and (15) of Chapter 2, equation (2) can be rewritten in the following ways.

$$R'(jk) = j(jk) T(jk) C(jk) L \tag{3}$$

$$= q(jk) T(jk) C(jk) LIN/e \tag{3b}$$

$$= q'(jk) LIN/e \tag{3c}$$

$$= \frac{Q(jk) T(jk) C(jk) LIN}{4\pi e (1 - p(jk;E)/3)} \tag{3d}$$

where $p(jk;E)$ is the polarization of the emitted radiation, I is the electron current, N is the target density, $q(jk)$ is the differential cross section and $C(jk)$ is the effective cross section. q' is important due to its use in future calculations. Note that is has the dimensions of a cross section. If there is any trapping of the helium resonance radiation, the effective cross section must be properly corrected. The trapping factor, $D(j1;P)$, depends on the resonance radiation and the partial pressure of the target gas in the chamber. It's form is derived in Appendix B.

Thus, the total actual photon rate due to the He resonance lines $(n^1P \rightarrow 1^1S)$, and the total actual photon rate due to the He+ lines $(n^2P \rightarrow 1^2S)$ are given by

$$R^1(He) = \sum_{j=2}^{\infty} D(j1) \; R^1(j1;He) \tag{4}$$

$$R^1(He^+) = \sum_{j=2}^{\infty} R^1(j1;He^+) \tag{5}$$

However, we only measure the sum of equations (4) and (5); namely,

$$R_T^1 = R^1(He) + R^1(He^+) \tag{6}$$

Thus, if one determines $R^1(He)$ using the known He resonance cross sections, the transmission properties of the XUV filter, the quantum efficiencies of the channel electron multiplier, and the trapping factors, $D(j1)$, the total actual photon rate for He^+ can be determined.

$$R^1(He^+) = R_T^1 - R^1(He) \tag{7}$$

Using equation (3c), equation (7) can be rewritten in the following final form.

$$\sum_{j=2}^{\infty} q'(j1;He^+) = eR_T^1 / LIN - \sum_{m=2}^{\infty} D(m1) q'(m1;He) \tag{8}$$

4.2.1.1 Normalization

Since L and N are not experimentally determined, $eR_T^1(E)/LIN$ can not be measured absolutely. However, it can be determined through a normalization procedure. Using the fact that for electron impact energies below 65.4 eV (minimum threshold for He^+ excitation) no He^+ radiation is emitted, then

$$eB_T^1(E)/LIN = A \ B_T^1(E) \tag{9a}$$

$$= \sum_{m=2}^{\infty} D(m1) q'(m1;E;He) \quad ; \quad E \leq 65.4 \ eV \tag{9b}$$

where

$$A = e/LIN = \sum_{m=2}^{\infty} D(m1) q'(m1;E;He)/B_T^1(E) \tag{9c}$$

Thus

$$\sum_{j=2}^{\infty} q'(j1;E;He^+) = A \ B_T^1(E) - \sum_{m=2}^{\infty} D(m1) q'(m1;E;He) \tag{10}$$

for all E.

4.2.1.2 Assumptions

In order to determine the effective cross section for the He+ 30.4 nm line, several assumptions are made. They can be expressed as follows:

and
I. $\quad q(j1He^+) = F(E) q(21;He^+)$

II. $\quad T(j1) C(j1) = T \ C$

The first equality states that the contribution to the total He+ signal due to transitions from $j \geq 3$ to j=1 is only a fraction (F) of that due to the transition from j=2 to j=1. Note that F is a function of the impact energy. The second equality states that for $j \geq 3$, T(j1) and C(j1) are given by their median values T and C. Incorporating these assumptions into equation (10) gives

$$q(21;He^+) = \frac{A \ B_T^1 - \sum_{m=2}^{\infty} D(m1) q'(m1;He)}{T(21) C(21) + F(E) TC} \tag{11}$$

for the differential cross section and

$$Q(21;He+) = 4\pi[1 - F(21)/3]q(21;He+) \tag{12}$$

for the effective cross section.   If one also assumes that p=0 for all E, then the apparent cross section, which is the quantity we shall determine, is given by

$$Q(21;He+) = 4\pi q(21;He+) \tag{13}$$

4.2.2   Case 2 (E ≥ 200 eV)

When the monochromator is used the actual photon rate is given by R^2 (2 indicates case 2) where

$$R^2(21;He+) = q(21;He+)Eff(21)LIN/e \tag{14}$$

and Eff(21) is the detection efficiency of the monochromator and channel electron multiplier detection system. Consequently:

$$q(21;He+) = R^2(21;He+)e/Eff(21)LIN \tag{15}$$

4.2.2.1   Normalization

As before q(21;He+) can not be determined absolutely since N and L are not determined. However the normalization factor, B, can be determined by normalizing equation (15) at some energy E_0 which is common to both case 1 and case 2. In other words

$$q(21;E_0;He^+) = \cfrac{A \cfrac{R^1}{T} - \sum\limits_{m=2}^{\infty} C(m1)\, q'(m1;E_0;He)}{T(21)C(21) + F(E)TC} \tag{16a}$$

$$\text{and} \qquad = E(E)R^2(21;E_0;He^+) \tag{16b}$$

$$E(E) = q(21;E_0;He^+)/R^2(21;E_0;He^+) \tag{17}$$

Thus the results from case 2 can be normalized to the results from case 1.

4.3 Experimental

4.3.1 Setup

A schematic diagram of the experimental arrangement is shown in Figure 6. A crossed (90°) electron-beam-gas-beam is oriented such that the photon signal dispersed by the monochromator and detected by a Galileo-Electro-Optics 4039C CEM is corrected for any instrumental polarization. However, for both experimental procedures, the detector was oriented at 90° to the electron beam instead of at the magic angle. Thus, the polarization of the radiation should eventually be taken into account. The filter was a Luxel TF 101 extreme ultraviolet filter. It consists of a 150.0 nm film of an aluminum-silicon alloy with a 27.0 nm carbon overcoat. The gas beam was produced from a multi-capillary array so as to increase the number density and to improve the uniformity of the gas beam.
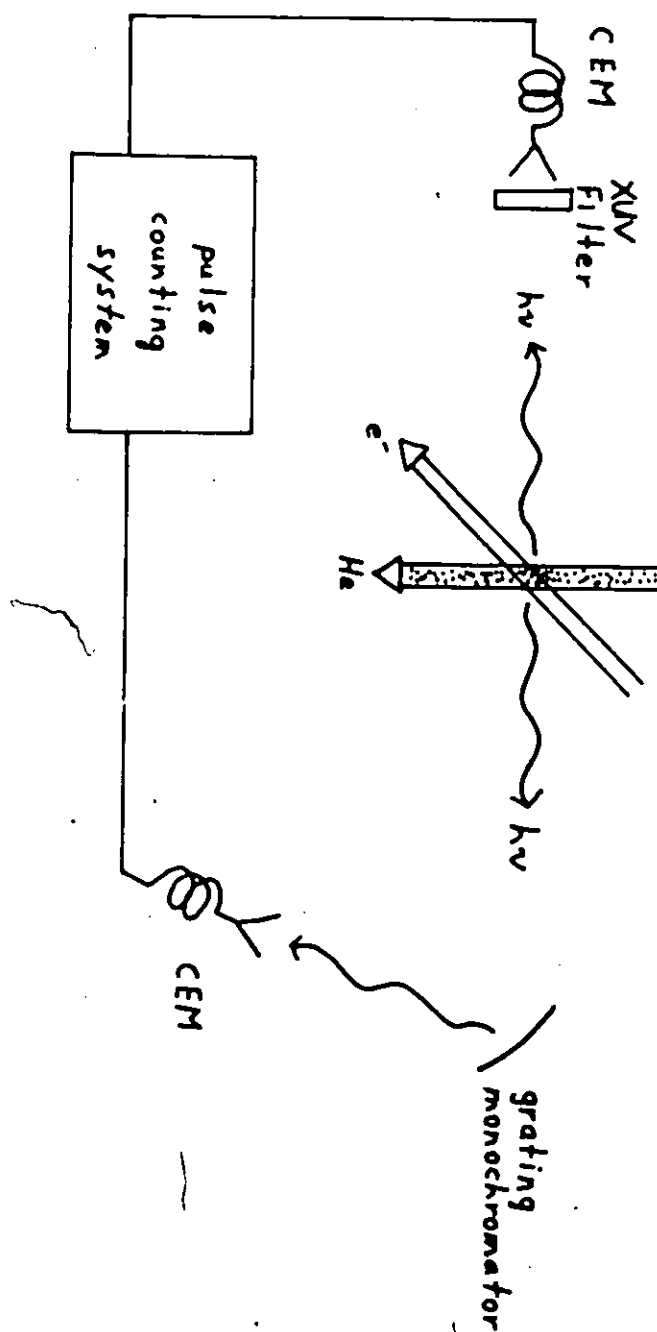
Figure 6: Schematic illustrating the helium experiment.

Regardless of the experimental setup, the electronic pro-
cessing of the signals were identical. For the near-
threshold work, the results were accumulated on the MCA and
a ramp produced by the MCA was used to vary the electron
impact energy. For the work at higher energies a scaler was
used to record the events for each energy.

As mentioned in Chapter 2, in order to be able to ignore
the effects of resonance absorption ([38]) and multiple
scattering in He, one works at sufficiently low gas pres-
sures and electron currents (see Figure 7 and Figure 8).
From Figure 8 it can be seen that for a chamber pressure
(measured with an ionization gauge) of 5.5 microtorr, the
observed signal is quite linear from 10 to 110 microamperes.
Thus, multiple scattering effects could be safely ignored.
Figure 7 shows how the observed He and He$^+$ signal changed
as a function of the partial pressure of the target gas for
an electron current of 25 microamperes and an electron
impact energy of 150 eV. The background pressure was meas-
ured to be 0.6 microtorr. The curved line is a least squares
squares fit of the data to the following formula derived
using the results of Chapter 2 and Appendix B.

$$S(He;P) = S_0 \, P \, \exp[-\alpha \, P] + S(.6) \tag{19a}$$

$$= S_0 \, D(P) + S(.6) \tag{19b}$$

where $S(He;P)$ is the observed signal at the helium partial
pressure P, $S_0 (= 1850 \pm 90)$ is a scaling constant and

$S(.6) (= 172)$ is the signal detected at the background pressure (no He admitted). α $(= .0169 \pm .007)$ is the absorption coefficient and $D(P)$ the total trapping factor. The straight line is derived by letting α go to zero and is the curve which would be followed if there was no resonance trapping. One can use these curves to determine the trapping factors, $D(j1;P)$. These calculations are performed in the next section with the help of several results from Appendix B.
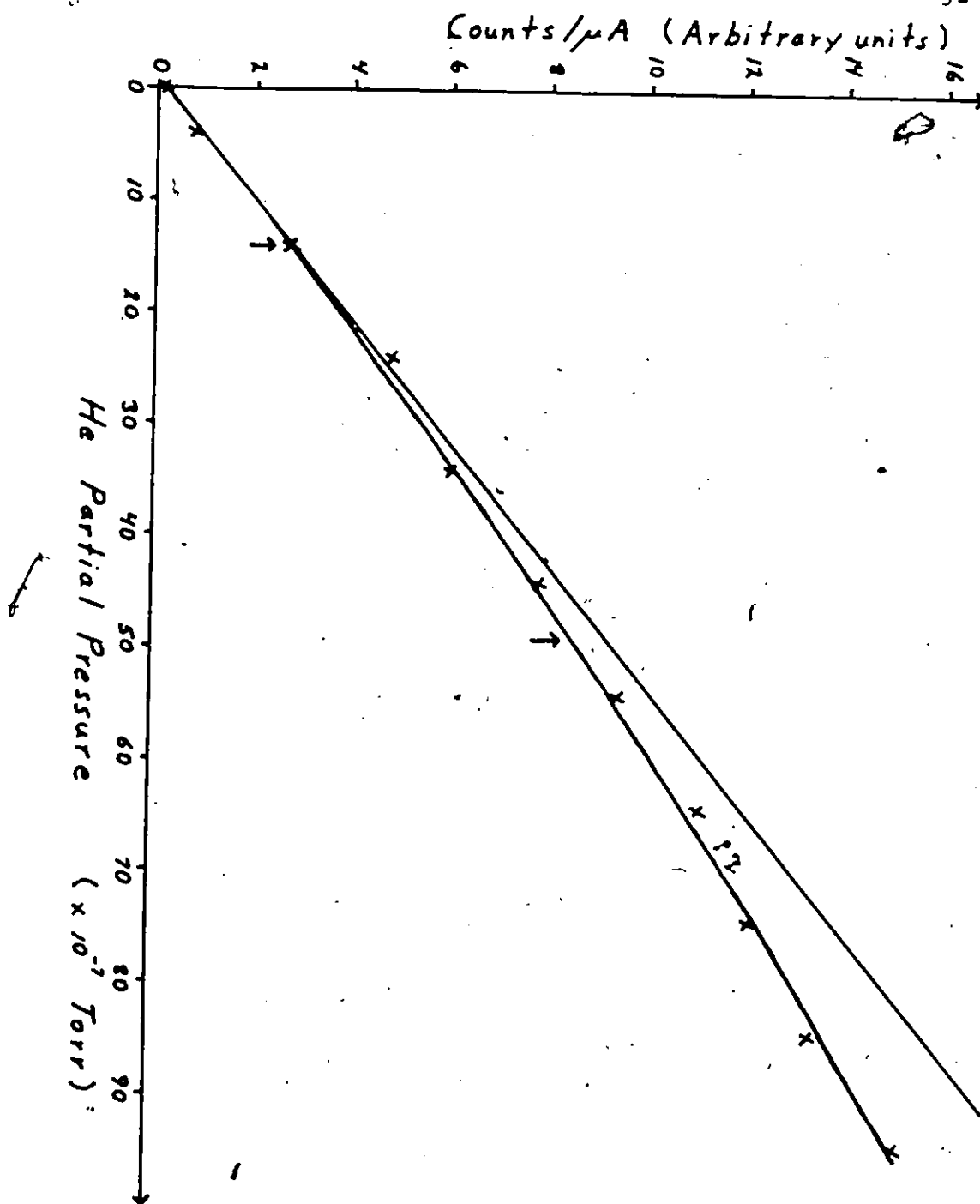
Figure 7: e⁻ +.He signal versus He partial pressure. Arrows indicate positions of the two He partial pressures used in the experiment.
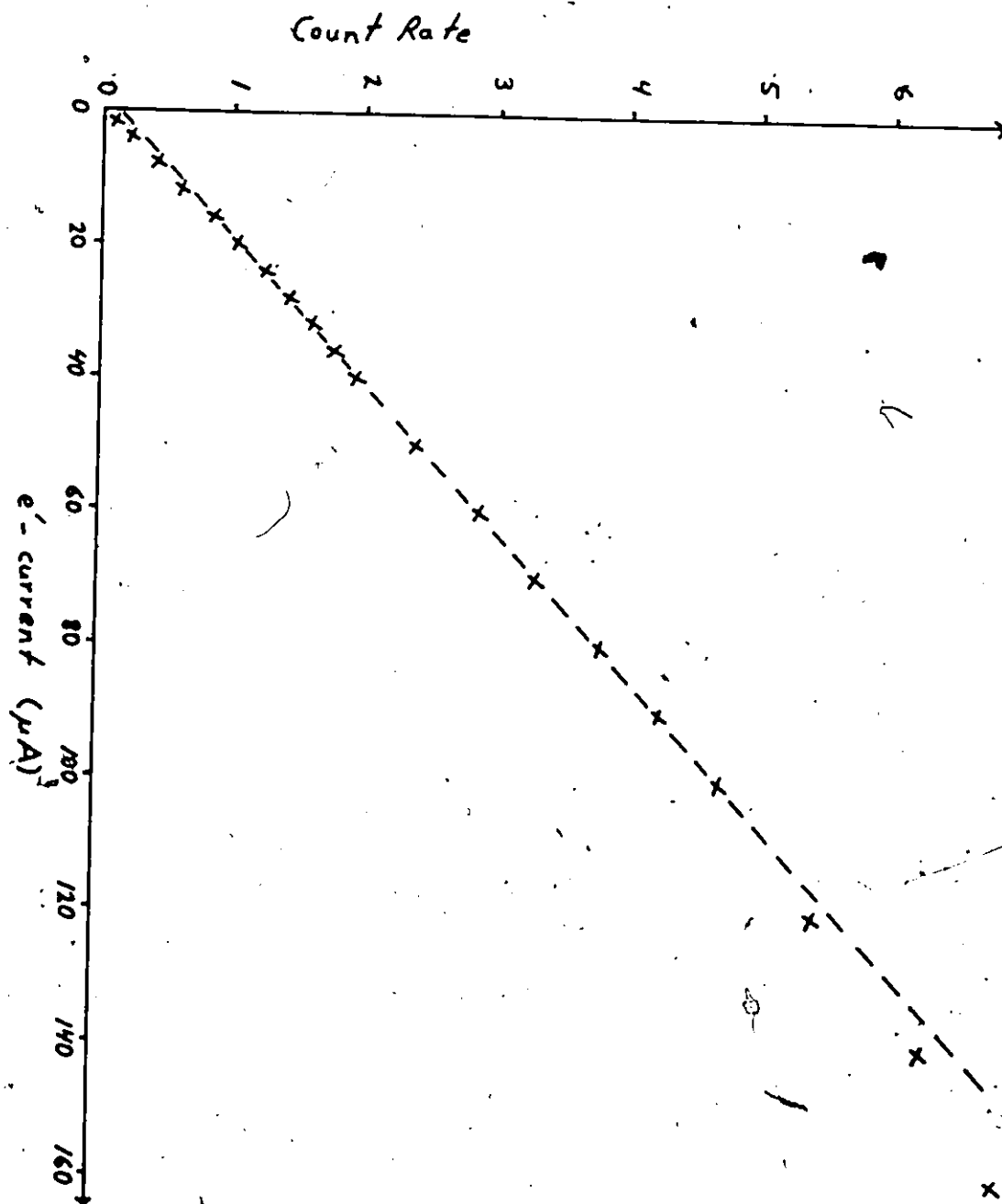
Figure 8: e⁻ + He signal versus electron current.

4.3.2   Calibration

4.3.2.1   XUV Filter

The transmission of the Luxel TF 101 XUV filter versus wavelength is an important parameter in this experiment. Consequently, we have not relied entirely upon the manufacturer's data.   Figure 9 shows both the transmission curve provided by the manufacturer and our experimental data points (tabulated in Table 1). They are in excellent agreement. Our experimental values were determined by dispersing the radiation through the monochromator and counting the observed signal for a given wavelength with and without the filter in place.

4.3.2.2   Channel Electron Multiplier

The quantum efficiency of the Galileo-Electro-Cptics 4039C channel electron multiplier as a function of wavelength is extremely critical.   The values listed in Table 1 are taken from a graph given by Weller and Young (1970) [98] for a 4039C channel electron multiplier. The graph is shown in Figure 10.   The use of their values can be justified as follows.   First, they have studied the same type of CEM as was used in this work.   Secondly, CEM quantum efficiencies have been found to remain constant, within measurement error, as long as the CEM could be operated on the plateau in the characteristic mode (i.e.   count rate constant as a function of the applied high voltage)[98].

4.3.2.3 Trapping factors

Figure 8 does not directly give us the amount by which the helium resonance radiation is being trapped for two reasons. First, the observed signal at 150 eV electron impact energy is composed of radiation from both He and He+. Second, the He radiation results from different transitions which are not equally trapped. However, using equation (18) and results from Appendix B, equation (19) can be expressed in term of the trapping factors, $D(j1;P)$ and in terms of $q'(j1;He)$ and $q'(j1;He+)$. Thus,

$$D(P) = \frac{\sum_{j=2}^{\infty} D(j1;P)\,q'(j1;He) + q'(j1;He+)}{\sum_{j=2}^{\infty} q'(j1;He) + q'(j1;He+)} \tag{19}$$

Using the following result from Appendix B, equation (19) can be expressed in terms of $D(21;P)$.

$$D(j1;P) = D(21;P)^{Y_j} \qquad \text{for } j>3 \tag{20}$$

where
$$Y_3 = 0.2719 \qquad Y_4 = 0.1131$$
and
$$Y_5 = 0.0575$$

Y_j are the respective trapping coefficients. Therefore, $D(P)$ can be expressed as

$$D(P) = \frac{\sum_{j=2}^{\infty} D(21;P)^{Y_j}\,q'(j1;He) + \sum_{j=2}^{\infty} q'(j1;He+)}{\sum_{j=2}^{\infty} q'(j1;He) + q'(j1;He+)} \tag{21}$$

Making the following assumption (justification is given from Figure 11 and Figure 12).

$$\sum_{j=2}^{\infty} q'(j1;He+) / \sum_{j=2}^{\infty} q'(j1;He) = 0.50 \pm .02 \qquad (22)$$

then $D(P)$ can be written as

$$D(P) = \frac{\sum_{j=2}^{\infty} D(21;P)^{j} q'(j1;He) + 0.5 \sum_{j=2}^{\infty} q'(j1;He)}{(1 + 0.5) \sum_{j=2}^{\infty} q'(j1;He)} \qquad (23)$$

where $D(P)$ is known from equation (19) and $\sum q'(j1;He)$ can be calculated. While equation (23) can not be solved analytically, it can be solved by trial substitution. The two target partial pressures which we used were 1.4 microtorr and 4.9 microtorr. Their respective values for $D(P)$ are 0.977 ± .01 and 0.921 ± .03. The results for $D(n1;P)$ (n equals 1 to 5) are listed in Table 1.
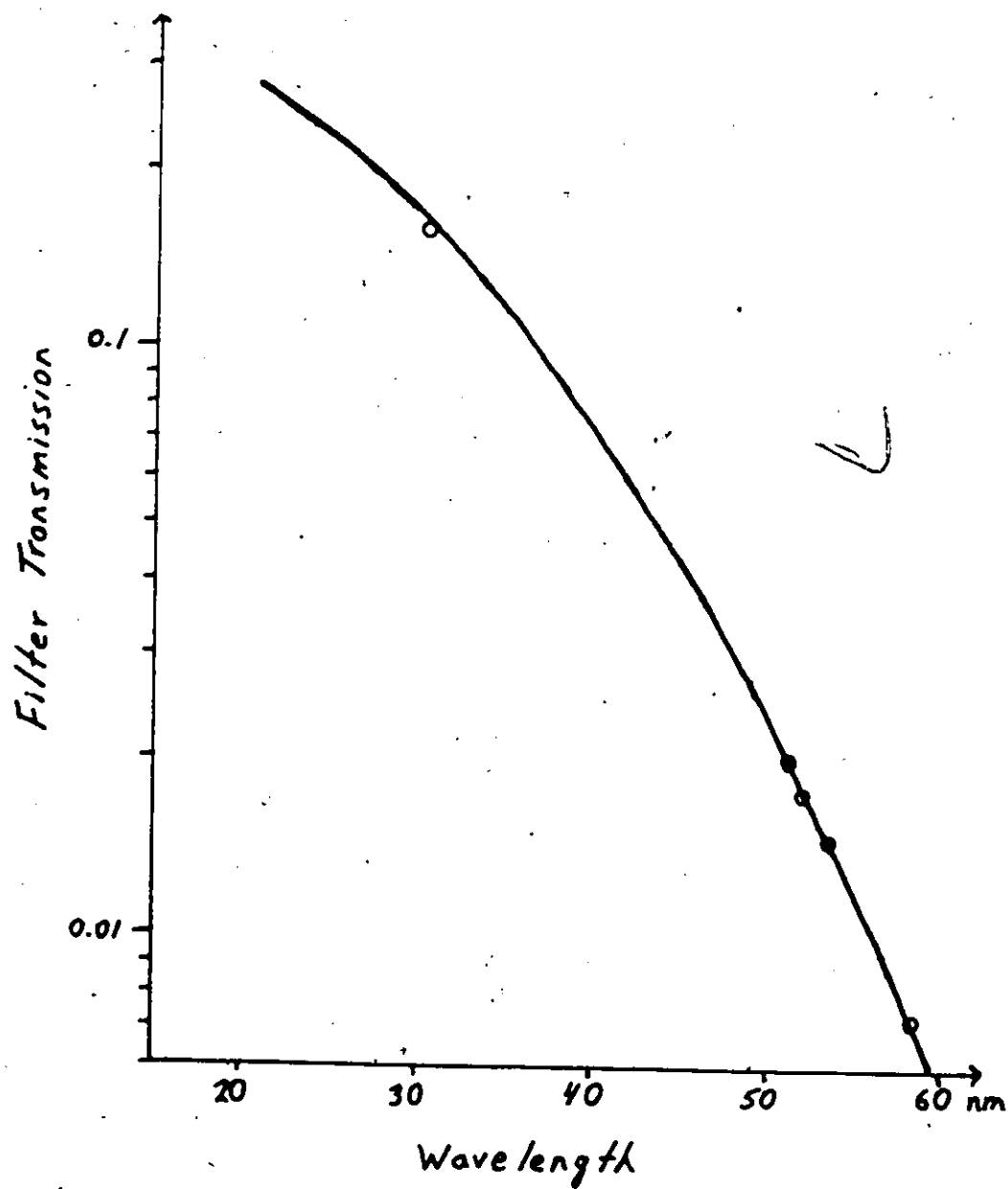
Figure 9: Luxel TF 101 XUV filter transmission versus wavelength.
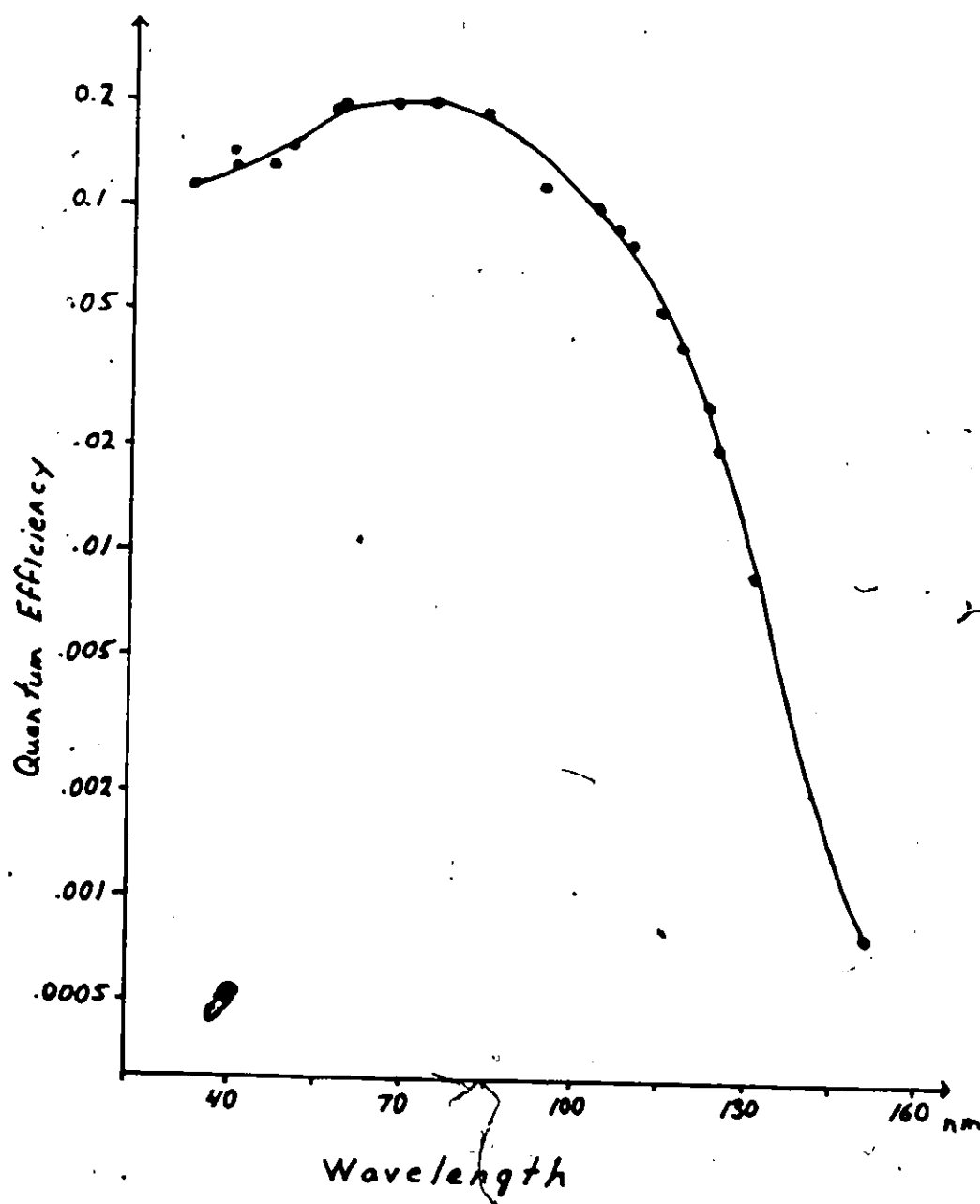
Figure 10: Channel electron multiplier quantum efficiency
versus wavelength. Taken from Weller and
Young [98].

TABLE 1

Transition	Wavelength (nm)	Filter Transmission $T(\lambda)$	Quantum Efficiency [b] $C(\lambda)$	$T(\lambda)C(\lambda)$	Trapping Factor $D(nl,P)$ $P = 1.4$ μTorr	Trapping Factor $D(nl,P)$ $P = 4.9$ μTorr
He 2^1P-1^1S	58.4	0.0072 ± 1.9%	0.187 ± 10%	0.00135 ± 11%	0.944 ± 4.3%	0.803 ± 11%
He 3^1P-1^1S	53.7	0.0147 ± 2.6%	0.165 ± 10%	0.00243 ± 11%	0.986 ± 2.3%	0.947 ± 5.9%
He 4^1P-1^1S	52.2	0.0175[b] ± 2.4%	0.159 ± 10%	0.00278 ± 11%	0.994 ± 1.5%	0.978 ± 3.8%
He $n{\ge}5^1P$-1^1S	50.5-51.7	0.0200 ± 3.6%	0.155 ± 10%	0.00310 ± 11%	0.997	0.989 ± 2.7%
He$^+$ 2^2P-1^2S	30.4	0.157 ± 2.1%	0.115 ± 10%	0.0181 ± 11%	1	1
He$^+$ $n{\ge}3^2P$-1^2S	22.8-25.6	0.23[a] ± -5.0%	0.109 ± 15%	0.025[c] ± 16%	1	1

(a) From manufacturer's data
(b) From Weller and Young [98]
(c) Extrapolation of Weller and Young's data

4.4 Results

4.4.1 The Low-Energy Region

The low-energy region encompasses the range of electron impact energies from threshold to 250 eV. The measured excitation function for the combined He and He+ emissions below 60 nm is shown in Figure 11 and Figure 12 (crosses). Figure 11 and Figure 12 show the results for measurements taken at chamber pressures of 2 microtorr and 5.5 microtorr respectively.

Counting statistics of 1% or better were achieved for both measurements using electron currents between 25 and 30 microamperes and data accumulation times of 20 seconds.

The full curves in Figure 11 and Figure 12 represent the excitation function of the He contribution to the total signal. They are constructed of averaged data from the measurements of van Eck and de Jongh (1970) [92], Donaldson et al (1972) [25], Westerveld et al (1979) [100], and Shemansky et al (1985) [79]. The strong polarization of the He resonance radiation is also taken into account using the data summarized in the work of Westerveld et al (1979) (see Figure 13). Table 1 and Table 2 give all the relevant quantities needed for this construction. Numerical values are tabulated in Table 3. Finally, the combined He and He+ excitation functions were normalized to their constructed He resonance curves below the lowest threshold for He+ emission (65.4 eV). As can be seen from Figure 11 and Figure

Figure 11: $q'(He \& He^+)$ (x), $q'(He)$ (-), and $q'(He^+)$ (o) versus electron impact energy for a chamber pressure of 2 microtorr.

Axis labels:
$g'(90°)$ $(\times 10^{-21} cm^2)$

Vertical axis ticks: .8, 1.6, 2.4, 3.2

Horizontal axis: Electron Energy (eV) — 50, 100, 150, 200, 250
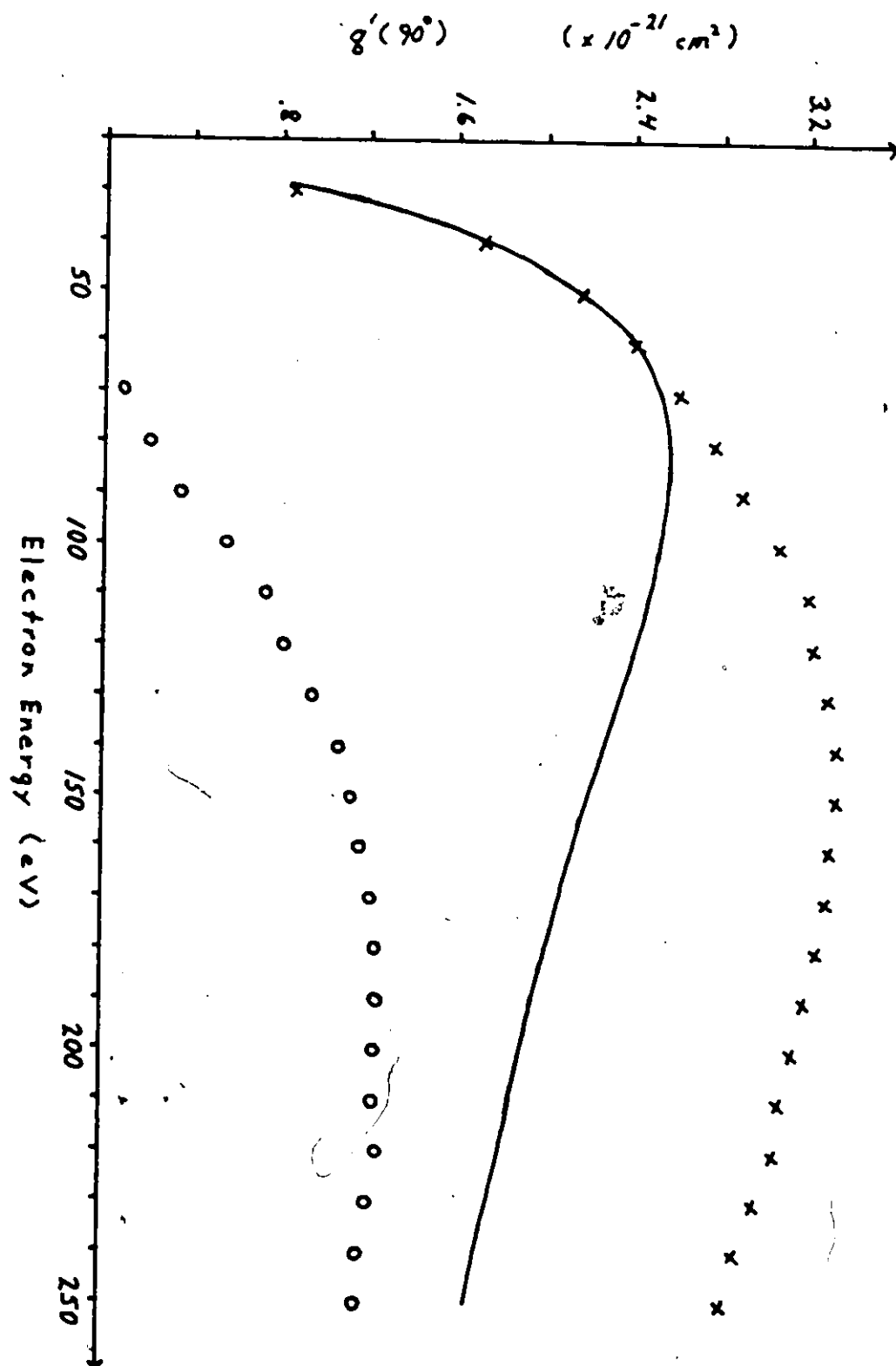
Figure 12: $q'(He\&He^+)$ (x), $q'(He)$ (-), and $q'(He^+)$ (o) versus electron impact energy for a chamber pressure of 5.5 microtorr.

$q'(90°)$ $(\times 10^{-21} cm^2)$

3.2

2.4

1.6

.8

Electron Energy (eV)

50

100

150

200

250
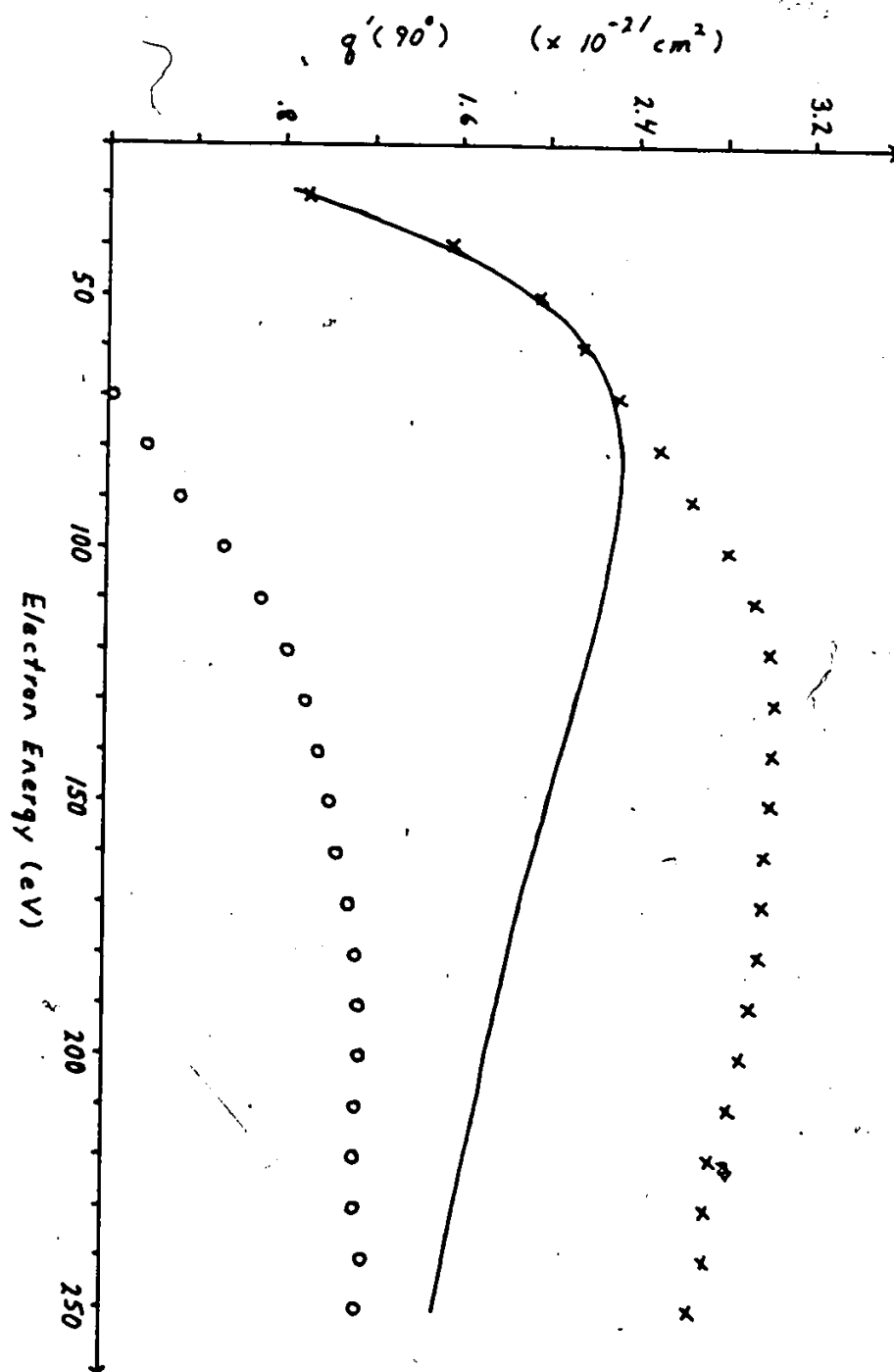
12   good agreement between the constructed excitation func-
tions and the measured excitation functions below 65 eV is
obtained.

Upon subtracting the He resonance contribution from the
measured excitation functions, curves representing the radi-
ation arising from the $n^2P \longrightarrow 1^2S$ transitions of Fe⁺ are
obtained (circles in Figure 11 and Figure 12).   The aver-
age of the two sets of He⁺ data are tabulated in Table 4.
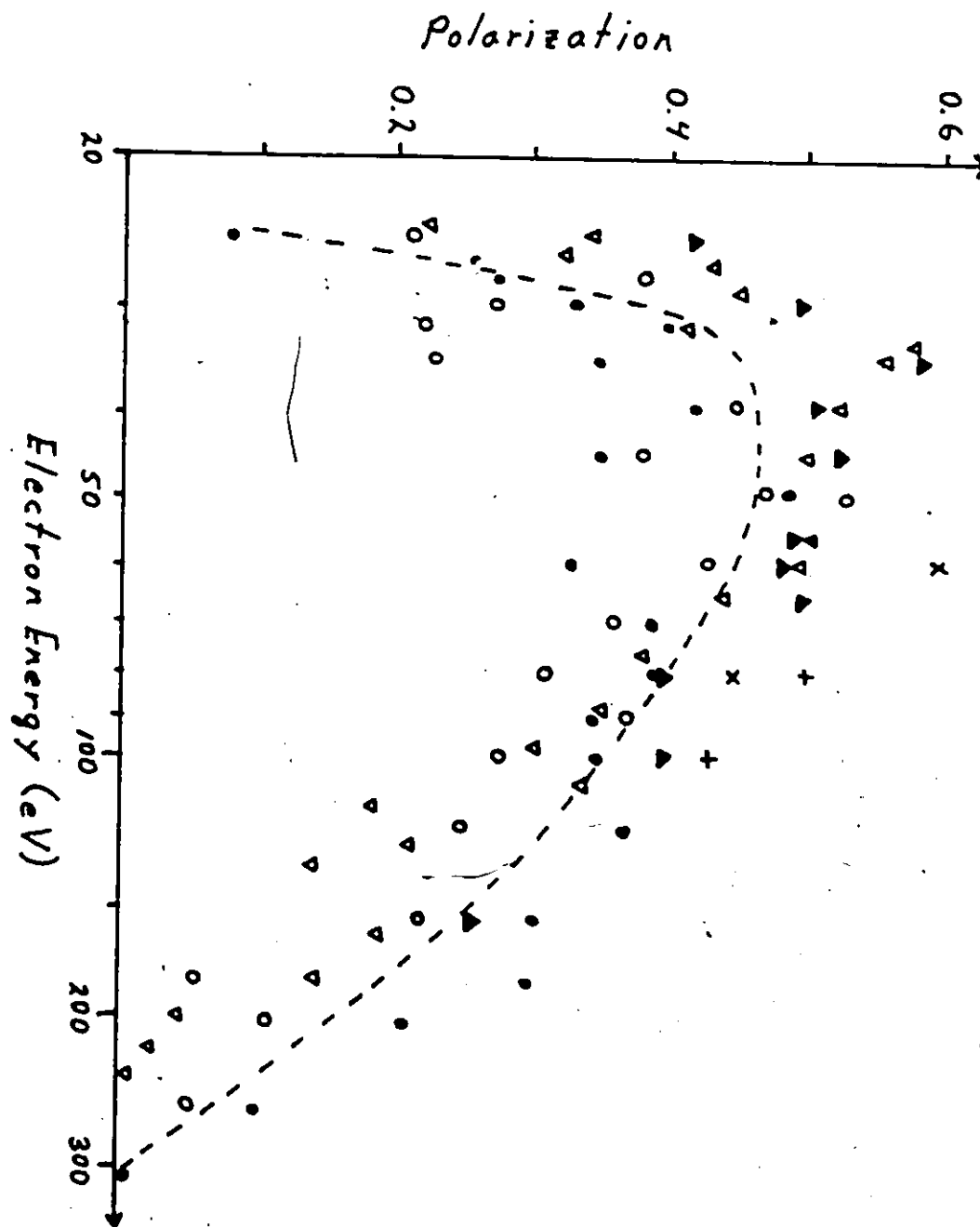
Figure 13: Helium polarization data. Taken from Westerveld et al [99]. ● 2^1P-1^1S, ○ 3^1P-1^1S Westerveld et al [99], ▽ 3^1P-2^1S Heddle and Lucas (1963), ▲ Σn^1P-1^1S Mumma et al (1974), and x 2^1P-1^1S, + 3^1P-1^1S Standage (1977).

TABLE 2

Average effective cross sections and polarizations as a function of electron impact energy for transitions in helium

Energy (eV)	Cross Sections ($\times 10^{-19}$ cm^2)				Polarization(f) P(E) ± .07
	2^1P-1^1S(b)	3^1P-1^1S(b)	4^1P-1^1S(c)	n≥5^1P-1^1S(e)	
30	49.7(a)	9.4(a)	3.5(d)	4.3	0.40
40	80.4	16.0	6.4	7.9	0.46
50	96.0	19.9	8.7	10.7	0.46
60	108.5(a)	23.8(a)	9.9(d)	12.1	0.45
70	108.5(a)	27.1(a)	10.6(d)	13.0	0.45
80	110.0(a)	26.7(a)	11.4(d)	13.0	0.42
90	110.9(a)	28.4(a)	11.0(d)	13.9	0.40
100	109.5	27.9(a)	11.0(d)	13.5	0.37
120	106.7	27.7(a)	10.8(d)	13.5	0.35
150	99.1	25.2	10.2	13.2	0.31
200	88.5	22.7	9.1	12.6	0.25
250	80.3	20.3	8.0(d)	11.1	0.16
				9.8	0.08

(a) Average of Westerveld et. al.[100] and Donaldson et. al. [25].
(b) Average of (a) and de Jongh et. al. [23]. (± 10%)
(c) Average of Donaldson et. al. [25] and van Eck et. al. [92]. (± 20%)
(d) Donaldson et. al. [25]. (± 38%)
(e) Shape of 4^1P-1^1S excitation function normalized to the data of Shemansky et. al. [79] at 200 eV. (± 40%)
(f) Westerveld et. al. [100].

TABLE 3

q'(E,He) and F(E) as functions of electron impact energy

$$q'(\text{He}) \times 10^{-21} \text{cm}^2$$

Energy (eV)	P = 1.4 µTorr (± 12%)	P = 4.9 µTorr (± 13%)	F(E)[a] (± 20%)
30	0.95	0.90	–
40	1.74	1.50	–
50	2.15	1.94	–
60	2.41	2.18	–
70	2.52	2.30	0.000
80	2.56	2.33	0.038
90	2.56	2.32	0.054
100	2.52	2.28	0.061
110	2.46	2.24	0.065
120	2.41	2.19	0.068
130	2.34	2.13	0.070
140	2.26	2.06	0.072
150	2.20	2.00	0.073
160	2.13	1.94	0.074
170	2.06	1.88	0.076
180	2.01	1.83	0.076
190	1.95	1.78	0.077
200	1.90	1.74	0.078
210	1.85	1.69	0.078
220	1.80	1.64	0.078
230	1.76	1.59	0.079
240	1.71	1.55	0.079
250	1.66	1.51	0.079

(a) $F(E) = \sum_{i \geq 3} q(i1,E,\text{He}^+)/q(21,E,\text{He}^+)$

TABLE 4

q'(E,He & He$^+$) and q'(E,He$^+$) as functions
of electron impact energy

Energy (eV)	q'(He & He$^+$)[a]		q'(He$^+$)		
	1.4 µTorr ($\pm$ 7.2%)	4.9 µTorr ($\pm$ 6.8%)	1.4 µTorr $+ .13 - .38$	4.9 µTorr $+ .13 - .36$	Average (10^{-21} cm^2)
30	0.85	0.91	-0.10	0.00	-0.05 $\pm$ .10
40	1.71	1.55	-0.03	0.05	0.01 $\pm$ .17
50	2.16	1.96	0.02	0.02	0.02 $\pm$ .21
60	2.40	2.16	-0.01	-0.02	-0.02 $\pm$ .23
70	2.60	2.32	0.08	0.02	0.05 $\pm$ .25
80	2.76	2.51	0.20	0.18	0.19 $\pm$ .26
90	2.90	2.65	0.34	0.33	0.34 $\pm$ .26
100	3.06	2.82	0.55	0.53	0.54 $\pm$ .26
110	3.20	2.94	0.73	0.70	0.72 $\pm$ .26
120	3.22	3.01	0.81	0.82	0.82 $\pm$ .26
130	3.29	3.03	0.95	0.90	0.92 $\pm$ .26
140	3.33	3.02	1.07	0.96	1.02 $\pm$ .25
150	3.33	3.02	1.13	1.02	1.07 $\pm$ .25
160	3.30	2.99	1.16	1.05	1.11 $\pm$ .24
170	3.29	2.99	1.22	1.11	1.16 $\pm$ .24
180	3.25	2.97	1.24	1.14	1.19 $\pm$ .23
190	3.19	2.93	1.24	1.15	1.20 $\pm$ .23
200	3.14	2.89	1.24	1.15	1.19 $\pm$ .22
210	3.08	2.83	1.23	1.14	1.18 $\pm$ .22
220	3.06	2.75	1.25	1.11	1.18 $\pm$ .21
230	2.96	2.73	1.21	1.14	1.17 $\pm$ .21
240	2.87	2.73	1.18	1.17	1.17 $\pm$ .20
250	2.82	2.66	1.16	1.15	1.16 $\pm$ .20

(a) Normalized to q'(E,He) for E $\geq$ 65 eV.
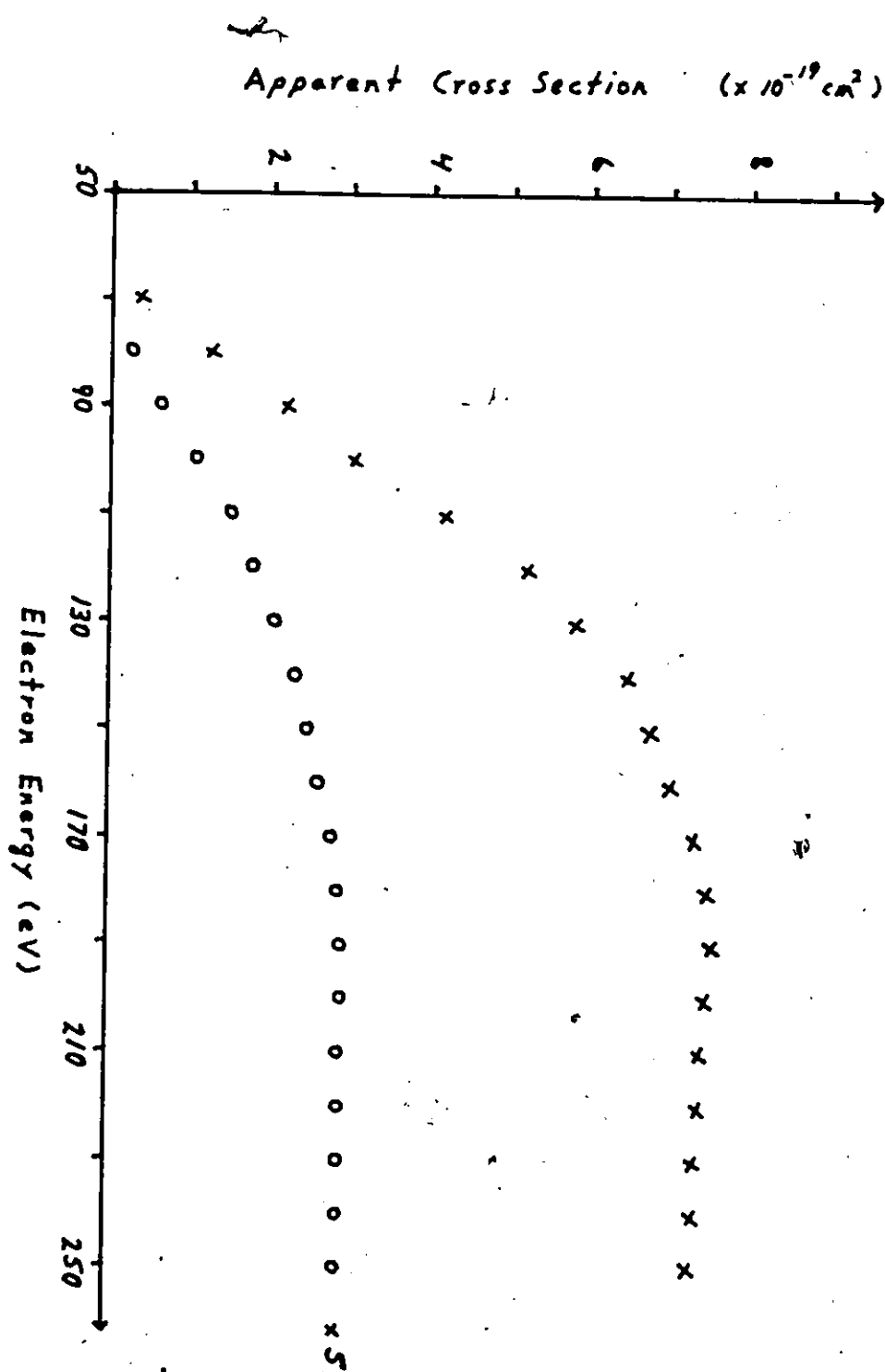
Figure 14: He$^+$ 2^2P-1^2S apparent cross section (x) and $\sum_{n\geq3}$ n^{2}P-1^2S apparent cross section (o) versus electron impact energy. Note the multiplier.

4.4.2   Near-Threshold Region

Figure 15 shows the near-threshold region of the He+ excitation function (crosses).   The curve was obtained by ramping over the 50 to 100 eV energy range for several hours, integrating over 5 channels (0.94 eV; approximately the resolution of our electron beam), and subsequently performing the same procedure as discussed above.   The chamber pressure was 2 microtorr.   Consequently, D(P) equalled 0.977.   The onset of the 30.4 nm $2^2P \to 1^2S$ line at 65.4 eV was used to calibrate the energy scale.   Note that there is only a slight indication of an upward trend near 73 eV corresponding to the onset of the n=3 state (25.6 nm line) and higher states.   This confirms previous measurements (Moustafa Moussa and de Heer [65]) and calculations (Shemarsky et al [79]) which indicated that the cross section for exciting the higher ^2P states declines rapidly with increasing principle quantum number.   However, if we assume the shape of the He+ $2^2P \to 1^2S$ and $n \geq 3 \, ^2P \to 1^2S$ excitation functions are linear near threshold, we can determine the ratio, $F(B)$, of the two differential cross sections.   The relevant equations are given by

$$\sum_{n=2}^{\infty} q'(n1;He+) = \sum_{n=3}^{\infty} q'(n1;He+) + q'(21;He+) \qquad (24a)$$

$$= b(E - E_2) + a(E - E_1) \qquad E > E_2 \qquad (24b)$$

$$= a(E - E_1) \qquad E_1 < E < E_2 \qquad (24c)$$

and

$$F(E) = \sum_{n=3}^{\infty} q(n1;E;He+)/q(21;E;He+) \qquad (25a)$$

$$= \frac{T(21)C(21) \sum_{n=3}^{\infty} q'(n1;E;He+)}{T \quad C \qquad q'(21;E;He+)} \qquad (25b)$$

$$= \frac{T(21)C(21) \quad b(E - E_2)}{T \quad C \qquad a(E - E_1)} \qquad (25c)$$

where E_1 and E_2 are the respective threshold energies ($E_1 = 65.4$ eV and $E_2 = 73$ eV).

Performing a statistically weighted least squares fit of our data to equation (24b) results in a value of b/a=0.109. Using the filter transmissions and quantum efficiencies from Table 1 gives

$$F(E) = (0.078 \pm 20\%) \times (E - E_2)/(E - E_1) \qquad (26)$$

for $E > E_2$.

Figure 15 shows the straight lines corresponding to the 2^2P --> 1^2S transition (dashed line) and the $n \geq 3^2P$ --> 1^2S transitions (solid line). Note the excellent agreement in the energy range below 73 eV. This procedure is expected to be valid for electron impact energies up to 110 eV due to the linearity of the He+ excitation function in this range (see

some of the previous figures). A plot of $P(E)$ is shown in Figure 16. Tabulated values are given in Table 3.

Figure 15: Near threshold excitation functions. $q'(21,He^+)$ (----), $\sum_{n\geq 3} q'(nl,He^+)$ (——), and $\sum_{n\geq 2} q'(nl,He^+)$ (x). The pointers correspond to the 30.4 nm threshold at 65.4 eV and the 25.6 nm threshold at 73 eV.

$8'(He^+)$　　　(Arbitrary units)

Electron Energy (eV)

65·4

73
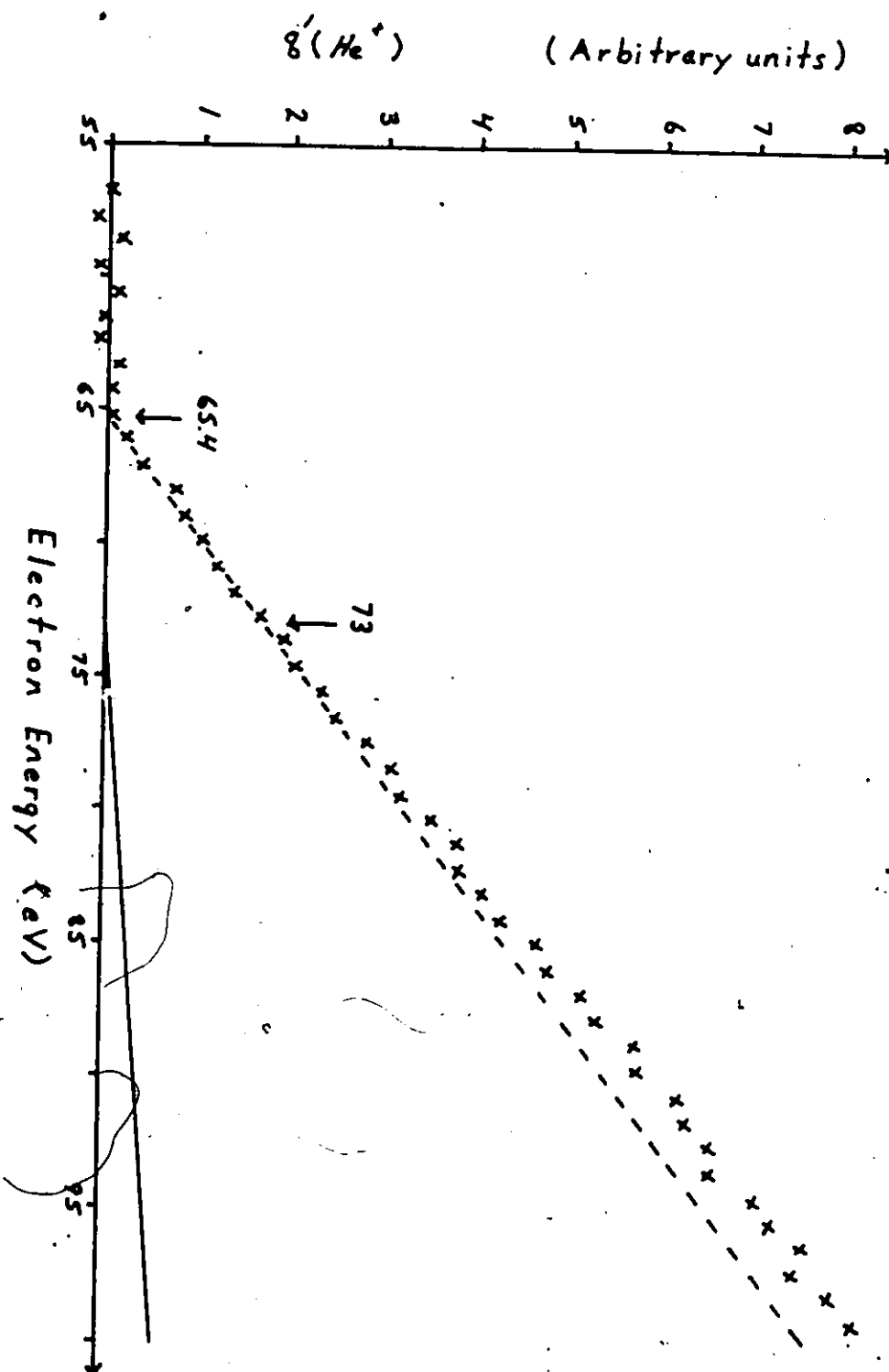
4.4.3 The High-Energy Region

In the regime of high impact energies, the monochromator had to be used to isolate the 30.4 nm line which was observed in second order. Relative excitation function measurements were made for incident electron impact energies from 200 to 1000 eV. Using the shape of the excitation function and the simple assumption that the He$^+$ n$\geq$2p --> 1^{2}S excitation function is proportional to the He$^+$ 2^{2}p --> 1^{2}S excitation function shifted by an amount equal to E_2-E_1 (=7.6 eV), we can determine F(E) for all electron impact energies. This statement can be expressed as follows:

$$F(E) = M \frac{q(21;E+E_1-E_2;He^+)}{q(21;E;He^+)} \tag{27}$$

where q(21;E;He$^+$) is given by the measured excitation function. The scaling factor, M, was determined by equating equations (26) and (27) under the assumption that q(21;E;He$^+$) is proportional to (E-E$_1$). In this way it can be shown that M=0.0784. Figure 16 shows our calculated values for F(E) from threshold to 350 eV.

$$F(E) = \sum_{n \geq 3} q(n1; E) / q(21; E)$$
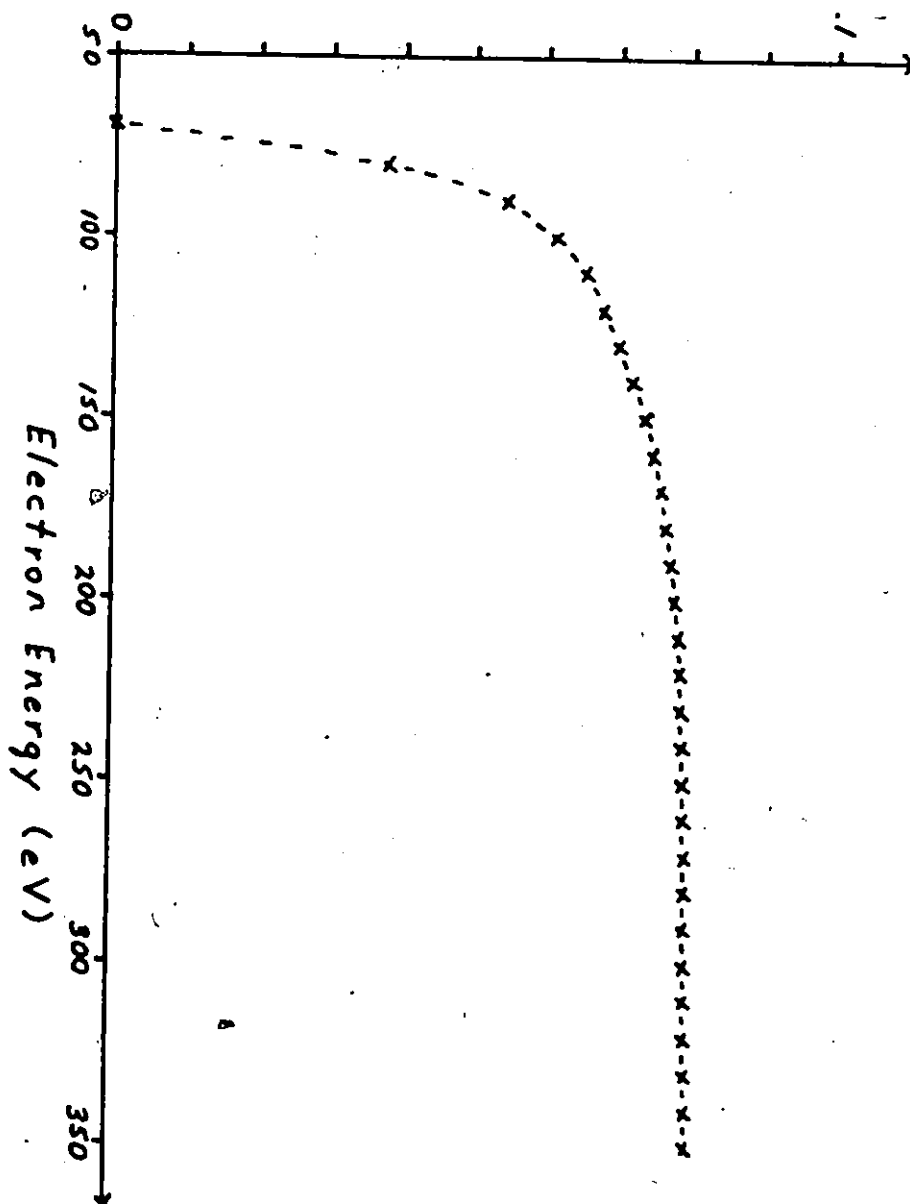
Figure 1·6: F(E) versus electron impact energy.

4.4.4   Determination of Q(30.4 nm)

Using equations (1) to (17) and the values tabulated in
Table 1 to Table 4 the apparent cross section for the He+
2²P --> 1²S transition can be determined.   A graph of the
results for energies below 250 eV is shown in Figure 14.
Figure 17 shows a plot for all energies up to 1000 eV along
with a plot of Q(21)xE.   The results are also tabulated in
Table 5.   The high energy results were normalized to the low
energy results at 200 eV.   The QxE plot illustrates the
optically forbidden nature of the simultaneous ionization-
excitation process as expected.

Figure 17: Apparent cross section (not corrected for
cascade or polarization) and $Q \times E$ plot, □, for
the He^+ $2^2P - 1^1S$ transition. o; $E < 250$ eV;
X, $E \geq 250$ eV.

Apparent Cross Section $(\times 10^{-19} cm^2)$

Electron Energy (eV)
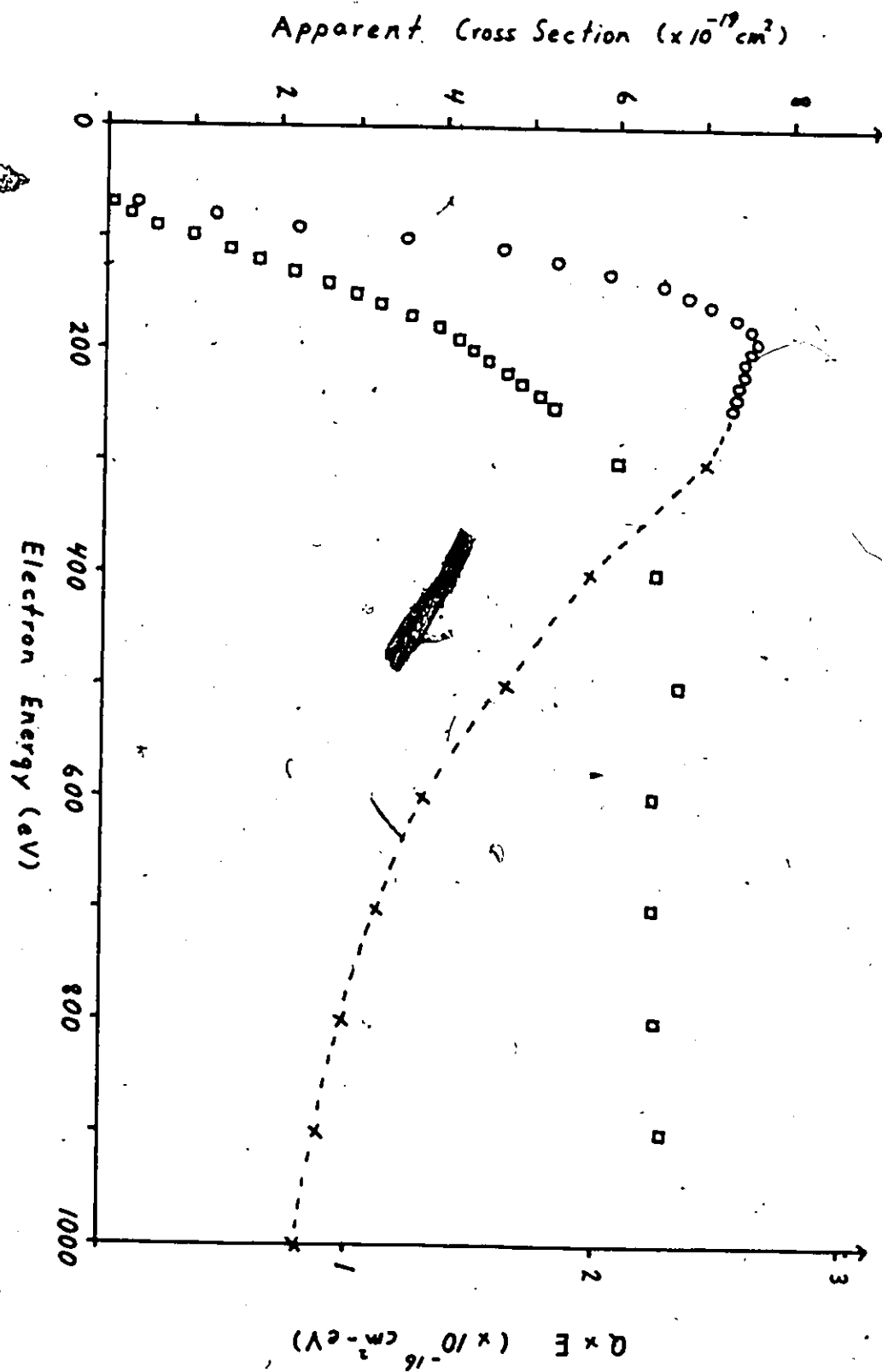
$Q \times E$ $(\times 10^{-16} cm^2-eV)$

TABLE 5

Apparent cross sections[*]
as a function of the electron impact energy

Energy (eV)	$\sum_{n \geq 3} Q(n1, He^+)$ (x $10^{-19} cm^2$)	$Q(21, He^+)$ (x $10^{-19} cm^2$)	$Q(21)$ x E (x $10^{-16} cm^2$-eV)
70	–	0.4 ± 1.8	0.0 ± 0.1
80	0.05 ± 1.8	1.2 ± 1.8	0.1 ± 0.1
90	0.12 ± 1.8	2.2 ± 1.7	0.2 ± 0.2
100	0.21 ± 1.8	3.5 ± 1.7	0.4 ± 0.2
110	0.30 ± 2.0	4.6 ± 1.8	0.5 ± 0.2
120	0.35 ± 2.0	5.2 ± 1.8	0.6 ± 0.2
130	0.41 ± 2.1	5.8 ± 1.8	0.8 ± 0.2
140	0.46 ± 2.2	6.4 ± 1.7	0.9 ± 0.2
150	0.49 ± 2.2	6.7 ± 1.7	1.0 ± 0.3
160	0.52 ± 2.2	7.0 ± 1.7	1.1 ± 0.3
170	0.55 ± 2.2	7.3 ± 1.7	1.2 ± 0.3
180	0.57 ± 2.2	7.5 ± 1.7	1.4 ± 0.3
190	0.58 ± 2.2	7.5 ± 1.7	1.4 ± 0.3
200	0.58 ± 2.2	7.5 ± 1.6	1.5 ± 0.3
210	0.58 ± 2.2	7.4 ± 1.6	1.6 ± 0.3
220	0.58 ± 2.1	7.4 ± 1.5	1.6 ± 0.3
230	0.58 ± 2.1	7.3 ± 1.5	1.7 ± 0.4
240	0.58 ± 2.1	7.3 ± 1.5	1.8 ± 0.4
250	0.57 ± 2.1	7.3 ± 1.5	1.8 ± 0.4
300	–	7.0 ± 1.5	2.1 ± 0.5
400	–	5.6 ± 1.3	2.2 ± 0.5
500	–	4.7 ± 1.0	2.3 ± 0.5
600	–	3.7 ± 0.8	2.2 ± 0.5
700	–	3.2 ± 0.7	2.2 ± 0.5
800	–	2.8 ± 0.6	2.2 ± 0.5
900	–	2.5 ± 0.6	2.3 ± 0.5
1000	–	2.3 ± 0.5	2.3 ± 0.5

[*] Not corrected for cascade or polarization.

4.5   Discussion

Figure 18 shows our (open circles) absolute emission cross section for the 30.4 nm line for electron impact energies from threshold to 300 eV.   Also shown are the results of three previous measurements, which like ours are not corrected for either cascade or polarization.   Bloemer et al (1981) [15] made only a single absolute measurement at 200 eV (open triangle) and suggested a renormalization of their previously reported curve (open squares) (Moustafa Moussa and de Heer [65]).   Their most recent result is closer to our cross section, and in fact, the measurements are within each other's error bars. However; Bloemer et al use a value for P(200eV) of 0.38.   This value can be determined from their ratio $I_0(2)/I_0(1)$, where $I_0(n)$ is the number of photons entering their ionization chamber per second corresponding to the He$^+$ $(n+1)^2P$ to 1^2S transition. In order to reach the ionization chamber the photons must pass through an aluinum foil filter.   Thus their ratio can be reexpressed as

$$I_e(2)/I_0(1) = t(2)Q(31)/t(1)Q(21) \qquad (28a)$$
$$= 0.43 \pm 0.23$$
or
$$Q(31)/Q(21) = P(200) = t(1)I_e(2)/t(2)I_0(1) \qquad (28b)$$
$$= 0.39$$

where $t(n)$ are their filter transmissions and $Q(n+1,1)$ are the effective cross sections.   If we use their value for P(200) in our calculations, instead of 0.078 (our value at

200 eV), our apparent cross section becomes 5.43 x 10⁻¹⁹ cm² at 200 eV (I), which is very close to the result of Bloemen et al. The points represented by the solid circles are given by Porand et al [29]. They are the result of an earlier analysis (1984). The recent review of the analysis resulted in a number of changes. First, we had employed quantum efficiencies from Galileo for our 4039C CEM. However, they do not provide reliable values for radiation below 50 nm, and since it is the ratio of the quantum efficiencies at 58.4 nm and 30.4 nm which is important in our calculations, we decided not to use Galileo's data in our present calculations. Secondly, we have found it necessary to compensate for radiation trapping, especially for the data taken at a chamber pressure of 5.5 microtorr. Nevertheless, renormalization of their data to our present data using a factor of 1.2 gives results in good agreement at all energies.

A quantitative statement on cascade is rendered difficult, since no reliable cross section data for transitions terminating in the 2^2P state are available. However, as the cross sections for exciting higher states in He⁺ are believed to decline very rapidly with increasing principle quantum number [79], cascade is not expected to play an important role. Our values for P(E) are in support of this statement. Also, if one assumes the situation is hydrogenic, we should not expect cascade to contribute more than 4

Figure 18: Absolute emission cross sections for the He$^+$
2^2P-1^2S transition versus electron impact energy.
Present results (o), present result (F(200) =
0.38) (x), Forand et al (●), Bloemen et al (△),
and Moussa et al (□).

Cross Section $(\times 10^{-19} \text{ cm}^2)$

2   4   6   8

50   90   130   170   210   250   290

Electron Energy (eV)
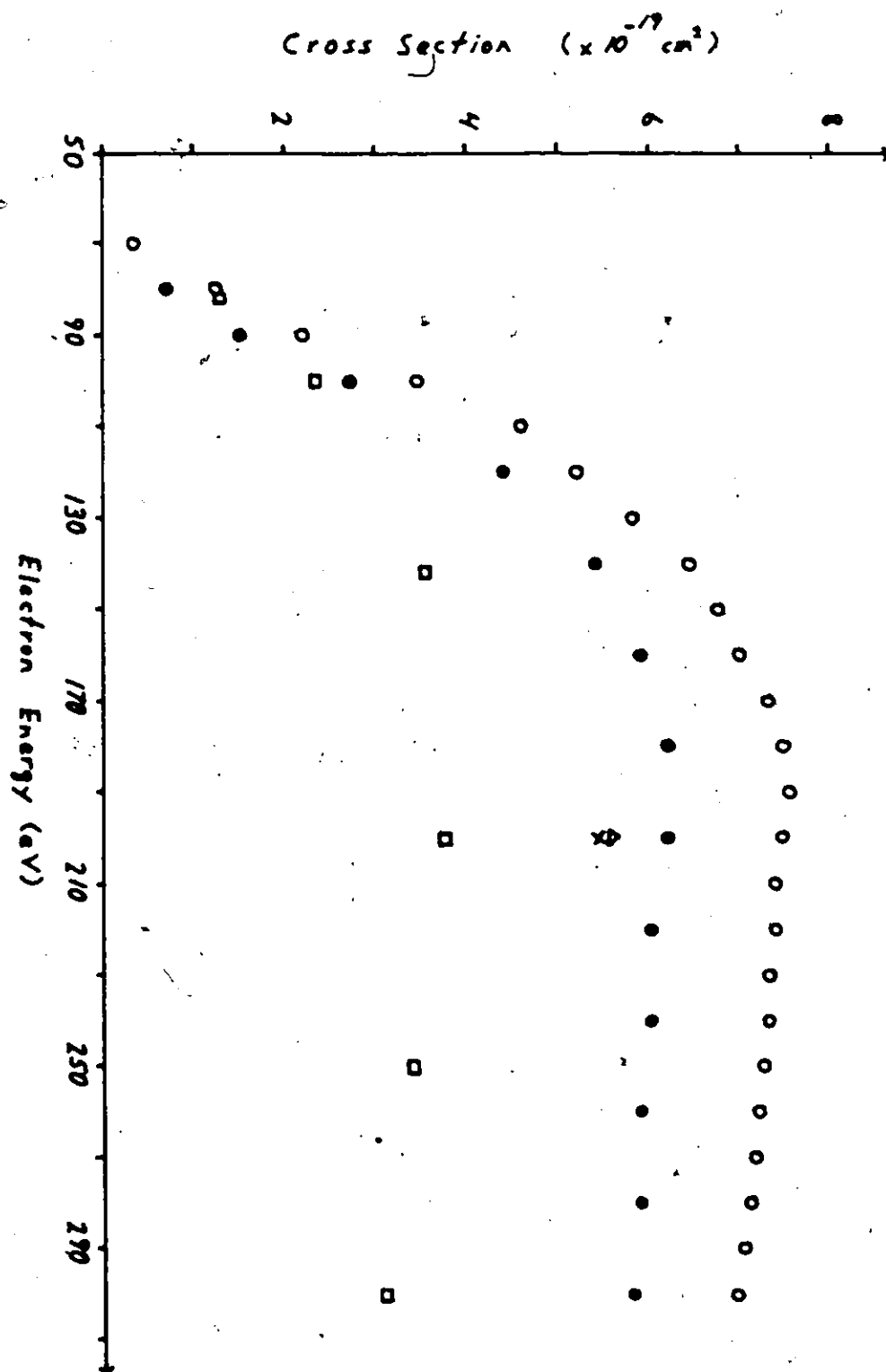
percent (see Appendix C). It is also interesting tc note that our value for P(E) is not consistent with the n^{-3} rule.

It is also difficult to estimate the effect of possible polarization of the 30.4 nm radiation on the cross section. In fact, only the polarization of the n=4 --> n=3 manifold at 468.6 nm has been measured (Elenbaas 1930 [26], Haidt and Kleinpoppen 1966 [33]) and a threshold polarization of 0.13 was found in the latter experiment. However, this result is not relevant to our case, since the 468.6 nm line is made up of all the allowed l'-->l transitions, whereas the 30.4 nm line is a pure l'=1 to l=0 transition. On the other hand, if it is assumed that the Percival-Seaton hypothesis (Percival and Seaton, 1958) [73] is applicable to the simultaneous ionization-excitation process, a threshold polarization of $p(th)=3/7=0.429$ and a high-energy limit of $p_\infty=-3/11=-0.273$ should be expected for the subsequently emitted (unresolved) $2^2P_{1/2,3/2}$ --> $1^2S_{1/2}$ doublet. Note that He has zero nuclear spin, thus the polarization is not attenuated by hyperfine perturbations. Such a strongly polarized emission would, of course, affect the shape of the measured 30.4 nm cross section through the anisotropy factor $(1 - p/3)$ where p is the energy-dependent polarization of the radiation. On the other hand, we do not expect the normalization at 200 eV to be seriously affected, since in this energy range, well away from threshold and infinity, the polarization is likely to be small. A polarization of 10% would lead to a 3% change in the cross section.

4.6   Summary

We have presented a fairly simple and straightforward
approach to measure the cross section for emission of the
He$^+$ 2^2P --> 1^2S line at 30.4 nm following electron impact on
He.   A value of $(7.5 \pm 1.6) \times 10^{-19}$ cm^2 at 200 eV impact
energy was found.   Using our threshold data and some simpli-
fying assumptions we have also calculated the ratio $F(E)$ of
the radiation emitted from the $n \geq 3^2F$ --> 1^2S transitions to
that emitted from the 2^2P --> 1^2S transition of He$^+$.   This
enables us to determine a total cross section for both Σn^2P
--> 1^2S ($n=2,3,...$) and Σn^2P --> 1^2S ($n=3,4,...$).   For any
energy they are given by $(1 + F(E)) Q(21;E)$ and $F(E) Q(21;E)$
respectively.   The difference between our value for $F(200)$
and that of Bloemen et al appears to be one reason for the
discrepancy between the two results.   However, other prob-
lems are inherent in our experiment.   The principal reasons
for our large error bars are the current lack of reliable
data concerning the quantum efficiency of our CEM,   the
errors currently associated with the helium resonance cross
sections and their polarizations,   and uncertainties with
respect to the amount of resonance trapping and the amount
of radiation emitted by the lower wavelength transitions.
With respect to the quantum efficiency of CEM's, more accu-
rate data which can be directly linked to our CEM is needed.
Such improvements could substantially lower the error margin
and along with polarization measurements currently planned

in our laboratory could greatly improve the applicability of the 30.4 nm cross section as a reliable calibration standard in the extreme ultraviolet.

Chapter V

DISSOCIATIVE EXCITATION OF SF_6

5.1   Introduction

The purpose of this study is to look at the VUV radiation
which is emitted following electron impact on SF_6.   At elec-
tron impact energies of 200 eV it was found that no measura-
ble radiation could be identified as being due to molecular
transitions.   All the radiation could be identified with
atomic transitions in fluorine (F),   singly-ionized fluorine
(F+), sulfur (S), or singly-ionized sulfur (S+).   Only a
slight indication of a doubly-charged sulfur (S++)   tran-
sition could be seen.   Such information is important for
several reasons.   Since SF_6 is commonly used in high volt-
age devices as an insulator, it is important to understand
the type of processes which occur when it breaks down.   Sec-
ondly, like the inert gases, it is relatively inert.   This
property arises due to its spherical symmetry (no permanent
dipole) and because there are no electrons free to form
additional molecular bonds.   Lastly, since many inert gases
have been studied using electron impact, it is interesting
to study a moderately complex molecule which has many of the
properties associated with the inert gases.

5.2   Experimental

5.2.1   Apparatus

The apparatus consists of a crossed electron-beam gas-beam arrangement in conjunction with a VUV monochromator. An electron beam of 20 to 600 eV ($\Delta E_{FWHM} = 0.3$ eV) with a current of 20 to 125 microamperes intersects at right angles a gas beam of SF_6 molecules (instrument grade; purity 99.95%) effusing from a multi-capillary array. The number density of the gas was continuously monitored by measuring the head pressure (typically 60 to 100 mTorr) in the gas line with a MKS Instruments capacitance manometer. It was also convenient to use a pulsed supersonic gas beam using a piezoelectric Lasertechnics Model LPV molecular-beam valve equipped with a 0.15 mm nozzle for the initial spectral surveys due to its ability to produce a high number density of the target molecule in the interaction region. The VUV impact radiation, observed perpendicular to the plane defined by the electron and gas beams, was dispersed by a half-meter Seya-Namioka monochromator and detected using a channel electron multiplier connected to a standard pulse counting system. The information was stored in a multi-channel analyser (TN-1710) and transferred later into a computer (IBM 9001) for analysis. Below 130 nm, a gold-coated grating blazed at 70 nm with 1200 grooves/mm (reciprocal linear dispersion 1.7 nm/mm) was used with a Mullard 419 BL detector, while for wavelengths above 130 nm, an aluminum

and MgF_2 coated grating with 1200 grooves/mm (reciprocal
linear dispersion 1.7 nm/mm) was used with a caesium iodide
coated Galileo Electro-Cptics BX 7600-4413 detector.
Throughout this experiment, we did not operate at the magic
angle because we assumed that the radiation was isotropic
(zero polarization). This is in line with previous studies
of dissociative excitation into atomic fragments of all but
the very simplest of molecules [56] [41]. However, we did
operate at the orientation necessary to correct for instru-
mental polarization effects.

5.2.2   Calibration Procedure

Becker and McConkey [11] and Becker et al [12] have
discussed the absolute calibration of the detection equip-
ment above and below 120 nm respectively. Similar tech-
niques were used in this work. Basically the known cross
sections of the rare gas resonance transitions are used to
establish the calibration below 110 nm, while the cross sec-
tion for Lyman alpha production from H_2 is used at higher
wavelengths. The molecular branching ratio technique [57]
[1] was used (CO, fourth positive system, and H_2, Werner
system) to provide relative calibration points. Very recent
work [78] [95] [50] [104] on Lyman alpha excitation has
shown that the previously accepted cross section [67] is
too high. We adopt the value 7.09×10^{-18} cm^2 at 100 eV
impact energy, which is the value we have recently deter-
mined in our laboratory [104] (or see Chapter 7), as our

standard. It is different from the value 7.6×10^{-18} cm^2 used in our earlier paper on SP. [29]. Using the average ratio between the H_2 Lyman alpha cross sections at 100 eV and 200 eV electron impact energy given by Mumma and Zipf [67] and McConkey and Donaldson [59], and normalizing to our value at 100 eV, our cross section at 200 eV is 5.02×10^{-18} cm^2 The general effect of this change is to lower our previous results. However, the amount varies depending upon the reference cross section which was used.

Above 120 nm the accuracy of our relative calibration points is 10% or better except at the highest wavelengths around 180 nm where an extrapolation of our calibration curve [11] was necessary. Below 120 nm the accuracy depends on the precision of the available cross section data. In the region of the He resonance lines (52 - 60 nm) the accuracy is high (10%), but in other wavelength regions it is not better than 20 to 30% due to the scarcity of reliable data. For example, the Ne 73.6 nm emission has a claimed accuracy of only 30% (Tan et al [85]) and measured cross sections for the Ar+ lines at 92 and 93.2 nm differ by approximately 35% [85] [99]. Additional uncertainties are added due to the difficulty of deciding how to interpolate between the few data points. This inherent freedom is another reason for the differences between our previous results [29] and our present data.

The values which we have adopted for the various transitions are listed in Table 6 and the final relative calibration curves are shown in Figure 19 and Figure 20. The polarization data was obtained from Westerveld et al [99] for helium, Hammond [34] for neon, Dassen et al [22] for the argon resonance lines, and Ott et al [71] for H_2 Lyman alpha.

Count rates, in all cases were found to be proportional to the electron current but great care had to be taken when comparison of intensities at different pressures was made. Distinctly different intensity-pressure plots (see Figure 21 to Figure 29) were obtained for various transitions. Table 7 lists the parameters which were determined using a weighted least squares fit. The errors were determined using the statistical F-test at the 95% confidence level. Resonance trapping strongly affects the resonance lines, especially the He 58.4 nm line, Ar 104.8 nm line and the Ne 73.6 nm line. The other non-linear effect, where the intensity increases above what a linear increase would give, is due to changes in the flow characteristics of the gas through the orifice. This is consistent with findings from other laboratories using relative flow techniques [16]. The effect can be shown to be due to a change from molecular flow conditions into the regime of intermediate flow. The effect can also be used to determine molecular diameters. For SF_6 a value of 0.577 nm was obtained. Appendix A, Appendix B,

TABLE 6

Cross sections and polarizations at 200 ev electron impact energy for calibration below 125 nm

Line	λ (nm)	Effective Cross Section (a) (x 10^{-18} cm^2)	Polarization	Apparent Cross Section (b) (x 10^{-18} cm^2)	References
He I (4p-1s)	52.2	0.91 ± 20% (c)	0.16 ± .07	0.96 ± 20%	25,91,99
He I (3p-1s)	53.7	2.27 ± 10% (c)	0.16 ± .07	2.40 ± 11%	25,91,99
He I (2p-1s)	58.4	8.85 ± 10% (c)	0.16 ± .07	9.35 ± 10%	25,91,99
Ne I (3s-2p)	73.6	5.53 ± 30%	0.04 ± .02	5.60 ± 30%	84
Ar II (3s3p^6-3s^{2}3p^5)	92.0	4.58 ± 25% (c)	0	4.58 ± 25%	84,98
Ar II (3s3p^6-3s^{2}3p^5)	93.2	2.38 ± 25% (c)	0	2.38 ± 25%	84,98
Ar I (4s-3p)	104.8	15.60 ± 20%	0.00 ± .01	15.60 ± 20%	57
Ar I (4s-3p)	106.7	6.70 ± 20%	0.00 ± .01	6.70 ± 20%	57
H$_2$ (Lyman alpha)	121.6	5.02 ± 9%	0.02 ± .01	5.05 ± 9%	-

(a) Cascade included
(b) Corrected for polarization and cascade
(c) Average value from all the references
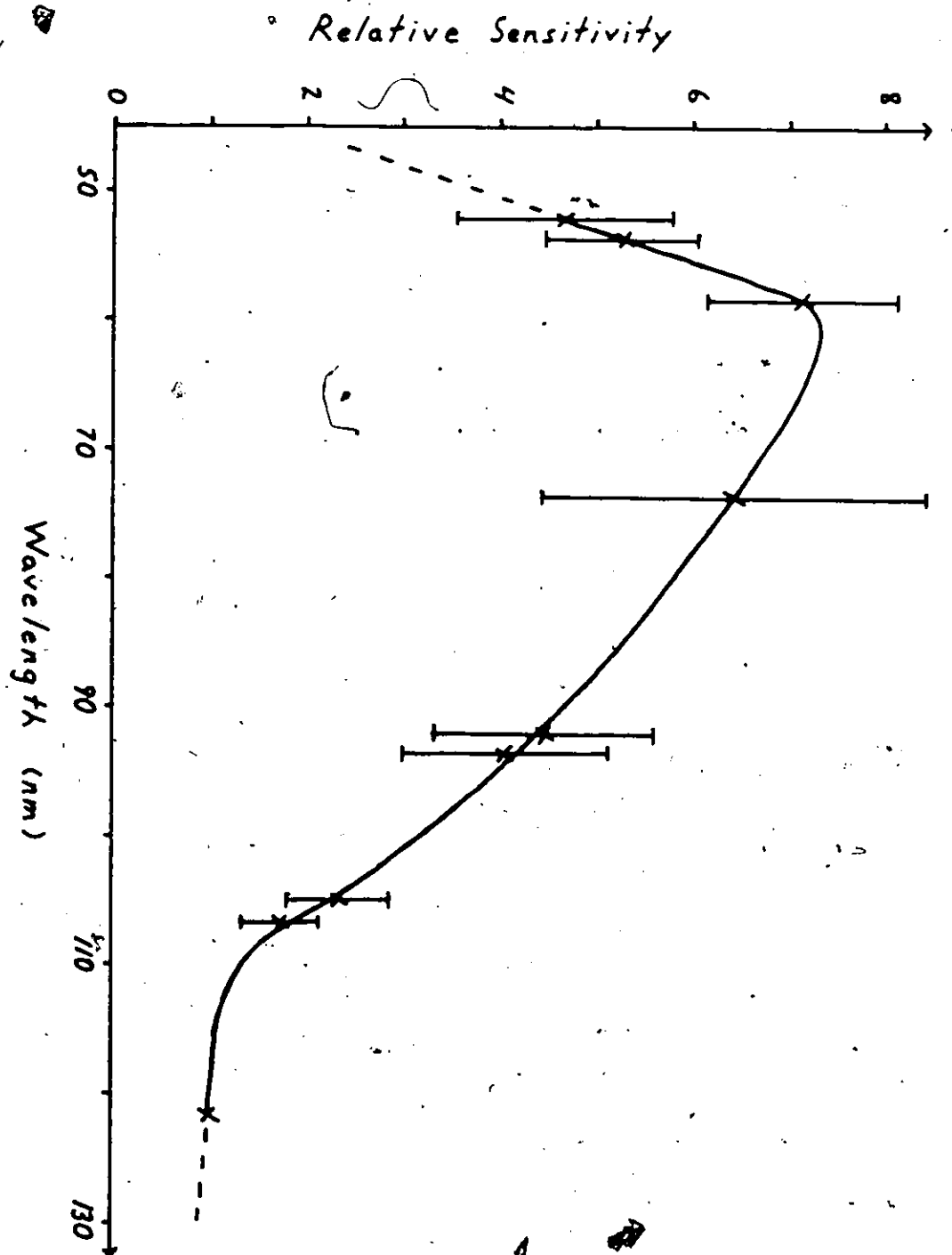
Figure 19: Relative detection sensitivity below 125 nm.
All data are normalized to H_2 Lyman alpha. The
dashed lines indicate extrapolation.
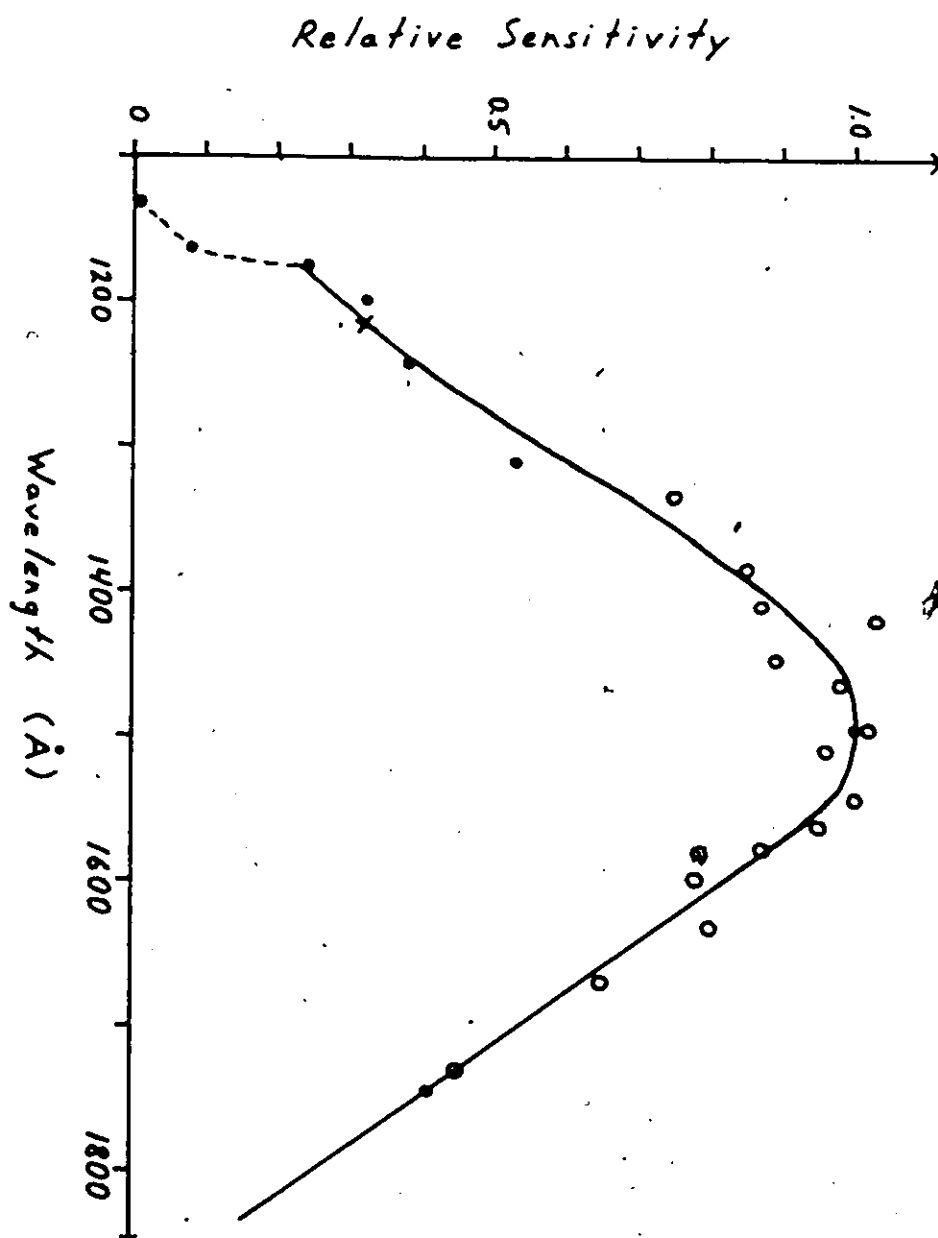
Figure 20: Relative detection sensitivity above 120 nm.
Data is taken from Becker and McConkey [11].
They have used a branching ratio technique and
the following emissions: CO (o); NI (•), and H_2
Lyman alpha (x). The dashed lines indicate the
MgF_2 cut-off or an extrapolation.

and Chapter 2 give more details regarding the technique. The poorer fit of the model in the case of resonance trapping is thought to be due to the breakdown of some of its simplifying assumptions. However, all our measurements were performed at lower pressures where the fit is excellent. A capacitance manometer was used for accurate head pressure measurements.

All absolute cross section measurements were carried out at an electron impact energy of 200 eV or 400 eV. The data were made absolute by comparison of the intensity of the particular emission under study with that of a convenient reference transition of known cross section (Table 6) excited under identical electron beam currents and known source pressures. Relative excitation functions were taken for many of the lines from threshold to 600 eV. The near threshold regions were investigated in detail by ramping the impact energy and using multichannel scaling techniques. This enabled us to measure the onset potentials to within 1.5 eV.

Figure 21: Intensity of the FI(95.5 nm) emission following
200 eV electron impact on SF_6 versus the source
pressure.
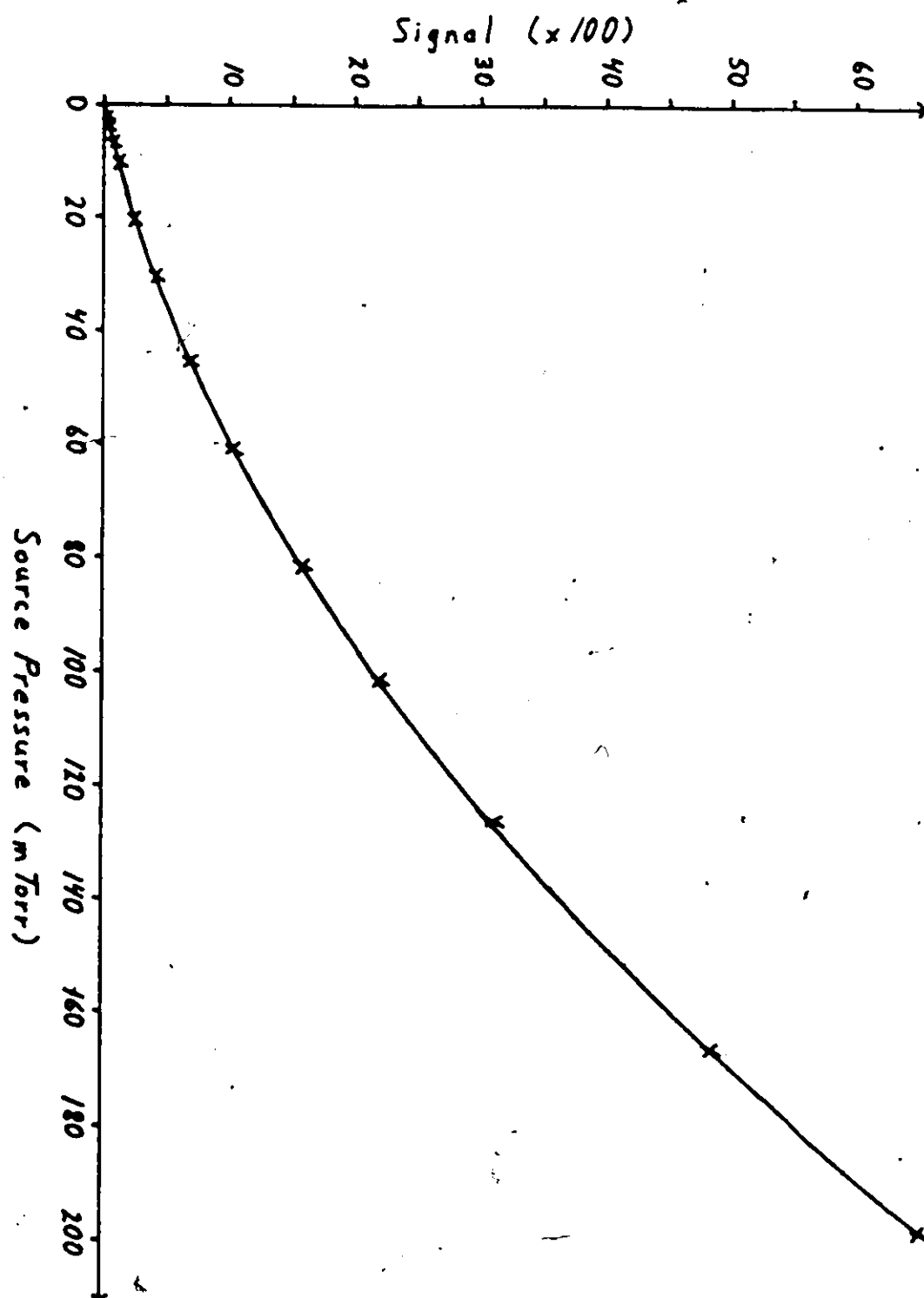
Figure 22: Intensity of the Lyman alpha emission following
200 eV electron impact on H_2 versus the source
pressure.

Signal (×100)

Source Pressure (mTorr)
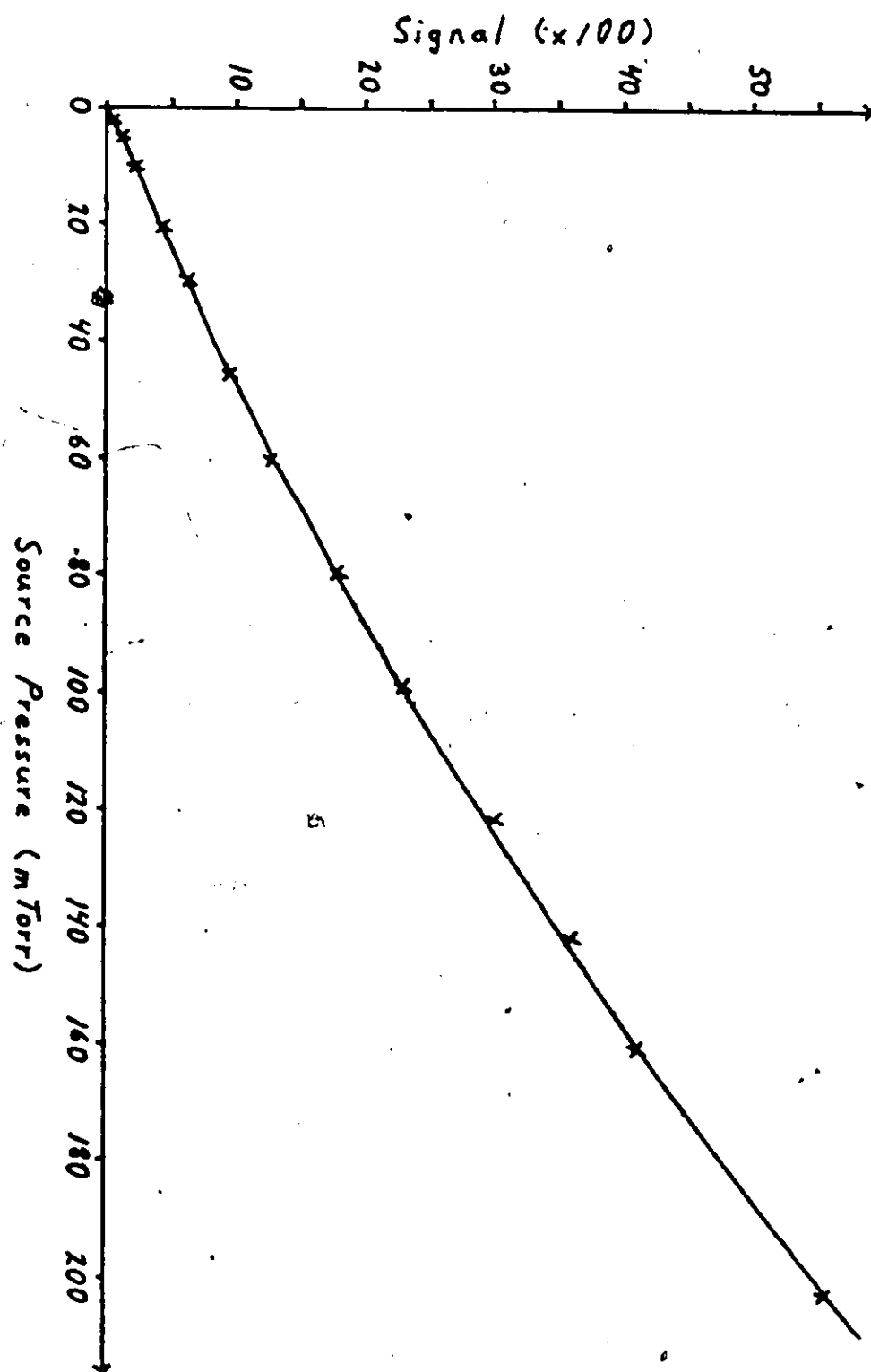
Figure 23: Intensity of the 58.4 nm emission following
200 eV electron impact on He versus source
pressure.
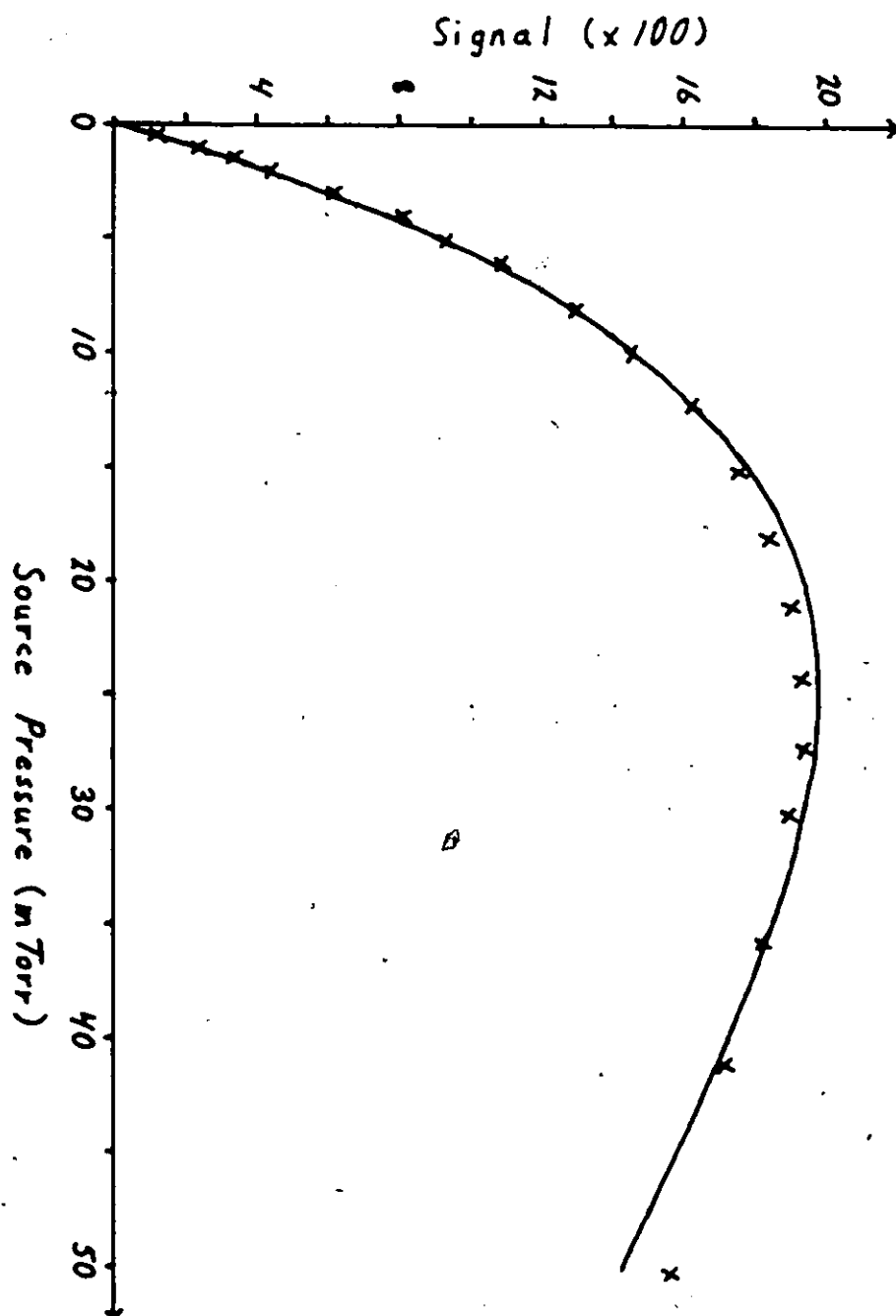
Figure 24: Intensity of the 53.7 nm emission following 200 eV electron impact on He versus source pressure.

Signal (x100)

Source Pressure (mTorr)
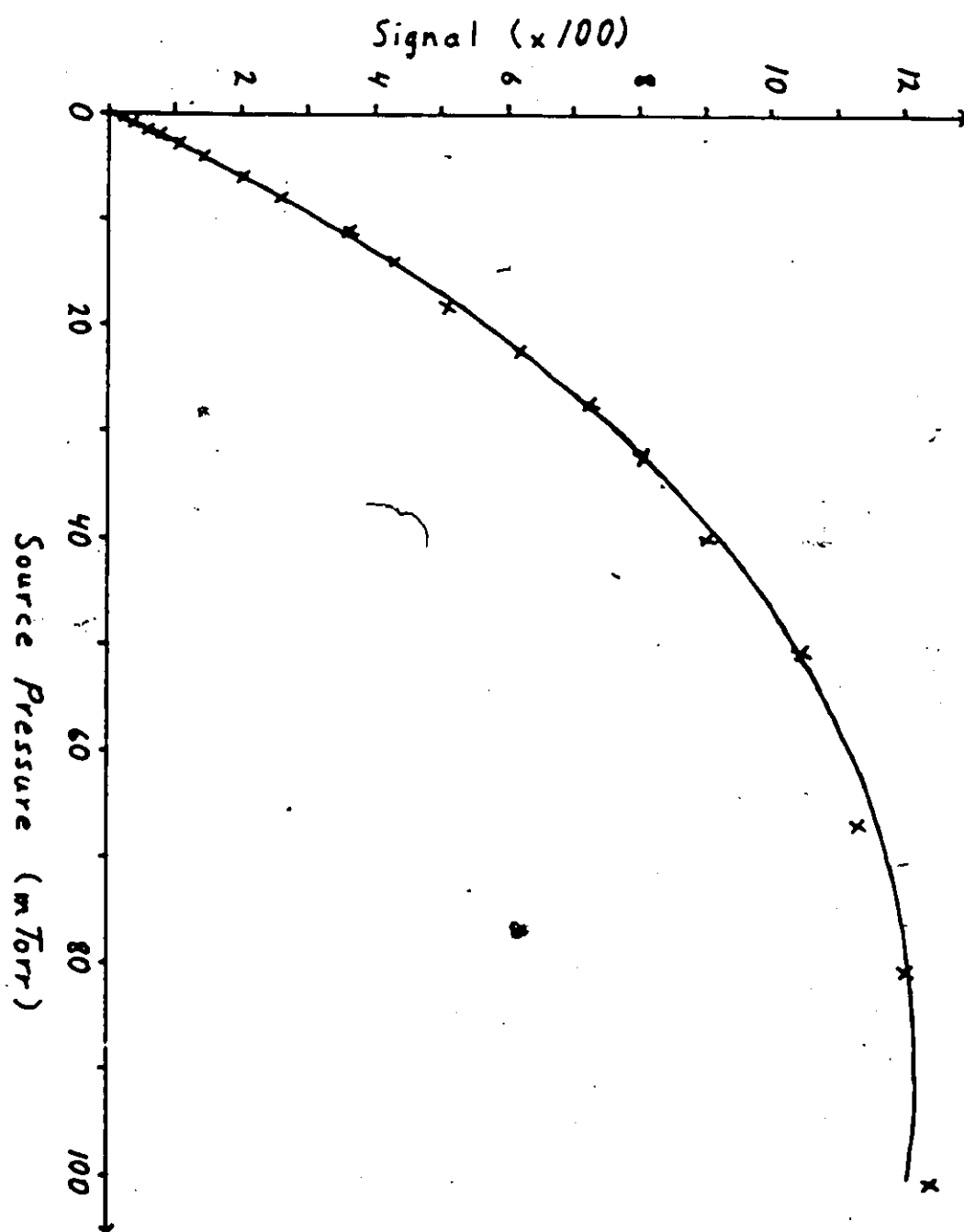
Figure 25: Intensity of the 104.8 nm emission following
200 eV electron impact on Ar versus source
pressure.
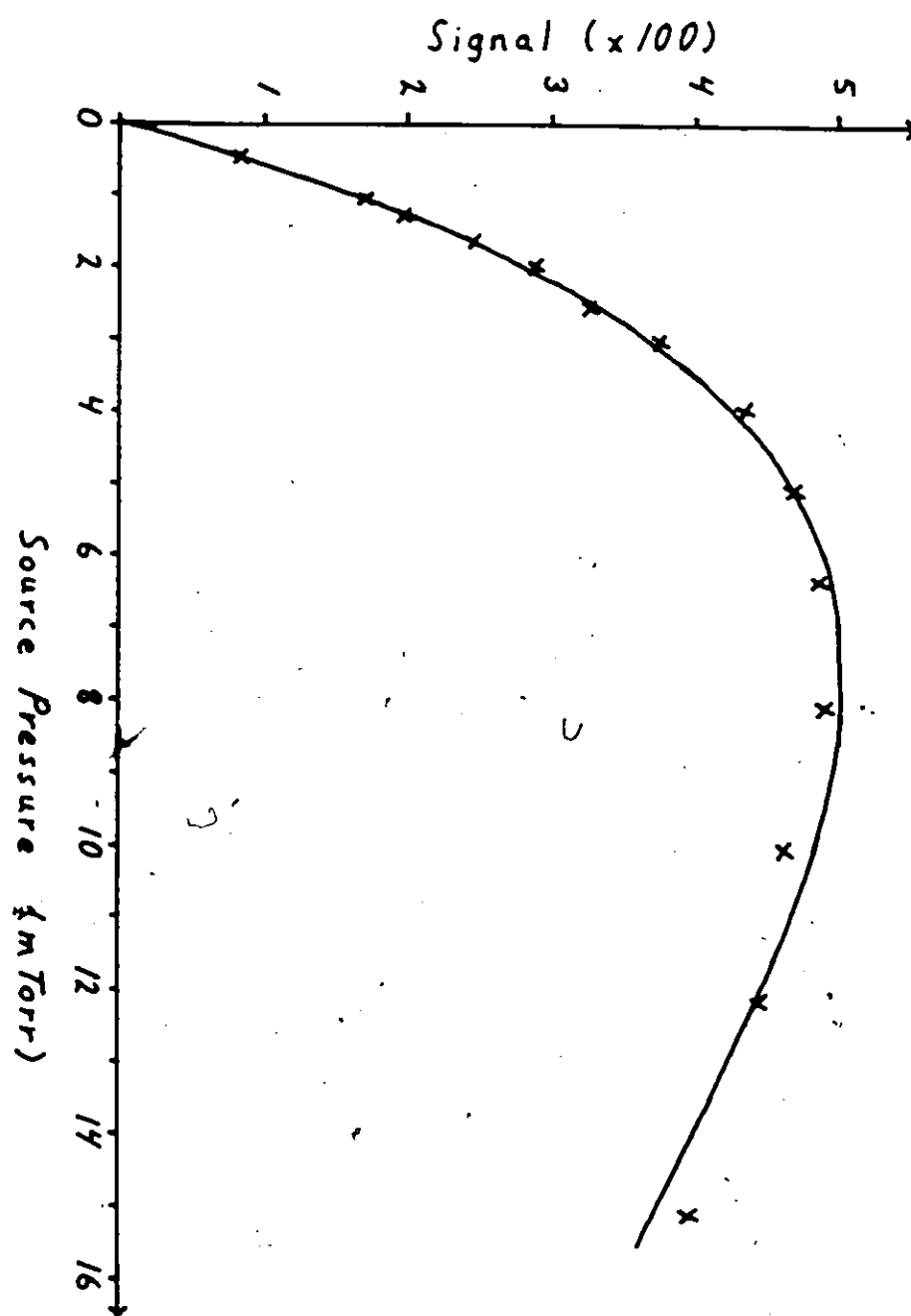
Figure 26: Intensity of the 106.7 nm emission following
200 eV electron impact on Ar versus source
pressure.

Signal (x 100)

Source Pressure (mTorr)

98
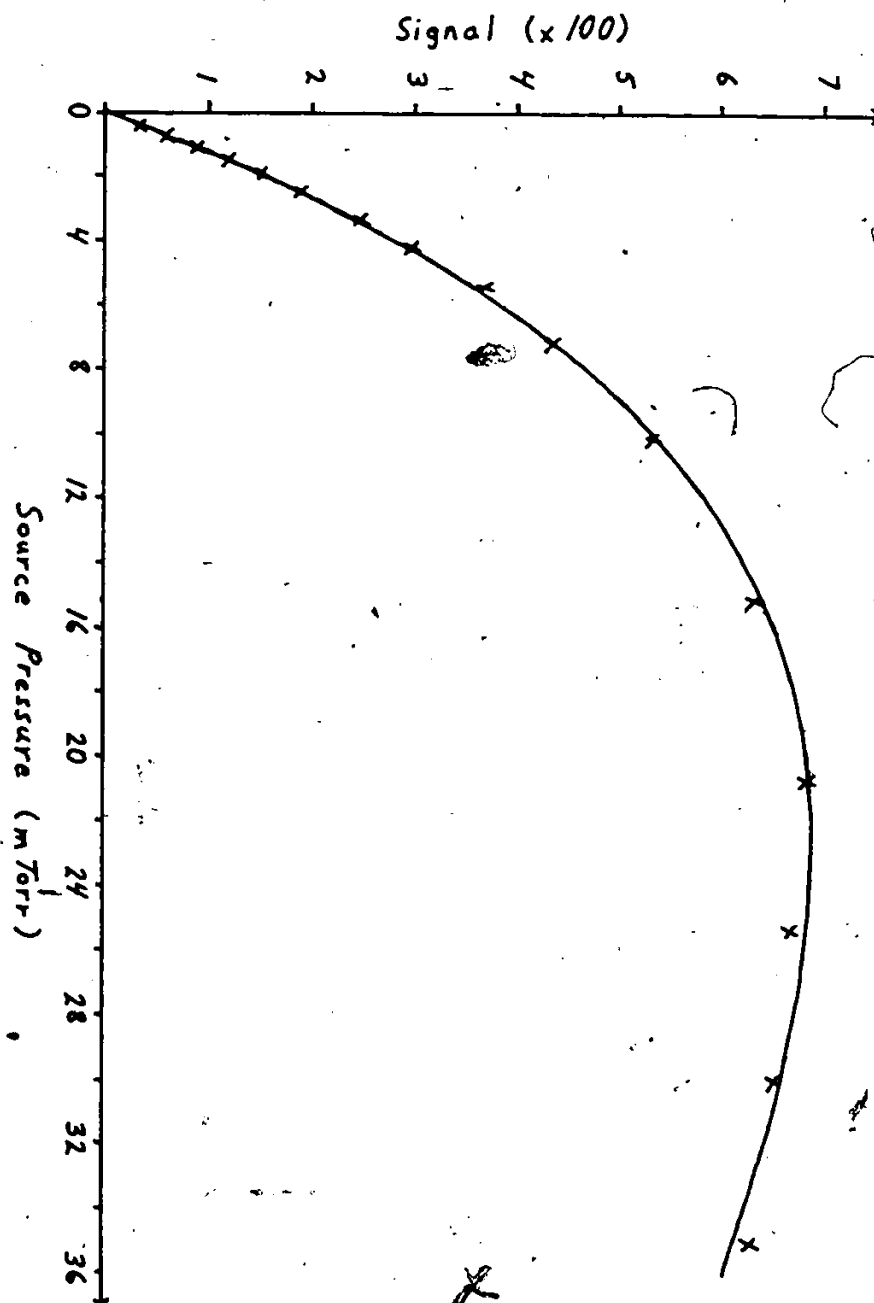
Figure 27: Intensity of the Ar^+ 92.0 nm emission (x) and
93.2 nm emission (o) following 200 eV electron
impact on Ar versus source pressure.   The
93.2 nm results have been scaled upwards by a
factor of 1.89.

Signal (x 100)

Source Pressure (mTorr)
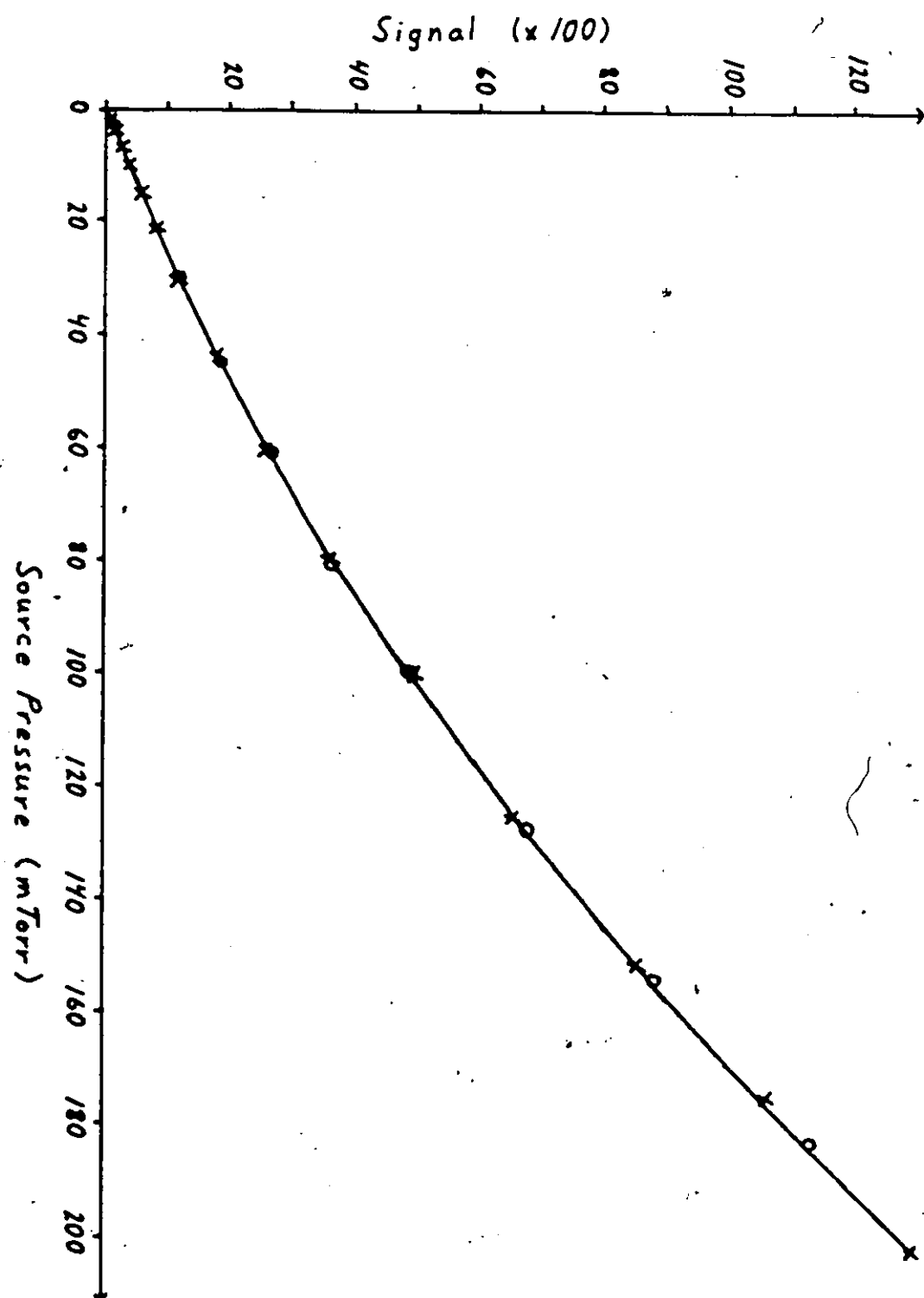
Figure 28: Intensity of the 73.6 nm emission following
200 eV electron impact on Ne versus source
pressure.

Signal (x 100)

Source Pressure (mTorr)
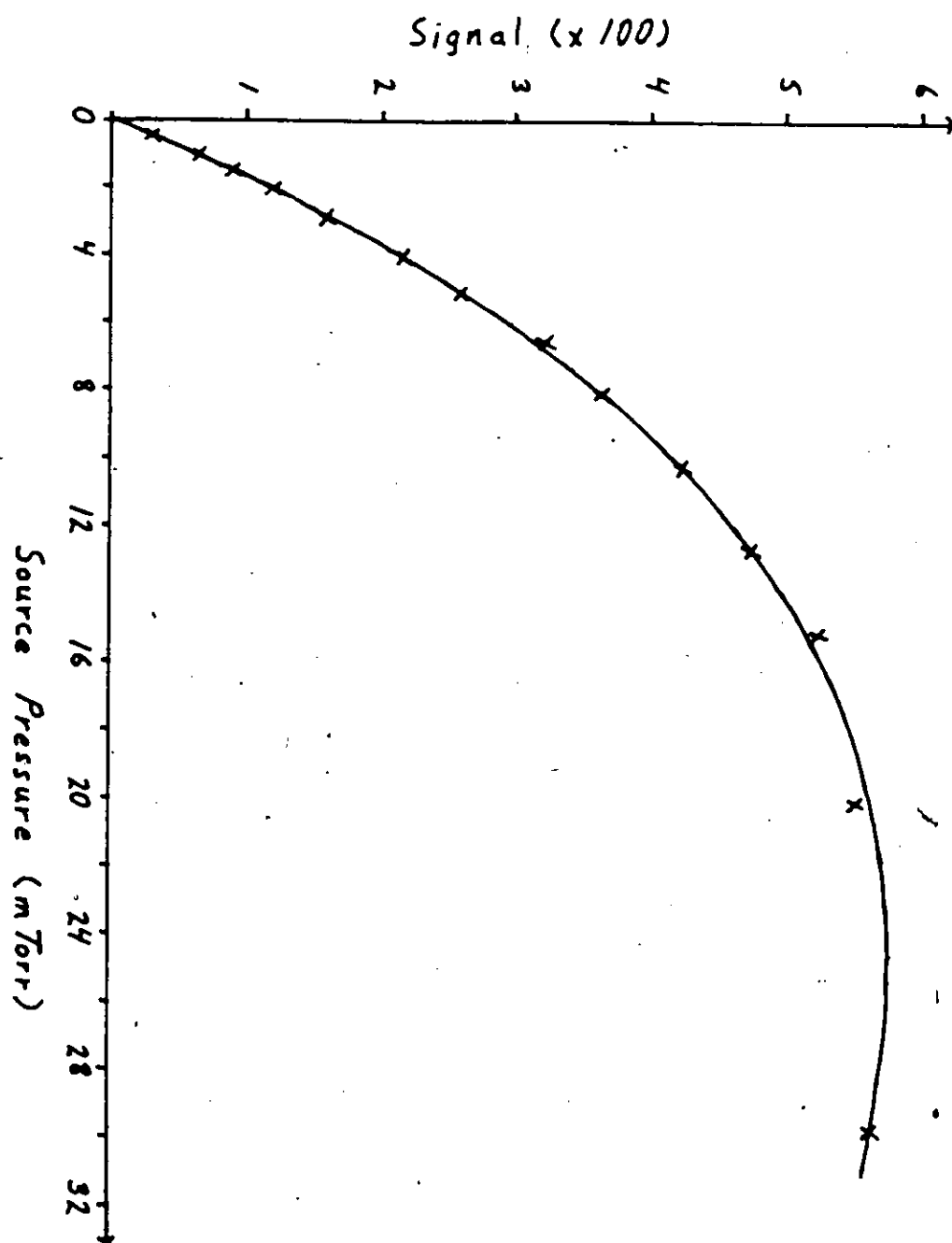
TABLE 7

Intensity versus pressure[*] fitting parameters
at 200 eV impact energy

Molecule (Line)	$S(\lambda,E)$	P_i (mTorr)	α (mTorr^{-1})
He (53.7 nm)	73.6 $\pm$ 2.1%	355.2	0.0223 $\pm$ 3.8%
He (58.4 nm)	453.9 $\pm$ 3.6%	355.2	0.0843 $\pm$ 3.6%
H_2 (Lyman α)	42.7 $\pm$ 2.6%	226.0 $\pm$ 8.4%	0
Ne (73.6 nm)	172.4 $\pm$ 2.4%	251.6	0.0923 $\pm$ 2.9%
Ar^+ (92.0 nm)	79.2 $\pm$ 2.3%	127.4 $\pm$ 3.3%	0
Ar^+ (93.2 nm)	41.9 $\pm$ 3.8%	127.4 $\pm$ 3.3%	0
Ar (104.8 nm)	375.7 $\pm$ 4.1%	127.4	0.275 $\pm$ 3.7%
Ar (106.7 nm)	129.0 $\pm$ 1.8%	127.4	0.0825 $\pm$ 3.4%
SF_6 (FI 95.6 nm)	23.75 $\pm$ 1.7%	50.76 $\pm$ 4.0%	0

[*] $S(\lambda,E,P) = S(\lambda,E)f(P/2,P_i/2)\exp[-\alpha\ f(P/2,P_i/2)]$

5.3 Mathematical Aspects

Following the same procedure as in Chapter 4 and using the results of Chapter 2, we define the signal measured at wavelength, λ, electron impact energy, E, and for a driving (head) pressure, P, to be $R(\lambda;P;E)$. Using results from Chapter 2, Appendix A, and Appendix B the measured signal can be expressed as follows.

$$R(\lambda;P;E) = \frac{Q(\lambda,E)\,Eff(\lambda)\,LIN\,D(\lambda;P;P_i)}{4\pi e\,(1 - p(\lambda;E)} \qquad (1a)$$

$$= Q'(\lambda,E)\,Eff(\lambda)\,LIN\,D(\lambda;P;P_i)/4\pi e \qquad (1b)$$

where Q is the effective cross section, Q' is the apparent cross section, $Eff(\lambda)$ is the efficiency of the detection system, L is the interaction length, I is the electron current, $p(\lambda;E)$ is the polarization, N is the target number density, and $D(\lambda;P;P_i)$ is the trapping factor.

In this experiment we wish to determine an unknown cross section, $Q'_u(E)$ at wavelength λ_u, by using a reference cross section, $Q'_r(E)$ at wavelength λ_r. Denote $R_r(E)$ to be the reference signal and $R_u(E)$ to be the "unknown" signal, for electron currents I_r, and I_u, and head pressures P_r, and P_u at the respective wavelengths. E is the energy of the electrons. Then the "unknown" apparent cross section is given by

$$Q'_u(E) = \frac{Eff(\lambda_r)\,I_r\,f(\overline{P}_r;\overline{P}_{ir})\,D(\overline{E}_r;\overline{P}_{ir})\,R_u(P)\,Q'_r(E)}{Eff(\lambda_u)\,I_u\,f(\overline{P}_u;\overline{P}_{iu})\,D(\overline{E}_u;\overline{P}_{iu})\,R_r(E)} \qquad (2)$$

where $f(\bar{P};\bar{P}_i)$ gives the form of the number density and $D(\bar{P};\bar{P}_i)$ is the trapping factor. Thus, if all the quantities on the right-hand side of equation (2) are known, one can determine the unknown apparent cross section, $Q'_u(3)$.

5.4   Results and Discussion

5.4.1   Spectra

Emission spectra covering the wavelength range from 45.0 to 185.0 nm are shown in Figure 29 and Figure 30. These spectra were obtained using the supersonic nozzle and were measured in 30.0 nm segments. Thus, these figures should only be used for spectral identification, not for calculating absolute cross sections or actual relative cross sections. Identification of the different emissions with regard to species and ionization stage is also indicated on the figures. Several interesting points may be highlighted.

All the lines observed could be identified with neutral and singly ionized sulfur and fluorine atomic transitions. The only possible exception is the 69.25 nm feature where an SIII emission may be contributing. Above 130.0 nm the spectrum is dominated by SI emissions, while below 62 nm FII lines dominate. The FI lines lie between 70 and 90.7 nm with strong additional lines at 95.6 and 97.5 nm. The SII emissions, on the other hand, are widely distributed from 60 to 136.5 nm. One may remark, that because of the richness of this spectrum, SF_6 may become a good candidate for spec-

Figure 29: Observed e^- + SF_6 emission spectrum below 130 nm.
Note tHe differert multiplying factors which
have been applied to different spectral regions.
The identification of the features is indicated.
Data were obtained using a supersonic source.
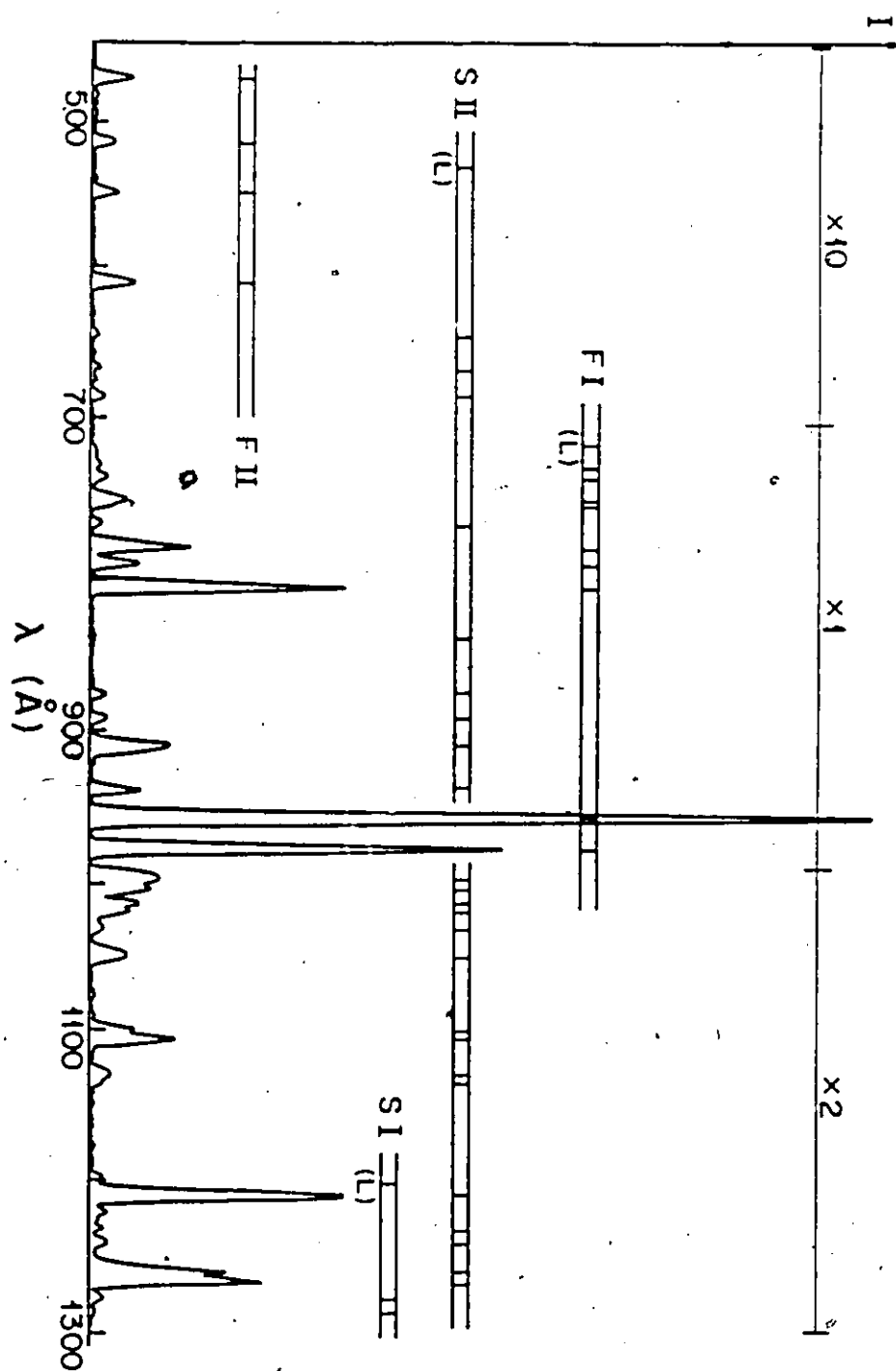
Figure 30: Observed $e^- + SF_6$ emission spectrum above 130 nm. The identification of the features is indicated. Data were obtained using a supersonic source.
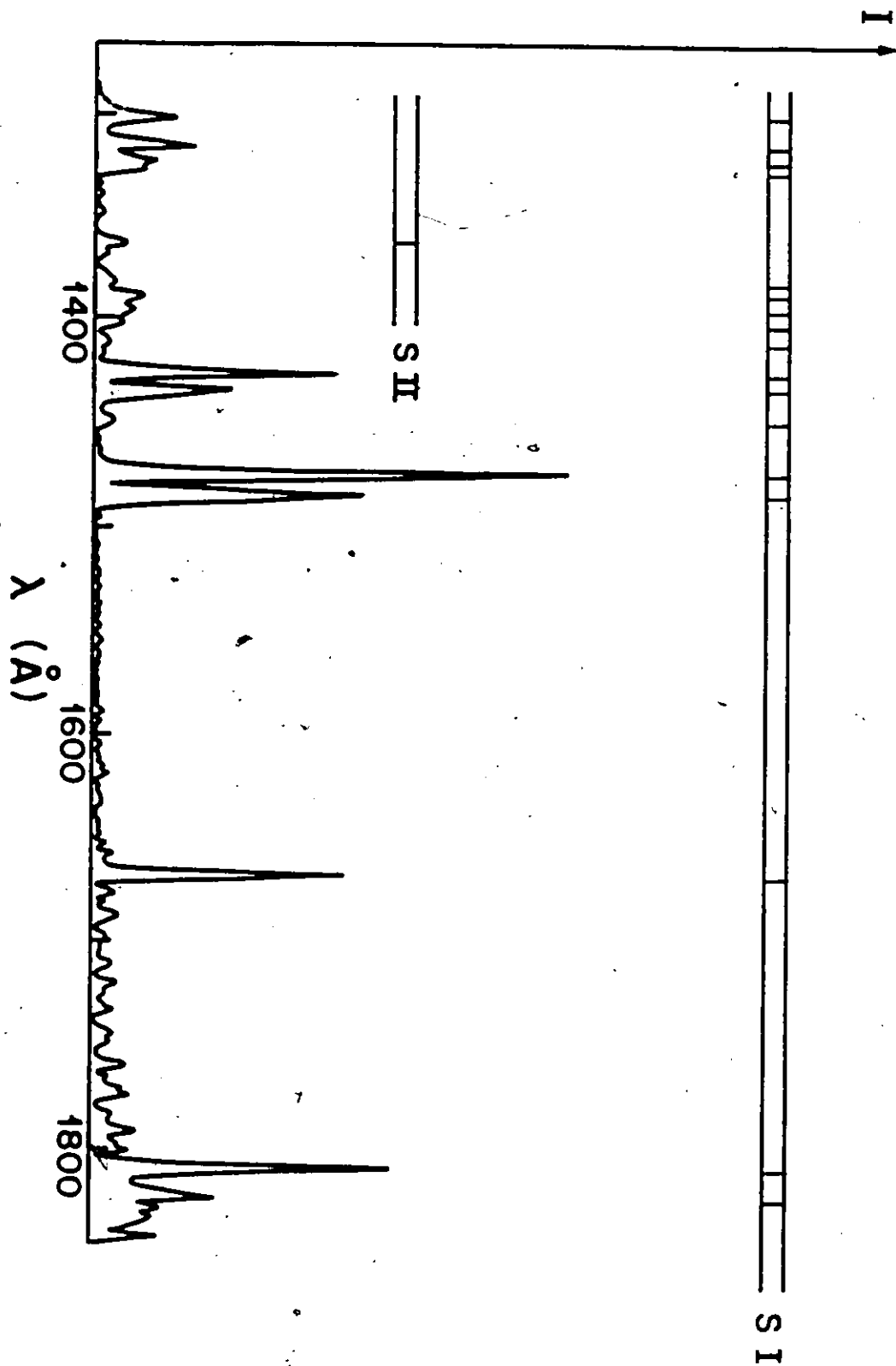
tral intensity calibration purposes in this wavelength
region.

All the major PI lines involve transitions to the ground
$1s^22s^22p^5$ $^2P_{1/2,3/2}$ state and involve the excitation of a p
electron to a 3s or 3d orbital. Excitation to orbitals with
n>3 are present but with much smaller cross sections. Fig-
ure 31 shows the energy level diagram for PI and Table 8
lists the identified transitions together with other data to
be discussed later. The multiplet nature of two strong 3s
--> 2p transitions is illustrated in the higher resolution
wavelength scan of Figure 32.

The PII spectrum consists of transitions which terminate
in the ^3P, $^1D_2$ and possibly $^1S_0$ terms of the ground configu-
ration $1s^22s^22p^4$. (See the energy level diagram in Figure
33). Again one of the outer p electrons is excited to a 3s
or 3d orbital. Exceptions to this are the strong transition
at 60.7 nm and possibly that at 51.5 nm, where an inner
shell 2s electron is excited to the 2s2p⁵ configuration
[72]. Table 9 summarizes the PII excitation data.

The SI spectrum exhibits similar features. All the lines
observed involve transitions to the ground configurations,
particularly the lowest ^2P term. (See the energy level dia-
gram in Figure 34.) The strongest features involve the pro-
motion of an outer p electron to a 4s or 3d orbital. Higher
resolution scans of the strongest features revealed the mul-
tiplet nature of the transitions. Table 10 summarizes the
SI data.

Figure 31: FI energy level diagram. Transition wavelengths
are given in Ångstroms.

$\times\,10^{3}\,cm^{-1}$

E1 Transitions

$n\ell'$ core $1s^2 2s^2 2p^4(^1D)$ $n\ell$ core $1s^2 2s^2 2p^4(^3P)$

$1s^2 2s^2 2p^5\ ^2P^{\circ}_{3/2,1/2}$

$^2P_{3/2,1/2}$ $^2D_{5/2,3/2}$ $^2F_{7/2,5/2}$ $^4P_{5/2,3/2,1/2}$ $^4D_{7/2,5/2,3/2,1/2}$ $^4F_{9/2,7/2,5/2,3/2}$

732.1 - 732.2
734.5 - 732.0
746.8 - 740.0
750.8 - 752.9
790 - 781
952 - 959

734.7 - 732.0
748.3 - 750.9
780 - 782
807 - 810

732.1 - 736.9
746.8 - 750.7
772.0 - 772.9

732.0 - 733.2
734.4 - 737.0
772.4 - 772.8
742.1 - 742.4
753.3 - 756.6
772.1 - 772.6
732.2 - 772.0
734.7 - 732.1
748.4 - 752.1
732.8 - 736.9
746.4 - 748.7
772.5 - 780.0

3s, 3d, 4s, 4d, 5s, 5p, 6s
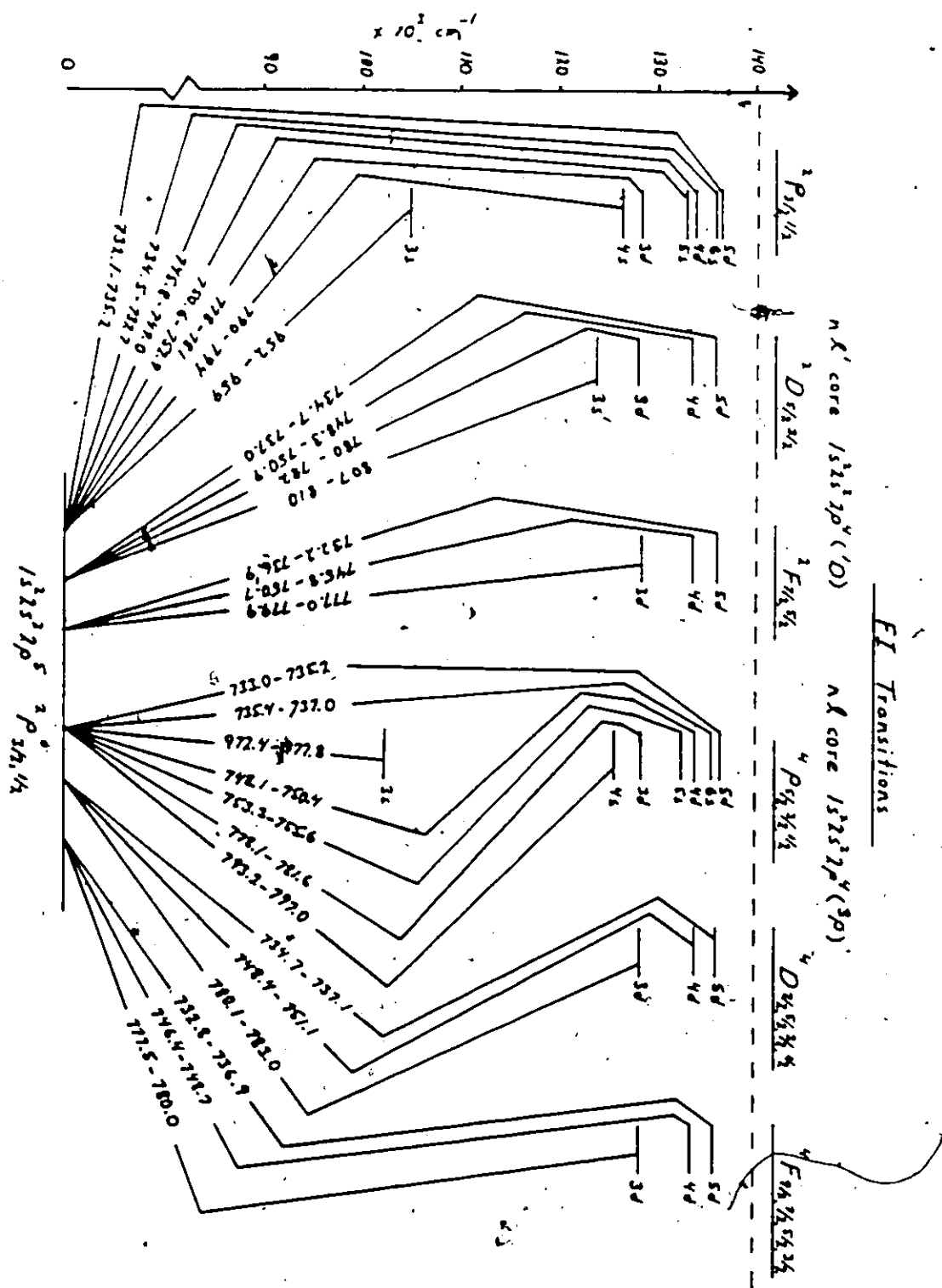
Figure 32: High resolution scans of the FI emissions near
96 nm (A) and the SII emissions near 100 nm (B).
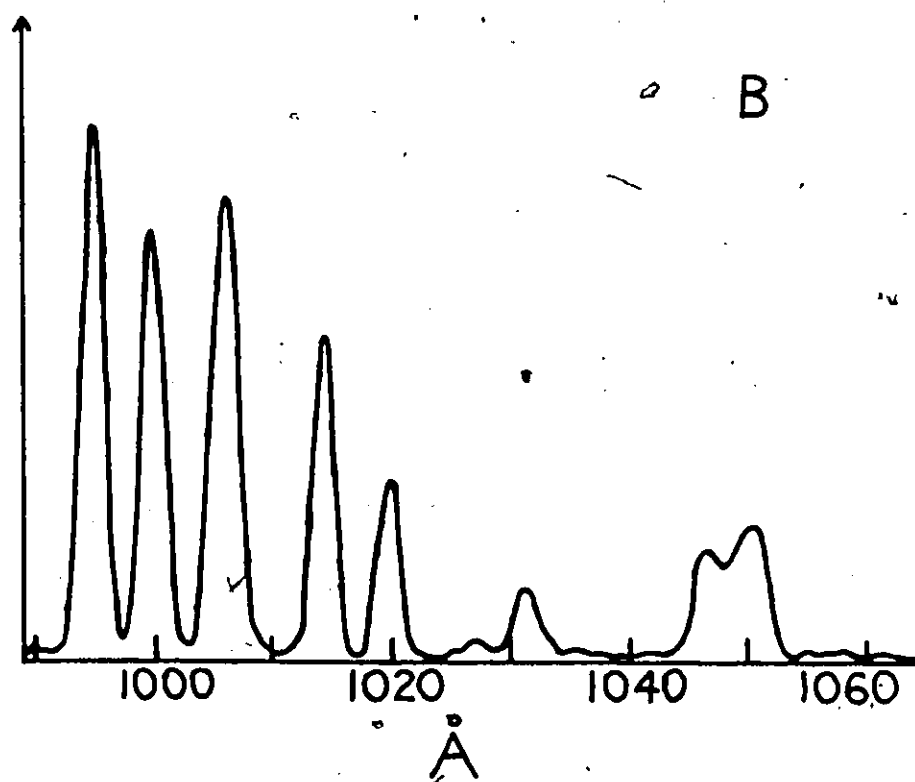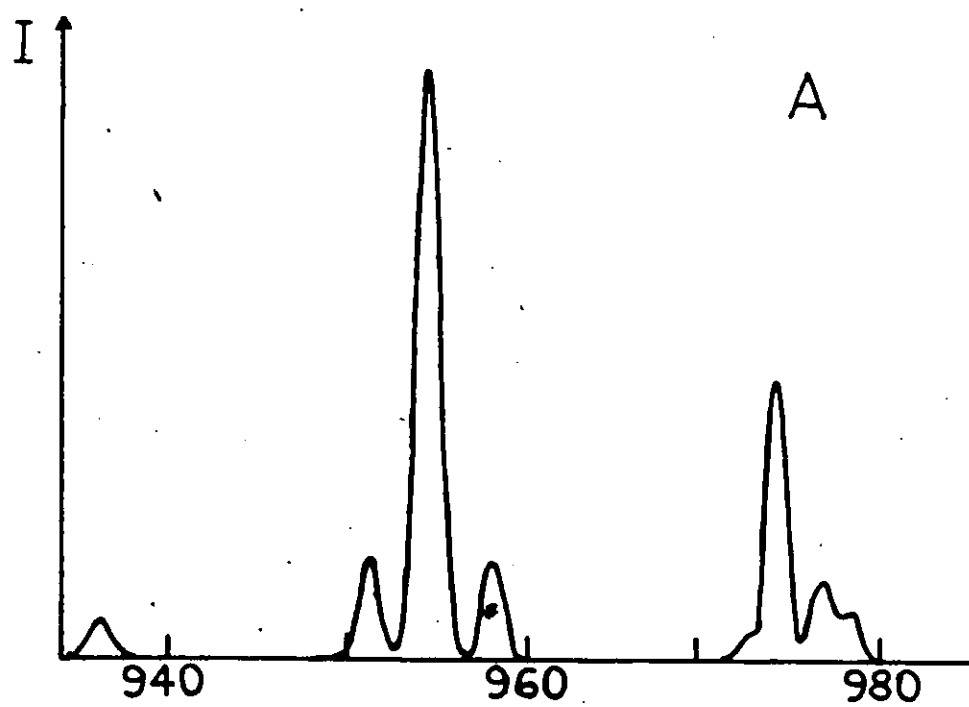
TABLE 8

Absolute FI emission cross sections
following 200 eV electron impact on SF_6

Wavelength (nm)	Transition	Cross Section ($\times 10^{-19} cm^2$)	Onset Energy (eV)
97.77	$2s^2 2p^4(^3P)3s\ ^4P_{3/2} - g^2P^0_{1/2}$	$1.59 \pm 35\%$	–
97.65	$2s^2 2p^4(^3P)3s\ ^4P_{5/2} - g^2P^0_{3/2}$	$2.94 \pm 35\%$	–
97.62	$2s^2 2p^4(^3P)3s\ ^4P_{1/2} - g^2P^0_{1/2}$		
97.39	$2s^2 2p^4(^3P)3s\ ^4P_{3/2} - g^2P^0_{3/2}$	$9.56 \pm 35\%$	–
97.24	$2s^2 2p^4(^3P)3s\ ^4P_{1/2} - g^2P^0_{3/2}$	$0.53 \pm 35\%$	–
95.85	$2s^2 2p^4(^3P)3s\ ^2P_{3/2} - g^2P^0_{1/2}$	$2.32 \pm 35\%$	
95.55	$2s^2 2p^4(^3P)3s\ ^2P_{1/2} - g^2P^0_{1/2}$	$15.80 \pm 35\%$	35.8 ± 1.5
95.48	$2s^2 2p^4(^3P)3s\ ^2P_{3/2} - g^2P^0_{3/2}$		41.2 ± 1.5
95.19	$2s^2 2p^4(^3P)3s\ ^2P_{1/2} - g^2P^0_{3/2}$	$2.22 \pm 35\%$	
80.96	$2s^2 2p^4(^1D)3s\ ^2D_{3/2} - g^2P^0_{1/2}$	$1.86 \pm 40\%$	35.7 ± 1.5
80.70	$2s^2 2p^4(^1D)3s\ ^2D_{5/2} - g^2P^0_{3/2}$	$3.42 \pm 40\%$	42.7 ± 1.5
79.20	$2s^2 2p^4(^3P)4s\ ^2P - g^2P^0$	$1.29 \pm 40\%$	–
79.45	$2s^2 2p^4(^3P)4s\ ^4P - g^2P^0$	$0.68 \pm 40\%$	–
78.0	$2s^2 2p^4(^3P)3d\ ^{2,4}P, ^{2,4}D, ^{2,4}F - g^2P^0$	$3.72 \pm 40\%$	–
75.1	$2s^2 2p^4(^3P)4d\ ^{2,4}P, ^{2,4}D, ^{2,4}F - g^2P^0$	$1.66 \pm 40\%$	–
	$2s^2 2p^4(^3P)5s\ ^{2,4}P - g^2P^0$		
71.1-73.6	Higher excited states $- g^2P^0$	$1.49 \pm 45\%$	–

Figure 33: FII energy level diagram. Transition wavelengths
are given in Ångstroms.
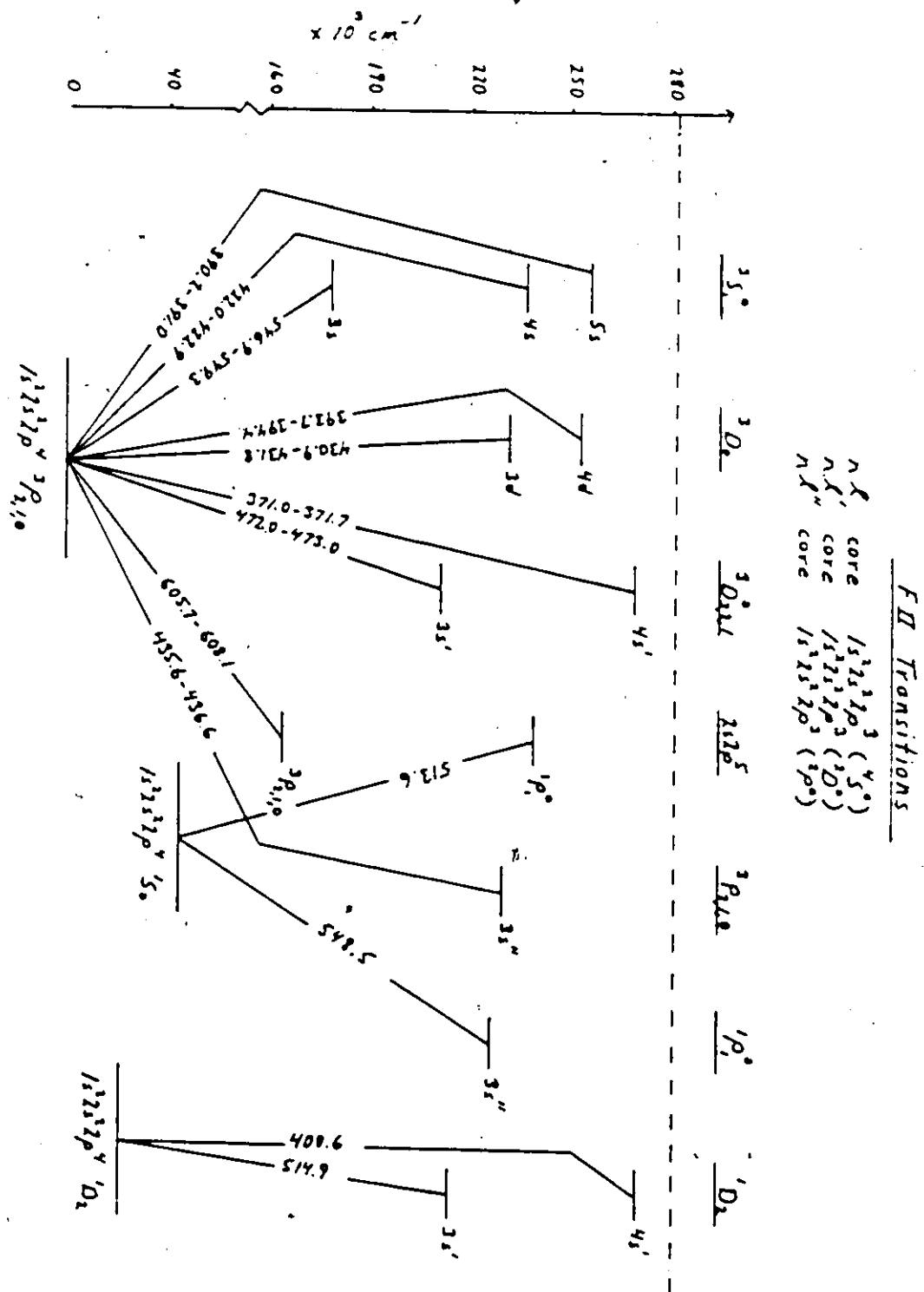
F II Transitions

TABLE 9

Absolute FII emission cross sections following 400 eV electron impact on SF_6

Wavelength (nm)	Transition	Cross Section ($\times 10^{-20} cm^2$)	Onset Energy (eV)
60.7	$2s2p^5\ ^3P_{2,1,0} - g\ ^3P^0_{2,1,0}$	$1.85 \pm 25\%$	43.5 ± 1.5 59.3 ± 1.5
54.8	$2s^22p^3(^4S^0)3s\ ^3S^0_1 - g\ ^3P^0_{2,1,0}$ $2s^22p^3(^2P^0)3s\ ^1P^0_1 - 2s^22p^4\ ^1S^0$	$1.29 \pm 30\%$	–
51.5	$2s2p^5\ ^1P^0_1 - 2s^22p^4\ ^1S_0$ $2s^22p^3(^2D^0)3s\ ^1D_2 - 2s^22p^4\ ^1D_2$	$0.88 \pm 40\%^*$	–
47.3	$2s^22p^2(^2D^0)3s\ ^3D^0_{3,2,1} - g\ ^3P^0_{2,1,0}$	$2.18 \pm 60\%^*$	–

* Error is larger for this line due to our extrapolation of the detector efficiency to these wavelengths.

Figure 34: SI energy level diagram.   Transition wavelengths
are given in Ångstroms.
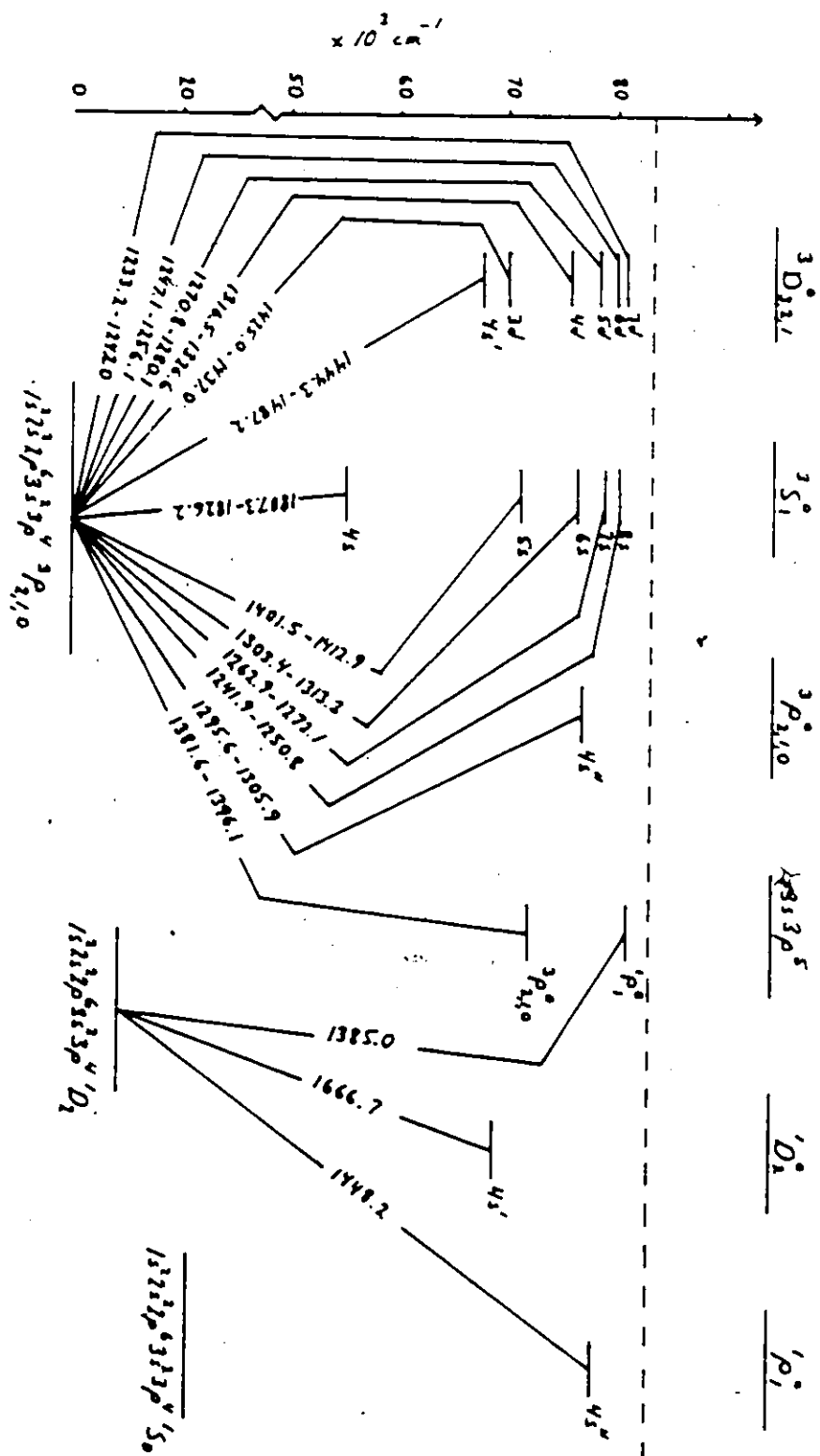
TABLE 10

Absolute SI emission cross sections following 200 eV electron impact on SF_6

Wavelength (nm)	Transition	Cross Section ($\times 10^{-19} cm^2$)	Onset Energy (eV)
129.6–130.6	$3s^2 3p^3(^2P^0)4s\ ^3P^0 - g\ ^3P$ $3s^2 3p^3(^4S^0)6s\ ^3S^0 - g\ ^3P$	$0.31 \pm 25\%$	–
131.0–131.7	$3s^2 3p^3(^4S^0)6s\ ^3S^0 - g\ ^3P$ $3s^2 3p^3(^4S^0)4d\ ^3D^0 - g\ ^3P$	$0.38 \pm 25\%$	–
132.4–132.7	$3s^2 3p^3(^4S^0)4d\ ^3D^0 - g\ ^3P$	$0.27 \pm 25\%$	
138.1–139.7	$3s 3p^5\ ^3P^0 - g\ ^3P$	$0.57 \pm 20\%$	–
142.5	$3s^2 3p^3(^4S^0)3d\ ^3D^0_{3,2,1} - g\ ^3P_2$	$0.80 \pm 15\%$	38.0 ± 1.5 43.3 ± 1.5
143.3	$3s^2 3p^3(^4S^0)3d\ ^3D^0_{2,1} - g\ ^3P_1$	$0.38 \pm 20\%$	–
143.7	$3s^2 3p^3(^4S^0)3d\ ^3D^0_1 - g\ ^3P_0$	$0.16 \pm 25\%$	–
147.4	$3s^2 3p^3(^2D^0)4s\ ^3D^0_{3,2,1} - g\ ^3P_2$	$1.65 \pm 15\%$	36.8 ± 1.5 43.3 ± 1.5
148.3	$3s^2 3p^3(^2D^0)4s\ ^3D^0_{2,1} - g\ ^3P_1$	$0.83 \pm 20\%$	–
148.7	$3s^2 3p^3(^2D^0)4s\ ^3D^0_1 - g\ ^3P_0$	$0.24 \pm 25\%$	–
166.7	$3s^2 3p^3(^2D^0)4s\ ^1D^0_2 - 3s^2 3p^4\ ^1D_2$	$0.81 \pm 20\%$	–
180.7	$3s^2 3p^3(^4S^0)4s\ ^3S^0_1 - g\ ^3P_2$	$0.87 \pm 25\%$[*]	–
182.3	$3s^2 3p^3(^4S^0)4s\ ^3S^0_1 - g\ ^3P_{1,0}$	$0.58 \pm 35\%$[*]	–

[*] Error is larger for this line due to our extrapolation of the detector efficiency to these wavelengths.

Many rather weak SII lines were observed from 60 to 136.5
nm (see Figure 29 and Figure 30). Again a pattern emerged
similar to the other atomic systems. Transitions were
observed involving all three ^2P, ^2D and ^4S terms cf the
ground $3s^23p^3$ configuration. (See the energy level diagrams
in Figure 35 and Figure 36.) Promotion of an outer p elec-
tron, predominantly to a 4s or 3d orbital, was found and
both doublet and quartet systems were evident. Inner shell
excitation (to the $3s3p^4$ configuration) gives rise to the
features near 105 nm, 120.4 nm, 136.2 nm, and 125.5 nm [74].
Full details of the SII data are summarized in Table 11.
The multiplet nature can be seen in Figure 32.

Only a single indication was found that a higher ioniza-
tion stage might be present. The weak feature near 68.5 nm
could have a SIII contribution. It is interesting to note
that clear evidence for this feature was observed in the
electron impact dissociation of SO_2 (Becker et al [12]).

Figure 35: SII doublet system energy level diagram.
Transition wavelengths are given in Ångstroms.

$\times 10^3 \ cm^{-1}$

0
20
70
100
130
160
190

$^2F_{7/2,5/2}$

$^2D_{3/2,5/2}$

$^2P_{1/2,3/2}$

$^2S_{1/2}$

$3s^23p^3 \ ^4S_{3/2}$

$3s^23p^3 \ ^2D_{3/2,5/2}$

$3s^23p^3 \ ^2P_{1/2,3/2}$

SⅡ - Transitions

$n'f'$ core $3s^23p^2 \ (^3P)$
$n'f'$ core $3s^23p^2 \ (^1D)$
$n''f''$ core $3s^23p^2 \ (^1S)$

649.8 - 655.9
705.2 - 702.0
679.9 - 1000.8
649.5 - 655.0
683.9 - 689.0
689.4 - 695.6
699.6 - 844.1
937.4 - 937.7
1031.8 - 9169.0
740.9 - 741.2
729.8 - 728.1
688.0 - 693.3
659.8 - 655.3
733.6 - 732.6
763.2 - 756.9
10141 - 10109
1026.6 - 11024
1126.7 - 1136.1
1124.4 - 1131.7
785.0 - 786.6
702.6 - 705.4
864.3 - 844.8

Figure 36: SII, quartet system, energy level diagram.
Transition wavelengths are given in Ångstroms.

$\times \, 10^3 \, cm^{-1}$
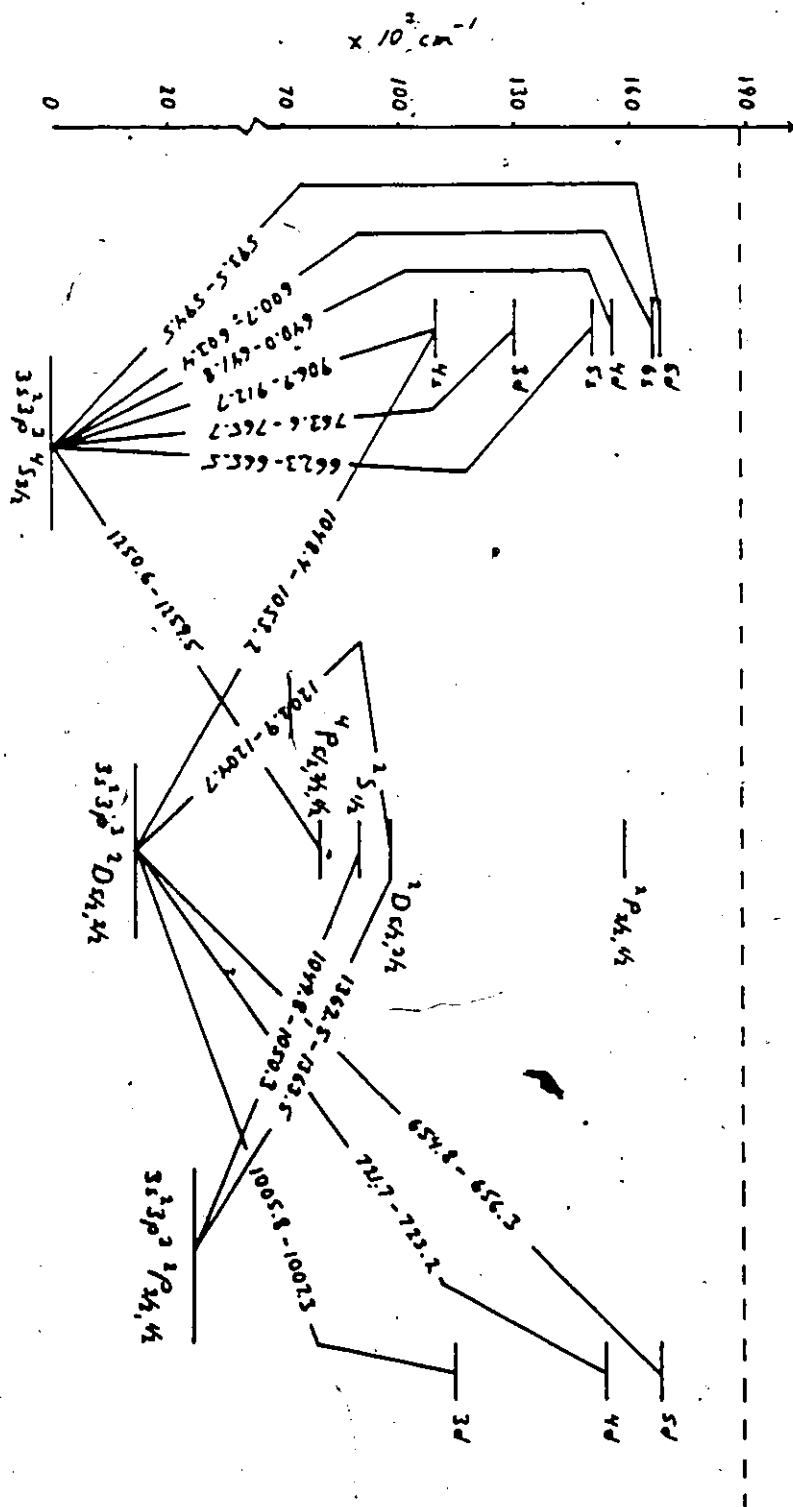
SⅡ Transitions.

| $n\ell$ | core | $3s^2 3p^2$ | (^3P) |
| $n\ell'$ | core | $3s^2 3p^2$ | (^1D) |
| $n\ell''$ | core | $3s^2 3p^2$ | (^1S) |

TABLE 1F

Absolute SII emission cross sections
following 200 eV electron impact on SF_6

Wavelength (nm)	Transition	Cross Section ($\times 10^{-19} cm^2$)	Onset Energy (eV)
90.69	$3s^2 3p^2 (^3P)4s\ ^4P_{5/2} - g^4S_{3/2}$	$1.03 \pm 40\%$	
91.05	$3s^2 3p^2 (^3P)4s\ ^4P_{3/2} - g^4S_{3/2}$	$0.59 \pm 40\%$	47.4 ± 1.5
91.27	$3s^2 3p^2 (^3P)4s\ ^4P_{1/2} - g^4S_{3/2}$	$0.34 \pm 40\%$	54.5 ± 1.5
91.54	$3s^2 3p^2 (^3P)3d\ ^2D_{5/2} - ^2P_{3/2}$	$0.06 \pm 40\%$	
91.90	$3s^2 3p^2 (^3P)3d\ ^2D_{3/2} - ^2P_{1/2,3/2}$	$0.05 \pm 40\%$	
93.7	$3s^2 3p^2 (^1D)4s\ ^2D_{3/2} - 3s^2 3p^3\ ^2D_{3/2}$ $3s^2 3p^2 (^1D)4s\ ^2D_{5/2} - 3s^2 3p^3\ ^2D_{5/2}$	$0.71 \pm 40\%$	−
99.60	$3s^2 3p^2 (^3P)3d\ ^2F_{7/2} - ^2D_{5/2}$	$0.92 \pm 40\%$	
100.06	$3s^2 3p^2 (^3P)3d\ ^2F_{5/2} - ^2D_{3/2,5/2}$	$0.71 \pm 40\%$	47.7 ± 1.5
100.61	$3s^2 3p^2 (^3P)3d\ ^4D_{7/2} - ^2D_{5/2}$	$0.87 \pm 40\%$	56.4 ± 1.5
100.63	$3s^2 3p^2 (^3P)3d\ ^4D_{5/2} - ^2D_{3/2}$		
101.42	$3s^2 3p^2 (^3P)4s\ ^2P_{3/2} - ^2D_{5/2,3/2}$	$0.51 \pm 40\%$	
101.95	$3s^2 3p^2 (^3P)4s\ ^2P_{1/2} - ^2D_{3/2}$	$0.31 \pm 40\%$	−
103.09	$3s^2 3p^2 (^1D)4s\ ^2D_{3/2} - ^2P_{1/2}$	$0.13 \pm 40\%$	−
103.04	$3s^2 3p^2 (^1D)4s\ ^2D_{5/2} - ^2P_{3/2}$		
104.5-105.3	$3s^2 3p^2 (^3P)3d\ ^4F - 3s^2 3p^3\ ^2D$ $3s^2 3p^2 (^3P)4s\ ^4P - 3s^2 3p^3\ ^2D$ $3s3p^4\ ^2S_{1/2} - 3s^2 3p^3\ ^2P_{3/2,1/2}$	$0.66 \pm 40\%$	
110.0	$3s^2 3p^2 (^3P)3d\ ^2P - 3s^2 3p^3\ ^2D$	$1.47 \pm 25\%$	−
112.4-113.2	$3s^2 3p^2 (^3P)4s\ ^2P - 3s^2 3p^3\ ^2D$	$0.39 \pm 40\%$	−
120.4	$3s3p^4\ ^2D - 3s^2 3p^3\ ^2D$	$3.18 \pm 13\%$	45.5 ± 1.5 51.0 ± 1.5
125.0-126.0	$3s3p^4\ ^4P - g^4S_{3/2}$	$3.21 \pm 18\%$	−

5.4.2   Excitation Functions and Absolute Cross Sections

5.4.2.1   Fluorine Emissions

Excitation functions from threshold up to 600 eV have been measured for the six strongest FI emissions. The shapes of all curves are similar above 50 eV. Typical FI excitation functions are displayed in Figure 37 together with the excitation function of the FII 60.7 nm line. The various excitation functions in Figure 37 and Figure 38 have been arbitrarily displaced vertically for clarity of presentation. Their respective magnitudes do not reflect the ratio of the absolute emisssion cross sections. The FI excitation functions all display a smooth increase to a maximum slightly above 200 eV and a gradual decline towards higher impact energies. This indicates that optically allowed excitation routes in the parent SF_6 molecule dominate the formation of excited FI fragments. The absolute emission cross sections of the FI lines at 200 eV impact energy are given in Table 8. Low resolution spectra (FWHM = 0.51 nm) were used in the normalization procedure to obtain high statistical accuracy. Cross sections for the individual components of the emission features centred at 97.5 nm, 95.5 nm, and 80.7 nm, respectively, were obtained from high resolution spectra. The other FI features are too complex and weak to easily isolate their individual components. Errors on the cross sections are typically 35% and are due almost entirely to uncertainties in the reference cross sections. This is true of all the cross sections.

Figure 37: FI and FII excitation functions: ● , FI 97.5 nm;
o , FI 95.5 nm; □ , FI 80.7 nm; and ■ , FII
60.7 nm. Note that the cross section scale is
arbitrary (see text).
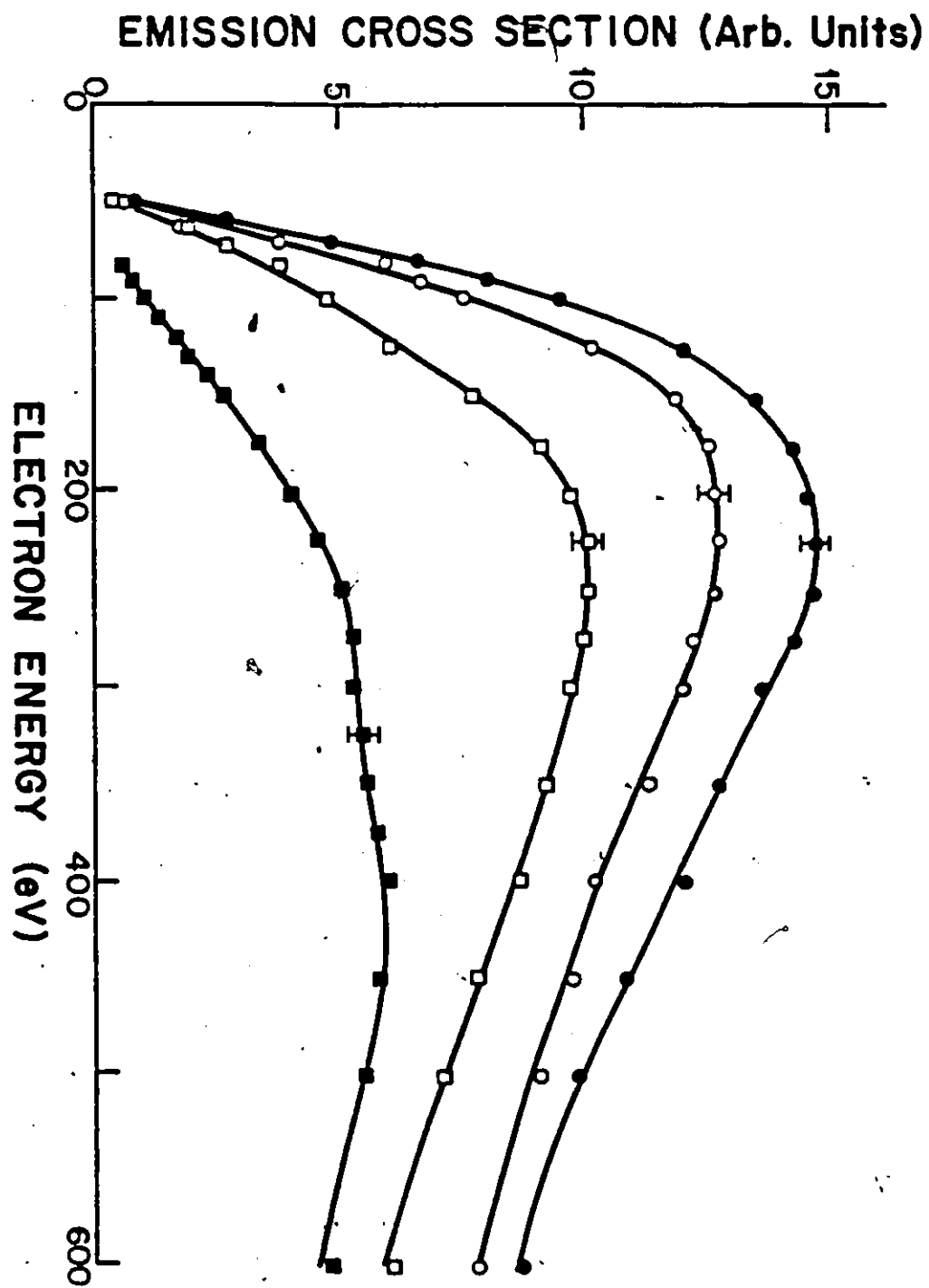
Emissions from singly ionized fluorine were found to be extremely weak. Several cross sections are given in Table 9. Errors on these cross sections are typically 30%. Only the 60.7 nm feature with an absolute emission cross section of 10^{-20} cm^2 at 200 eV was intense enough to be studied in some detail. The excitation function of this line is also displayed in Figure 37. Several independent measurements were taken and all showed a distinct indication of a broad double-peak structure. Unfortunately, no other FII line was intense enough to measure an excitation function with sufficient statistical accuracy to establish this behavior as being a characteristic feature of FII emissions. None of the FI lines or the SI and SII emissions displayed a similar structure in the excitation function.

5.4.2.2 Sulphur Emissions

The neutral sulphur emissions, which dominate the emission spectrum above 130 nm (Figure 30), are also character- ized by excitation functions typical of underlying optically allowed excitations in the parent molecule (see Figure 39). The absolute emission cross sections for these lines and the corresponding electronic transitions are summarized in Table 10. Errors of 20% are typical. Emissions from singly ion- ized sulphur are abundant from 60 to 136.5 nm (Figure 29 and Figure 30). Excitation functions were measured for the stronger transitions and are displayed in Figure 38. Again, all underlying processes appear to be optically allowed in

nature, as can be seen from the shapes of typical SII excitation functions. Absolute emission cross sections for the various SII features are given in Table 11. Errors are typically 35%. High resolution scans of the SII emissions at 91 nm and of the very complex feature between 99.6 and 102.0 nm (Figure 32) allowed individual cross sections to be presented for the transitions listed in Table 11.

Figure 38: SI and SII excitation functions: ● , SI 147.1-
148.7 nm; o , SI 166.7 nm; □ , SII 100 nm;
and ■ , SII 120.4 nm. Note that the cross
section scale is arbitrary (see text).

EMISSION CROSS SECTION (Arb. Units)
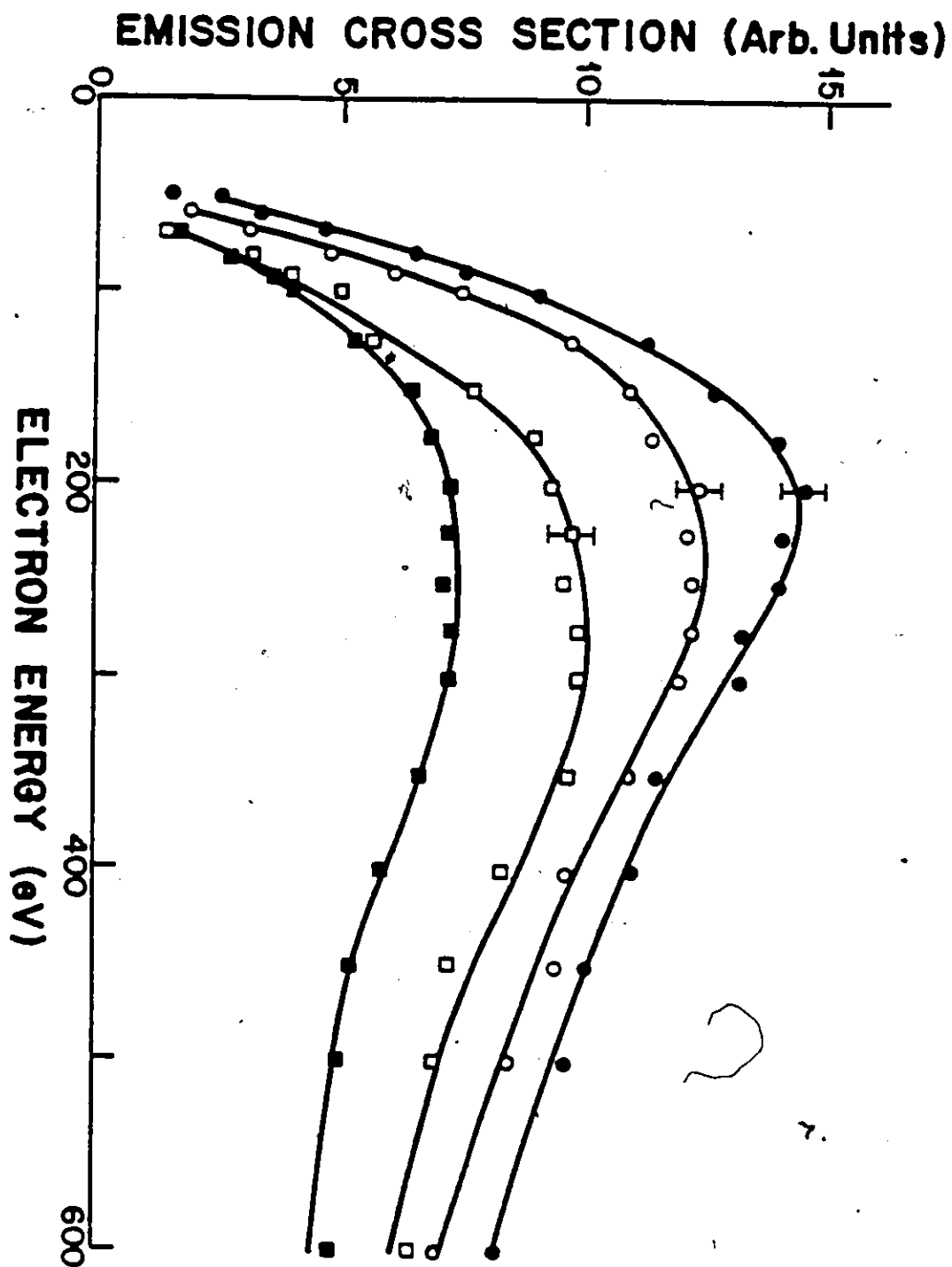
ELECTRON ENERGY (eV)

5.4.3   Onsets

Onset potentials for a number of lines were obtained by scanning the incident electron energy over the near-threshold region. The data were normalized with respect to changes in electron current with incident electron energy. Figure 39 through Figure 46 show near-threshold excitation functions for some of the stronger lines corresponding to PI, PII, SI, and SII transitions. Adjacent channels of the multichannel output were added until the distance between points in the display was approximately equal to the energy resolution of the electron beam. This improved the statistical significance of the individual points. The two thresholds evident in all the threshold excitation functions appear to be a general feature. The positions of these onsets are included in Table 8 to Table 11 where appropriate. Clearly, many different channels play a prominent role in the dissociation of SF_6. Recent time of flight studies in this laboratory, Corr et al [20], of the dissociative excitation of SF_6, in which both visible and long-lived Rydberg species were detected, have revealed the onset of dissociative channels at very similar energies as those observed in the present work.

We consider first the SI and SII lines, which, of necessity, must arise from total fragmentation of the molecule. After allowing for excitation (and ionization) energies, we note that the residual energy that must account for fragmen-
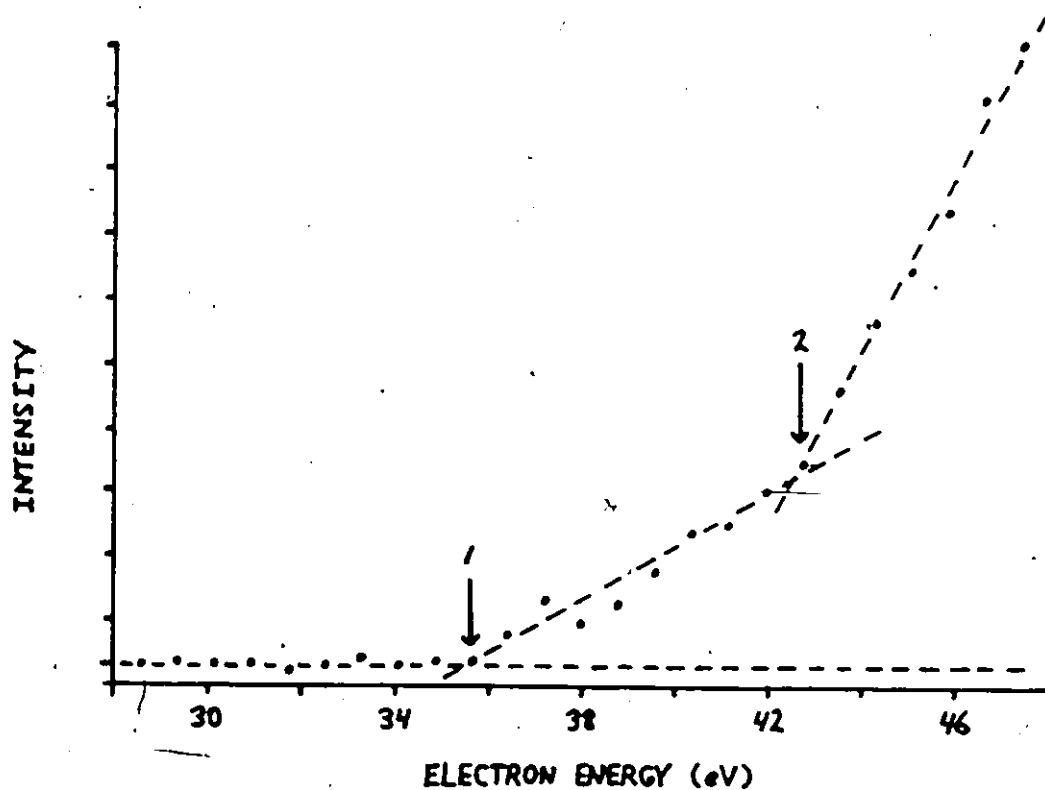
Figure 39: Near-threshold excitation function of
the FI emission at 80.7 nm. Note the
two onsets indicated by 1 and 2.
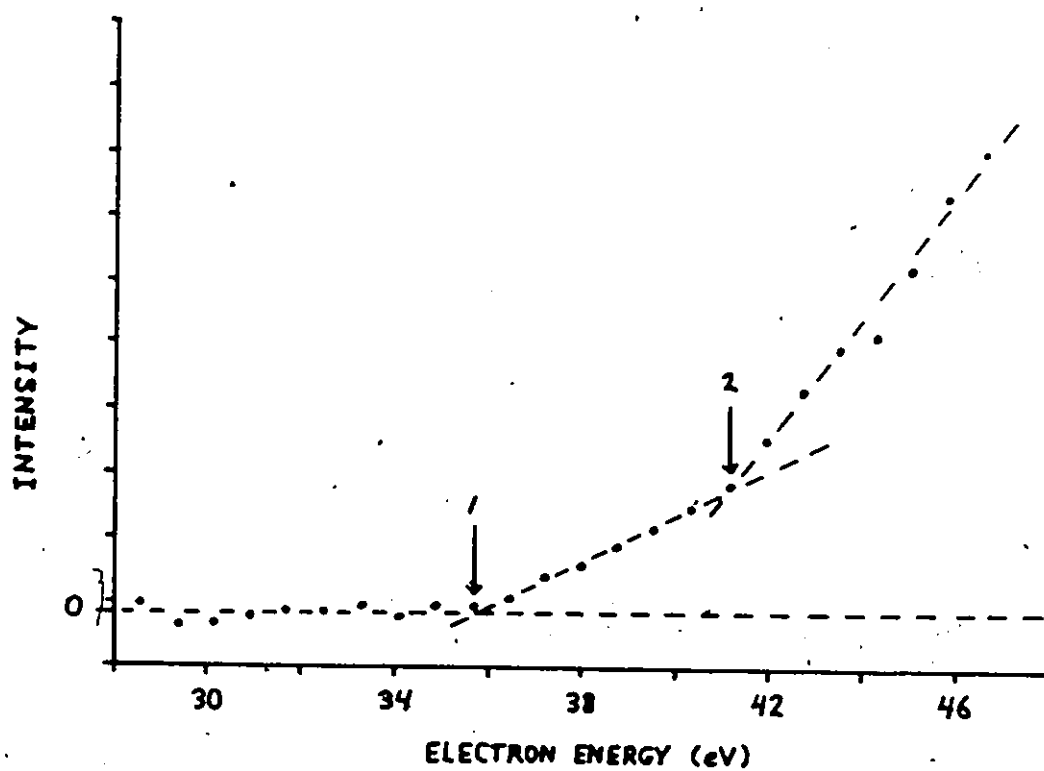
Figure 40: Near-threshold excitation function of the FI emission at 95.7 nm. Note the two onsets indicated by 1 and 2.

FII 60.6 nm
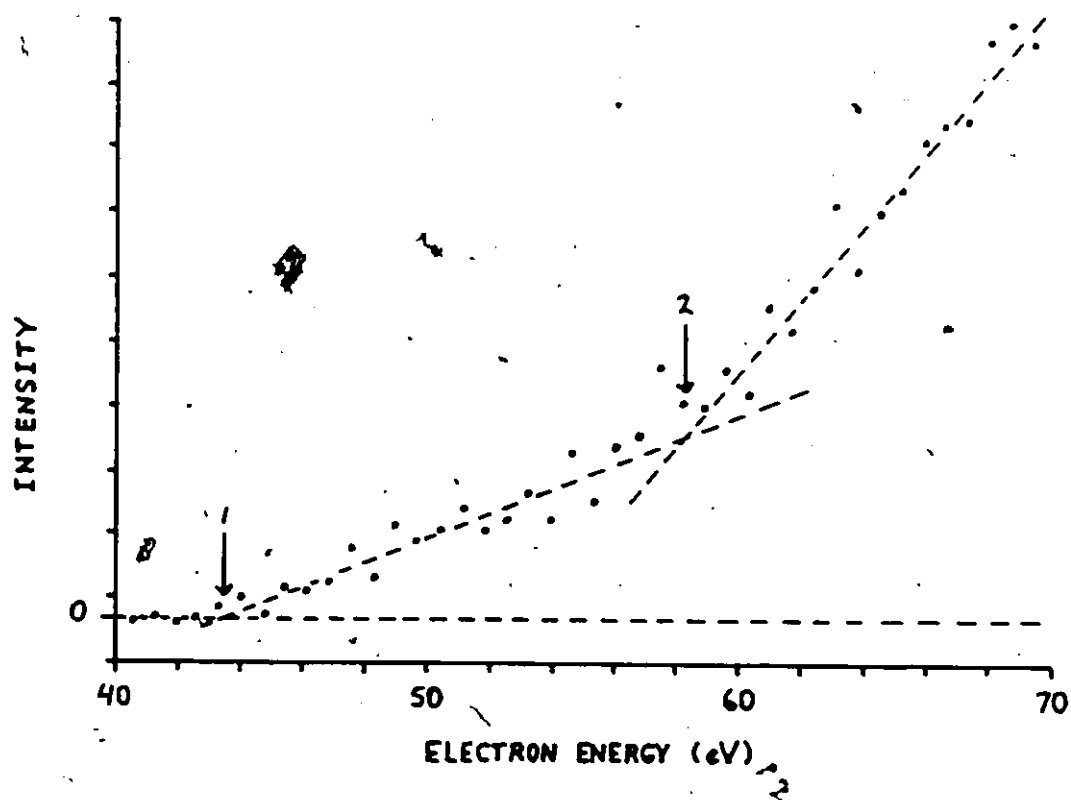
Figure 41: Near-threshold excitation function of the FII emission at 60.7 nm. Note the two onsets indicated by 1 and 2.
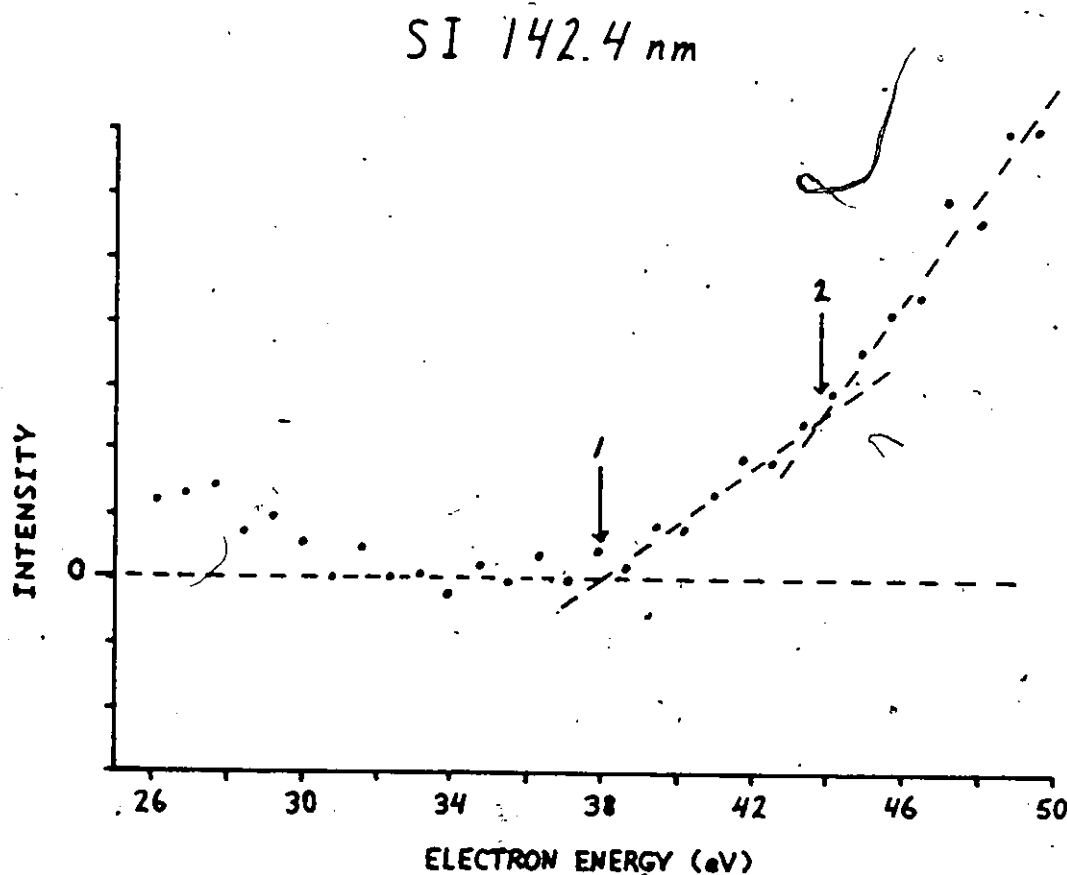
Figure 42: Near-threshold excitation function of
the SI emission at 142.4 nm. Note the
two onsets indicated by 1 and 2.
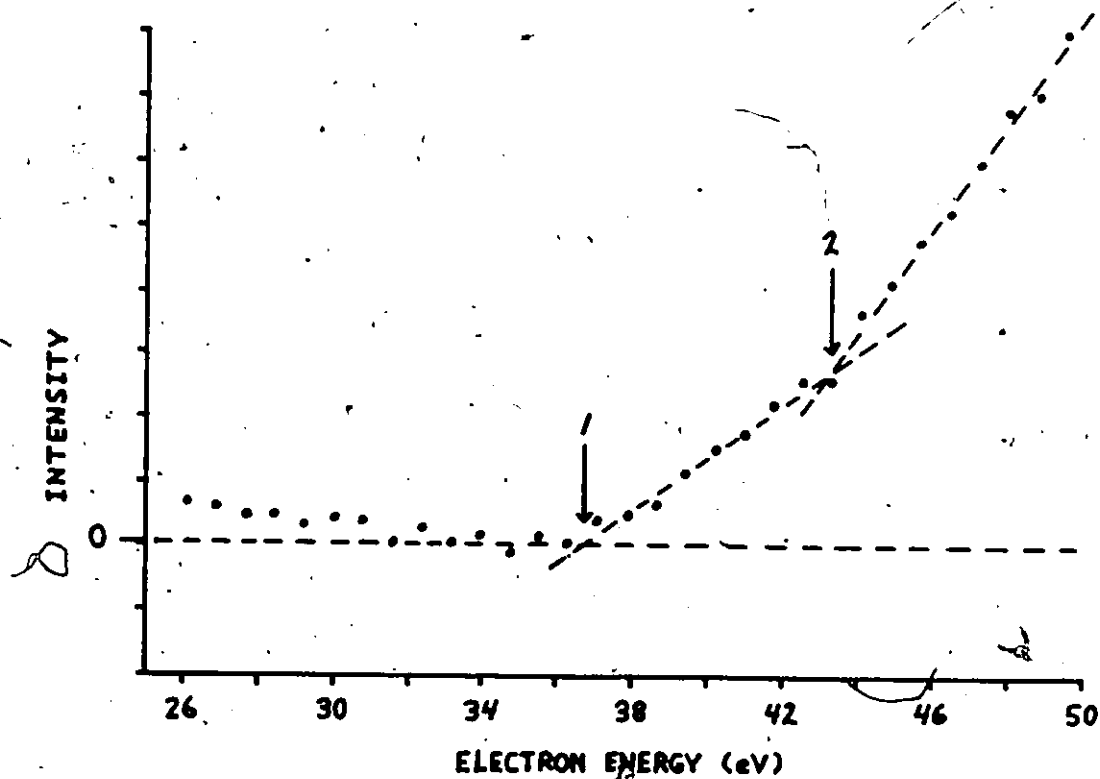
Figure 43: Near-threshold excitation function of the SI emission at 147.4 nm. Note the two onsets indicated by 1 and 2.

SII 91 nm
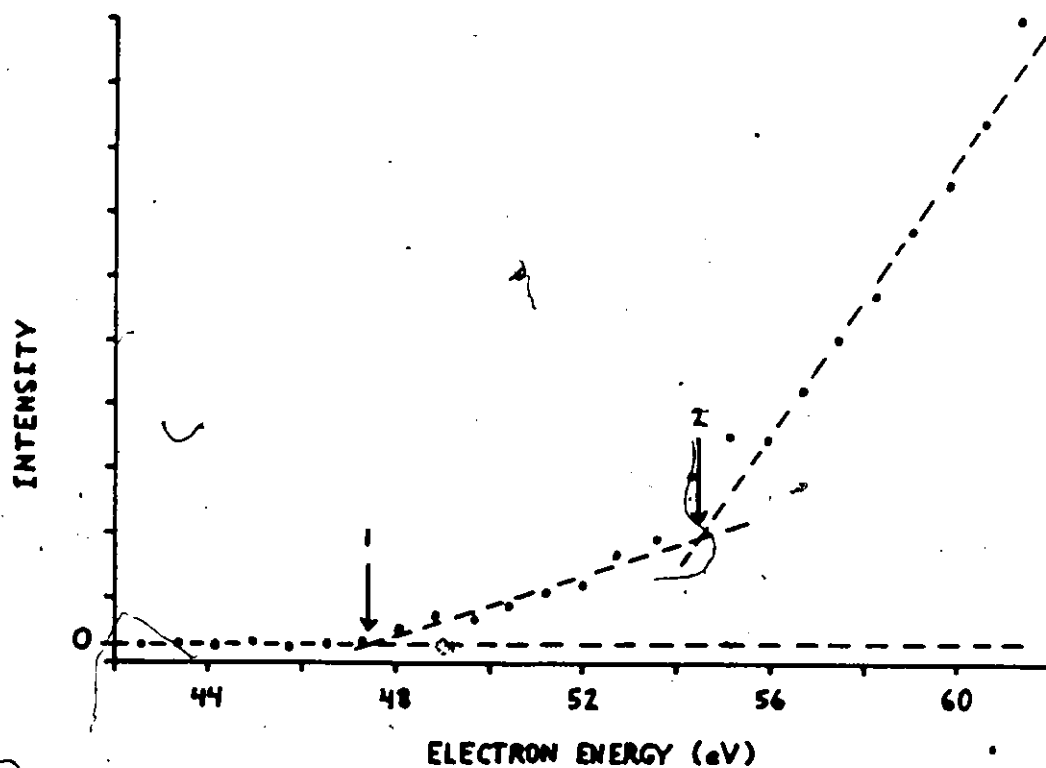
Figure 44: Near-threshold excitation function of the SII emission at 91 nm. Note the two onsets indicated by 1 and 2.

SII 100 nm
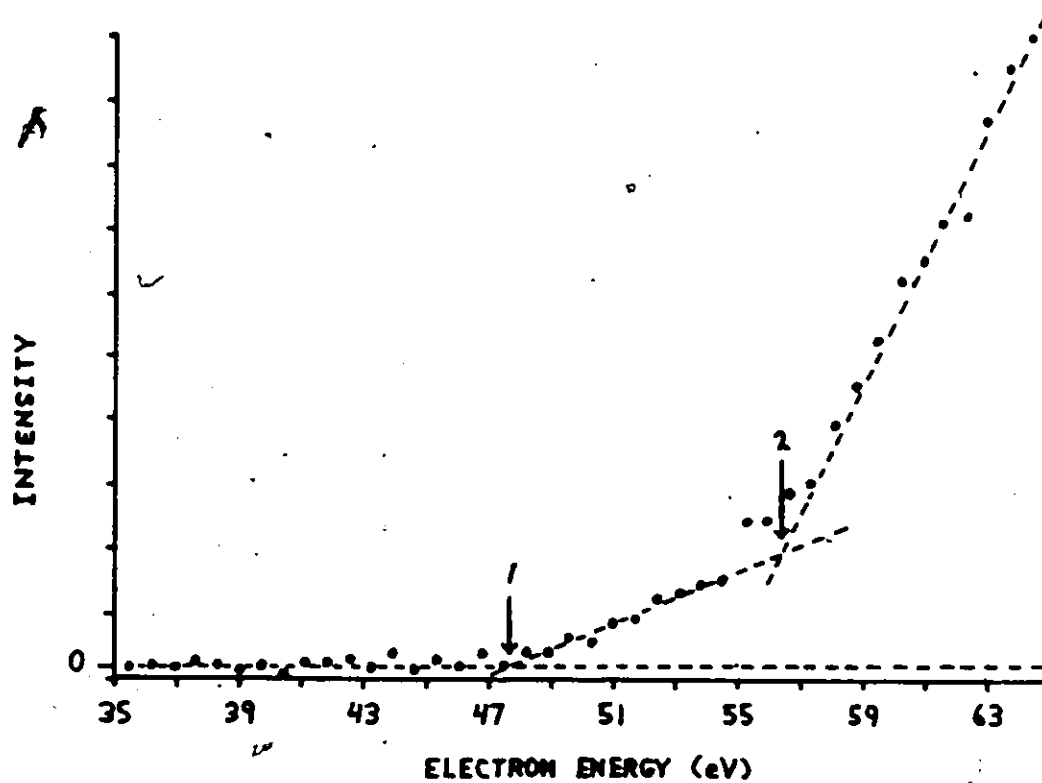
Figure 45: Near-threshold excitation function of
the SII emission at 100 nm. Note the
two onsets indicated by 1 and 2.

SII 120.4 nm
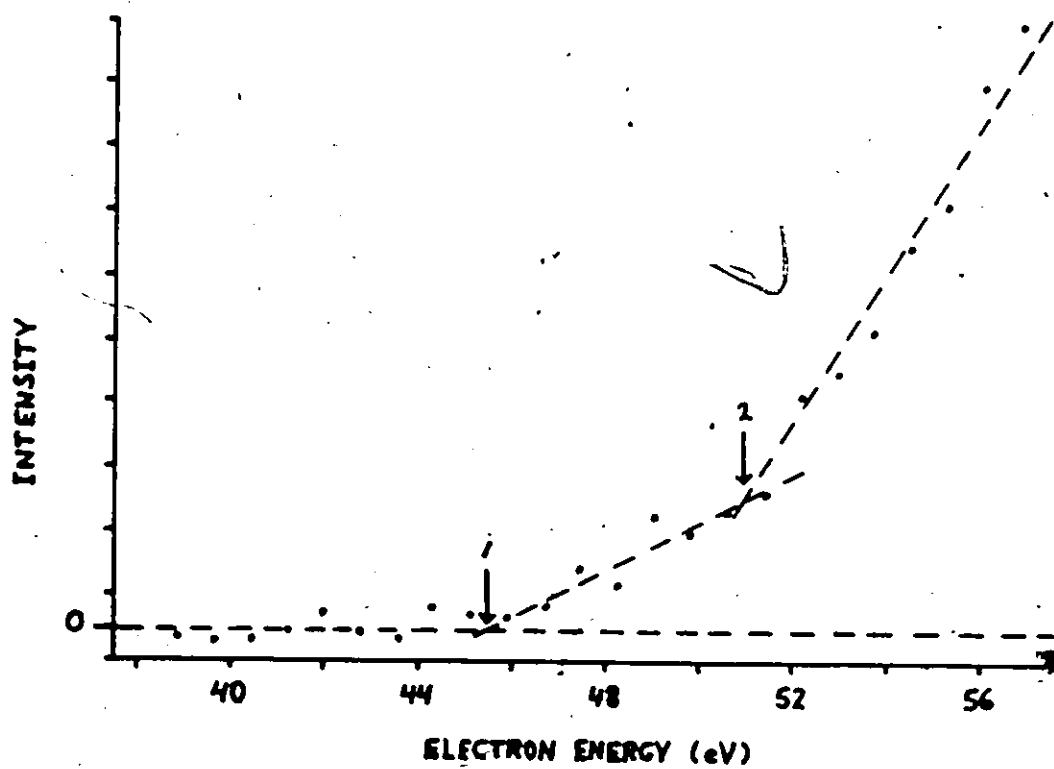
Figure 46: Near-threshold excitation function of the SII emission at 120.4 nm. Note the two onsets indicated by 1 and 2.

tation of the molecule and for any kinetic energy of the resultant fragments is approximately 29 eV for the SI emissions and 23 eV for the SII emissions. Using the JANAF Tables [42], we calculate the energy required for total fragmentation of the molecule to be 20.1 eV, which suggests that a significant amount of energy appears as kinetic energy of the seven fragments produced. We note that both Pullen and Stockdale [76] and Corr et al [20] detect fragments with several electron volts of kinetic energy.

We may compare our SII appearance potentials with those obtained for S^+ production in an electron-impact mass-spectroscopic investigation [24] of SF_6. Subtracting the excitation energies, we obtain an average value of 33.6 V for S^+ formation that is quite close to the value 37.3 ± 1 V obtained by Dibeler and Mohler [24], and 37.5 ± 1 V obtained by Pullen and Stockdale [76]. The difference in the situations may be due to different amounts of energy partitioning into kinetic energy.

In the case of the FI and FII lines, we might expect partial fragmentation of the molecule to play an important role. However, the observed appearance potentials are quite high (see Table 8 and Table 9) with the exception of the first appearance potential of the FII 60.7 nm line at 43.5 ± 1.5 V. If the ionization and excitation energies are taken into consideration, then approximately 6 eV is left for the dissociation process. This would be consistent with partial

fragmentation of the parent molecule. The second onset in the FII curve occurs some 15 eV higher, suggesting that the process being observed here, is again total fragmentation. We note that Dibeler and Mohler [24] concluded that total fragmentation was the dominant process contributing to F+ formation.

For the FI lines, approximately 21 eV is available after the excitation energies are subtracted from the appearance energies. Again, this is close to the energy required for total fragmentation and much higher than that required for partial fragmentation, so total fragmentation is likely to be the dominant process. We note, however, that other possibilities, for example, the breakup into $SF_4 + F + F^*$ cannot be ruled out.

Finally, we draw attention to the broad peaks observed in the energy-loss spectra following electron impact on SF_6 [91]. Many of these occur above the first ionization limit at about 16 eV [24], with a particularly strong feature close to 23.5 eV and less distinct features at 20 and 29 eV. The breadth of these features suggests that they may be associated with dissociation processes. Our work indicates that total fragmentation of the molecule is particularly strong and suggests that at least one of these peaks in the energy-loss spectra is associated with this channel. This molecule would be a particularly good candidate for a coincidence experiment, which is needed to further clarify this situation.

5.5 Conclusions

Neutral or ionized excited atomic fragments are formed
with significant probabilities following electron impact on
SF_6. During fragmentation of the molecule, promotion of one
of the outer atomic p electrons to an s or d orbital is the
most probable excitation channel, though excitation of an
inner-shell s electron can also occur.

From the broad, structureless shape of the excitation
functions, it is clear that the initial excitations in the
parent molecule are optically allowed. The double onsets,
which were observed in all the transitions studied, indicate
that at least two channels are contributing to the excita-
tion of the various excited species observed.

Consideration of the energetics involved in the formation
of excited S and S^+, where total fragmentation must be
occurring, indicated that a significant amount (several eV)
of energy must appear as kinetic energy of the fragments
produced. Total fragmentation of the molecule also seems to
be the dominant channel for excited F production.

Chapter VI

II (120 nm)

AN IMPORTANT H₂ EMISSION CROSS SECTION

6.1 Introduction

We have studied this emission due to its importance in
planetary atmospheres, especially our own. In our own
atmosphere it is an important auroral emission. Consequent-
ly, it is required for a detailed analysis of the extensive
terrestrial airglow and auroral data obtained by satellites
and rockets (for example Buffman et al., 1980 [40] and Gen-
tieu et al., 1979 [32]). Several researchers have previously
studied the emission; Bumma and Zipf (1971) [69], Aarts and
de Heer (1971) [2], Ajello (1970) [7], and Ajello and She-
mansky (1985) [6].

Due to its proximity to the H₂ Lyman alpha emission we
are able to use our recent cross section at 100 eV as a ref-
erence cross section. The experimental arrangements were
exactly the same as for the SF₆ work of the previous chap-
ter, thus the experimental procedure is identical, and will
not be discussed further.

6.2 Results

As in the previous chapter an intensity versus source pressure curve was obtained. It is shown in Figure 47. The parameters for the fit are $S = 17.84 \pm 3\%$ and $P_i = 133 \pm 17\%$. An estimate of the molecular diameter for N_2 is given in Appendix A.

Our value for the NI $3s^4P \longrightarrow 2p^3 \; ^4S^0$ multiplet emission at 120 nm following 200 eV electron impact on N_2 is $2.98 \times 10^{-18} \; cm^2 \pm 12\%$. Table 12 lists our present value and those of Ajello and Shemansky (1985), Mumma and Zipf (1971), and Aarts and de Heer (1971). The listed values for Ajello and Shemansky, and Mumma and Zipf have been normalized to our present value for the H_2 Lyman alpha cross section at 200 eV ($5.05 \times 10^{-18} \; cm^2$). See Chapter 5 for more details.
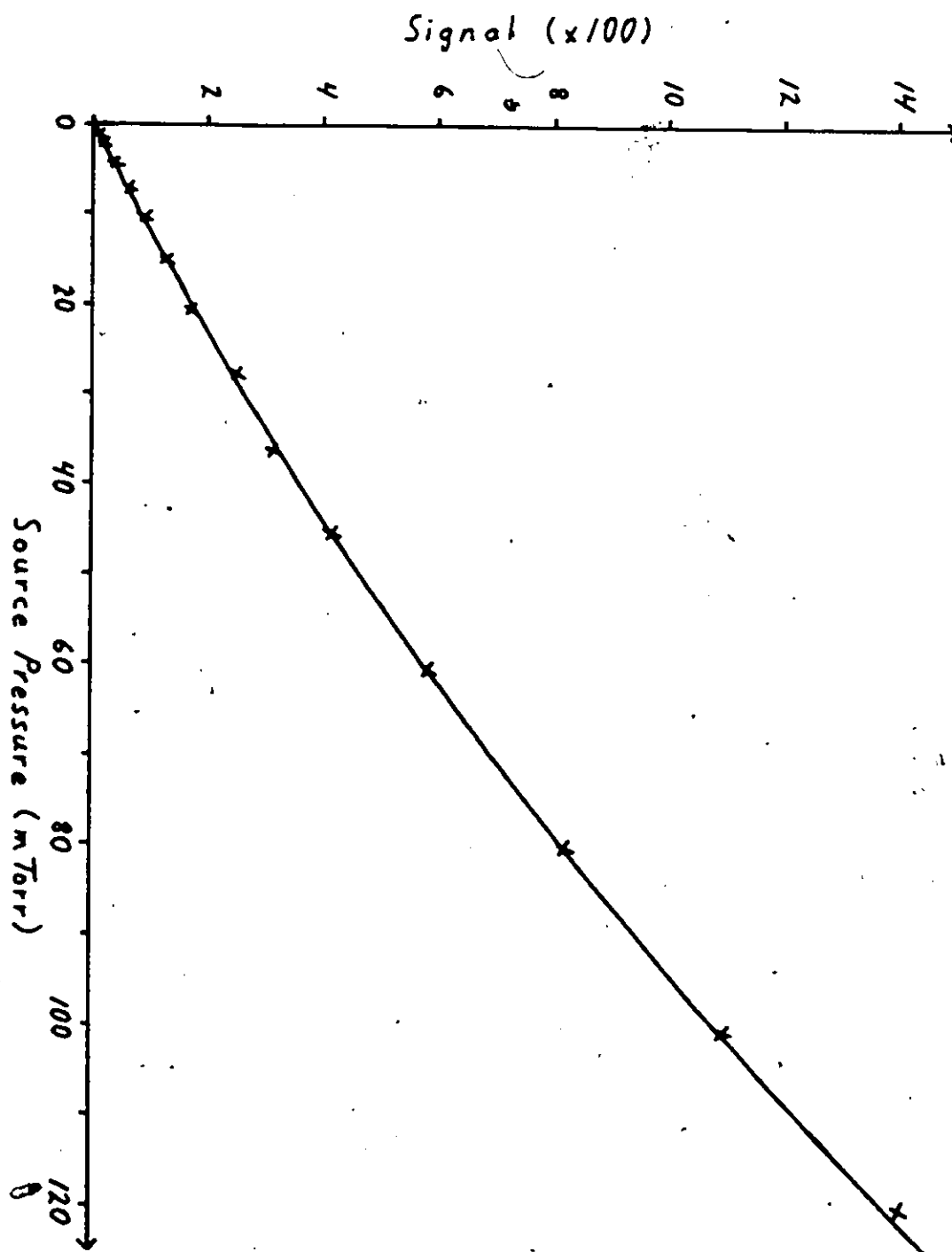
Figure 47: Intensity of the NI 120 nm emission following 200 eV electron impact on N_2 versus source pressure.

Table 12:   NI 120 nm emission cross sections.

Emission cross section data for the NI $3s^4P \longrightarrow 2p^3\ ^4S^0$ multiplet at 120 nm following 200 eV electron impact or N_2 in units of $10^{-18}\ cm^2$.

Present	(a)	(b)	(c)
2.98	3.04	3.06	3.47
±12%	±16%	±18%	±30%

(a) : Ajello and Shemansky (1985) [6].
      Normalized to our H_2 Lyman alpha cross section.

(b) : Mumma and Zipf (1971) [68].
      Normalized to our H_2 Lyman alpha cross section.

(c) : Aarts and de Heer (1971) [2].

6.3   Conclusion

As can be seen from Table 12 our present results are in excellent agreement with both Ajello and Shemansky, and Mumma and Zipf.   Aarts and de Heer use their CO emission cross section at 159.7 nm [3] as their standard.   It is based on the inelastic electron scattering data of Lassettre et al [45][46].   Nevertheless, all the results are well within the error bars.   Our error is largely due to the uncertainty in the H_2 Lyman alpha cross section (9%).   The remainder is due to systematic and statistical errors.

Chapter VII

HYDROGEN DISCHARGE EXPERIMENT

LYMAN ALPHA

7.1   Introduction

Electron impact excitation of atomic hydrogen to the 2p state is a fundamental scattering process which gives rise to Lyman alpha radiation at 121.6 nm.

$$e^- + H(1s) \longrightarrow H(2p) + e^- \longrightarrow H(1s) + e^- + Ly\,\alpha \qquad (1)$$
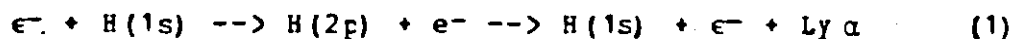
However, it is much easier to study molecular hydrogen, since unlike atomic hydrogen, it does not require a special source. Thus it is of practical importance, especially for the calibration of optical instruments in the V.U.V., to consider the production of Lyman alpha radiation following the dissociative excitation of molecular hydrogen.

$$e^- + H_2 \longrightarrow H(2p) + H(nl) + e^-$$
$$\longrightarrow H(1s) + Ly\,\alpha \qquad (2)$$
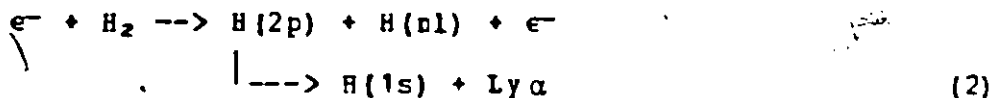
The cross section for the production of Lyman alpha by process (2) has been used as a calibration standard in the V.U.V. for fifteen years.   In aeronomy, cross sections for the dissociative excitation of nitrogen, oxygen and hydrogen are of special interest.   Lyman alpha intensities have even

- 139 -

been monitored during the Voyager space probe programme adding to its importance in modelling planetary atmospheres.

The cross section for (2) is based on both experimental and theoretical studies of (1). It was first studied experimentally by Fite and Brackmann (1958) [27] using a tungsten furnace to dissociate the molecular hydrogen and an oxygen filter, bounded by lithium fluoride windows, to isolate the Lyman alpha radiation from the surrounding molecular radiation and other atomic radiation. A later study by Long, Cox and Smith (1968) [53] also used a tungsten furnace. However, they did not use an oxygen filter. Instead they used nitric oxide as the ionizing gas in their ion chamber, and MgF_2 (or LiF) as their window. Thus they could only detect radiation between 113 nm (or 105 nm) and 134 nm (the ionization threshold of NO). Their excitation function for (1) was normalized to the Born approximation at 200 eV after a cascade correction of 2%. As the polarization is zero at 200 eV (Ott et al [71]), no correction for the possible polarization of the radiation is required. At 100 eV electron impact their cross section is 6.0×10^{-17} $cm^2 \pm$ 3% (see Kauppila et al, 1971 [43]). This cross section has been used as a standard ever since. It is an apparent cross section as it is corrected neither for cascade nor for any polarization of the radiation. However, it can be corrected for polarization using the measurements of Ott et al.

In 1971, Kauppila et al determined the ratio of the apparent emission cross sections from atomic hydrogen to the countable ultraviolet (CUV) radiation (total radiation transmitted by an oxygen filter bounded by lithium fluoride windows) from molecular hydrogen, following electron impact. They calculated a value of 4.05. ± 0.07 at 100 eV. From the data of Carriere and de Heer [18] and McGowan and Williams [60], Mumma and Zipf (1971) [67] allowed that 80% ± .10% of the CUV radiation was due to Lyman alpha. Putting these results together, Mumma and Zipf established the cross section for Lyman alpha produced by process (2) to be 1.2 x 10^{-17} cm² ± 11% at 100 eV electron impact energy. Recent work by van Zyl et al (1985) [95], Ligtenberg et al (1985) [50] [51], Ajello and Shemansky (1985) [4], Shemansky et al (1985) [78], and Woolsey et al al. (1986) [104], based on various pieces of evidence and using various calibration procedures, have suggested that this cross section needs to be revised downwards by at least 30%. The principal reason why the value of Mumma and Zipf needs to be revised is due to a lowering of the fraction of the CUV radiation which is due to Lyman alpha. For a further discussion of this subject, see Shemansky et al [78].

In view of the uncertainties surrounding the currently accepted values, we have remeasured the cross section ratio for the production of Lyman alpha by (1) and (2). Two basic problems in the early measurements have been identified.

First, the transmission of lithium fluoride windows is affected by x-rays generated by the impact of electrons having energies greater than about 100 eV. Second, and more important, oxygen-filtered radiation includes both Lyman alpha and molecular radiation. Owing to the unavailability of O_2 absorption data taken at the high pressures at which O_2 filters are used, it is extremely difficult in practice to estimate accurately the fraction of molecular radiation which penetrates the various O_2 windows. In our present study, we use neither a lithium fluoride window nor an oxygen filter.

7.2 Apparatus

The key to our technique is our use of an rf discharge source of the type described by Slevin and Stirling (1981) [92] in conjunction with a VUV 0.5 meter Seya-Namioka mounted McPherson monochromater. The spectrometer allows us to isolate the Lyman alpha radiation produced, when the discharge is either on or off, from the surrounding molecular radiation. A complete schematic (see Figure 3) and general discussion of the experimental setup is given in Chapter 3. Therefore, only those parts of the apparatus having to do with the discharge source will be discussed. Figure 49 to Figure 52 illustrate these parts.

7.3 The RF Source

Radio frequency discharges have been used by a number of investigators, for example, Toonies et al (1974) [89], Bouver et al (1974) [39], and Slevin and Sterling (1981) [92]. All three groups used similar sources/ In our experiment we have employed the source of Slevin and Sterling. They have achieved dissociation fractions of about 95% and number densities between 5×10^{11} and 2×10^{13} atoms/cm^3, compared to the 10^{10} atoms/cm^3 typical of tungsten oven sources. However, Slevin and Sterling operated at higher source pressures than we do. We have found that for source pressures (measured using a capacitance manometer) between 30 and 70 mTorr, the measured dissociation fraction varies from approximately 35% to 70%. Figure 52 shows the location of the capacitance manometer.

7.3.1 Theory of Operation

The dissociation of molecular hydrogen by DC electric discharges and radio frequency discharges has been experimentally investigated by a number of researchers (see Corrigan [21] and references therein). They agree that the dissociation in the discharges is a direct result of electron impact. Corrigan (1965) [21] investigated the dissociation rate of hydrogen molecules by electron impact as a function of the electron energy and found that the minimum energy required to cause dissociation was 8.8 ± 0.2 eV. He also found that the dissociation rate increased rapidly up to

about 14 eV. The onset energy (8.8 eV) is very close to the energy of excitation from the ground state, $^1\Sigma g$, to the lowest repulsive state, $^3\Sigma u$, of H_2. The next higher state which could readily cause dissociation is the $^3\Sigma g$ state at 11.8 eV. Excitation to this state from the ground state and subsequent decay to the lowest repulsive state would result in dissociation. Thus, for electron impact between 8.8 and 11.8 eV, hydrogen molecules can yield only the $^3\Sigma u$ state. The potential energy curves for the three states are shown in Figure 48.

The repulsive $^3\Sigma u$ state dissociates into two ground state hydrogen atoms; however, excitation of H_2 to higher states will yield hydrogen atoms in excited states and other products such as H^+, H^-, H_2^-, and H_2^+. The excited states of atomic hydrogen will decay to either the ground (1s) state or the metastable (2s) state. However, the RF field within the body of the discharge causes the (2s) state to mix with the (2p) state; consequently, the lifetime of the (2s) state is greatly reduced and the contribution of excited states of atomic hydrogen to the output beam from the source is expected to be small. In fact we did not detect any Lyman alpha radiation when, with the electron beam off, an electric field of 300 V/cm was applied. Contributions from the other products are also negligible.

Accordingly, the ideal condition for dissociating hydrogen molecules into ground state hydrogen atoms is achieved
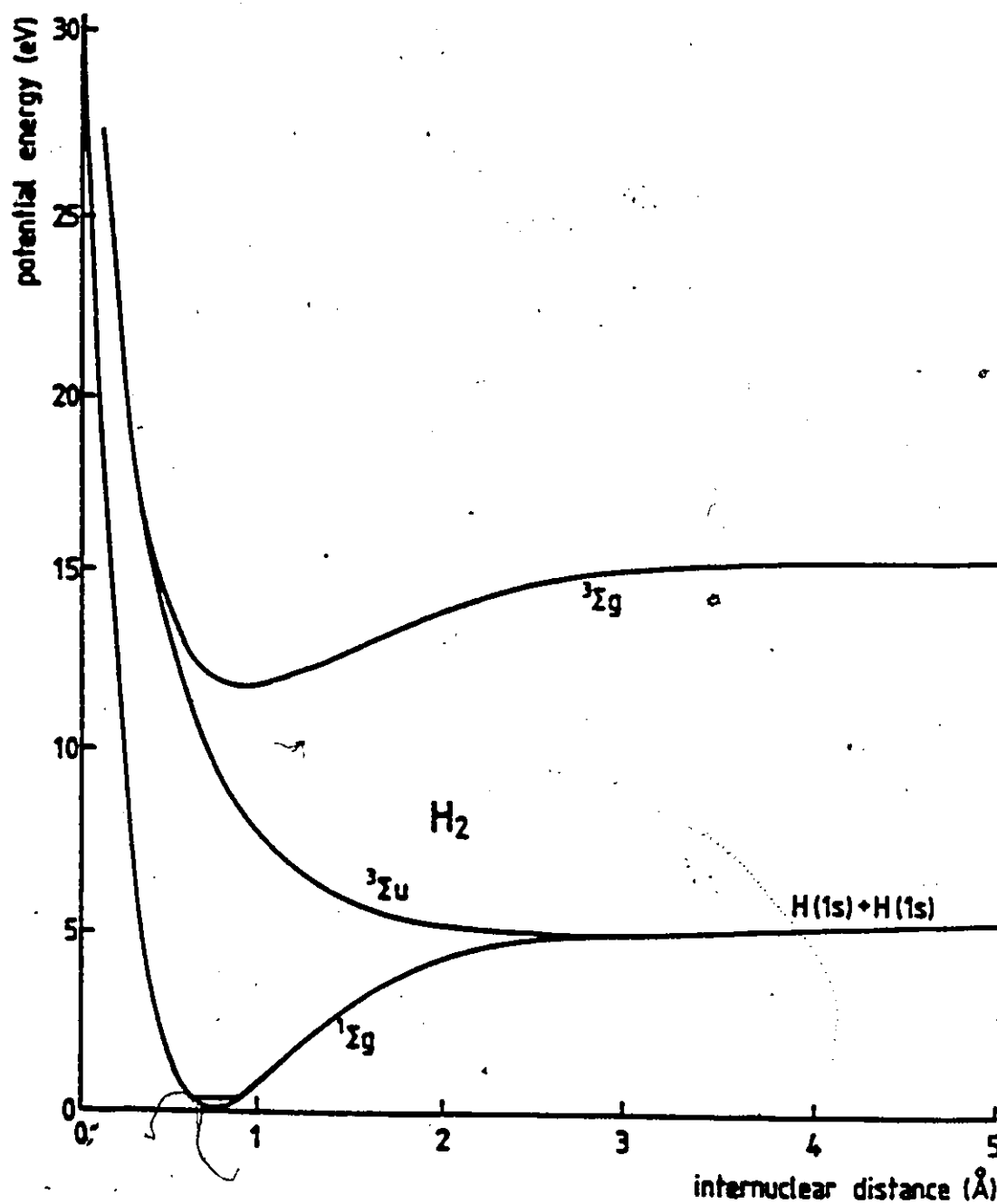
Figure 48: H_2 potential energy curves. Shown is the $^1\Sigma_g$ ground state, the lowest repulsive state, $^3\Sigma_u$, and the next triplet state, $^3\Sigma_g$.

by accelerating electrons within the discharge to between 8.8 and 11.8 volts. The Slevin and Sterling source produces an oscillating electric field within a resonant coaxial cavity and can supply 50 Watts of RF power at 35 MHz.

7.3.2 Details of the Source

The complete source, including its cylindrical vacuum tank, is shown in Figure 49. The discharge tube and RF cavity are shown in greater detail in Figure 50.

Figure 49 illustrates the manner in which the discharge tube is attached to its cylindrical vacuum tank and the important electrical, gas, and water connections. To allow exterior adjustments to the position of the source flexible bellows are employed.
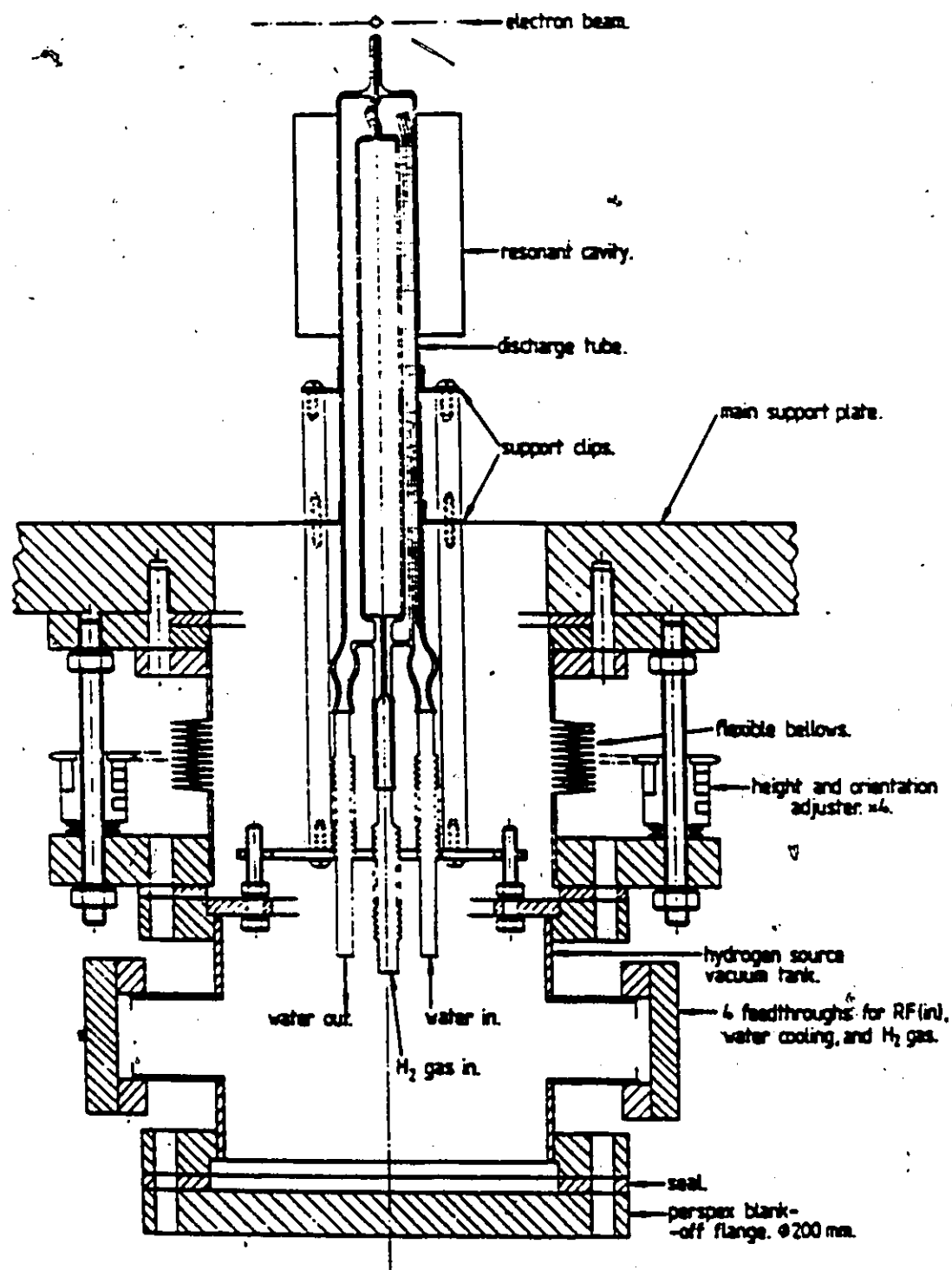
Figure 49: Illustrated is the complete rf-discharge source including it's vacuum tank and external connections.

7.3.2.1 The Discharge Tube

The discharge tube (see Figure 50) is constructed from pyrex and consists of a 220 mm long central tube with an 18 mm bore within which the discharge occurs. It is terminated at the gas exit by a 1 mm inner diameter capillary tube and at the gas entrance by a 2 mm inner diameter capillary tube. The capillaries prevent the discharge from spreading out of the main tube. Note the magnified inset of Figure 50. It depicts the shape of our nozzle, which is slightly different from that shown on the tube. The shape of the nozzle considerably reduces any spreading of the discharge out of the tube and helps to thermalize the beam. The central tube is surrounded by a water cooling jacket. The water is essential to inhibit the recombination of hydrogen atoms into molecules on the pyrex surface of the tube. Wood and Wise (1962) [103] have studied the process extensively. While the pyrex walls of the discharge tube have a low recombination coefficient for hydrogen atoms, the presence of even a monolayer of some impurities on its surface greatly increases the recombination coefficient. Thus besides water cooling, the tube must be thoroughly cleaned.

The cleaning process is performed in a fume hood due to the hazards associated with using hydrofluoric acid. Protective rubber gloves and a rubber smock are used for additional safety. The cleaning solvents are sucked into the discharge through the exit nozzle using a venturi pump. The procedure is as follows:

1. At least two washes with hot acetone. Allow the solvent time to act.

2. Thoroughly rinse the tube with distilled water in order to remove the acetone and any debris.

3. One wash with a 30% hydrofluoric acid solution. Allow the acid to act for about 45 seconds.

4. Thoroughly rinse the tube with distilled water in order to remove the remaining HF solution and any debris.

5. If the tube has recently been used in the discharge further applications of 30% HF solution followed by a thorough rinsing may be necessary.

After cleaning, the source is immediately mounted on the main vacuum chamber and the entire system is pumped down.
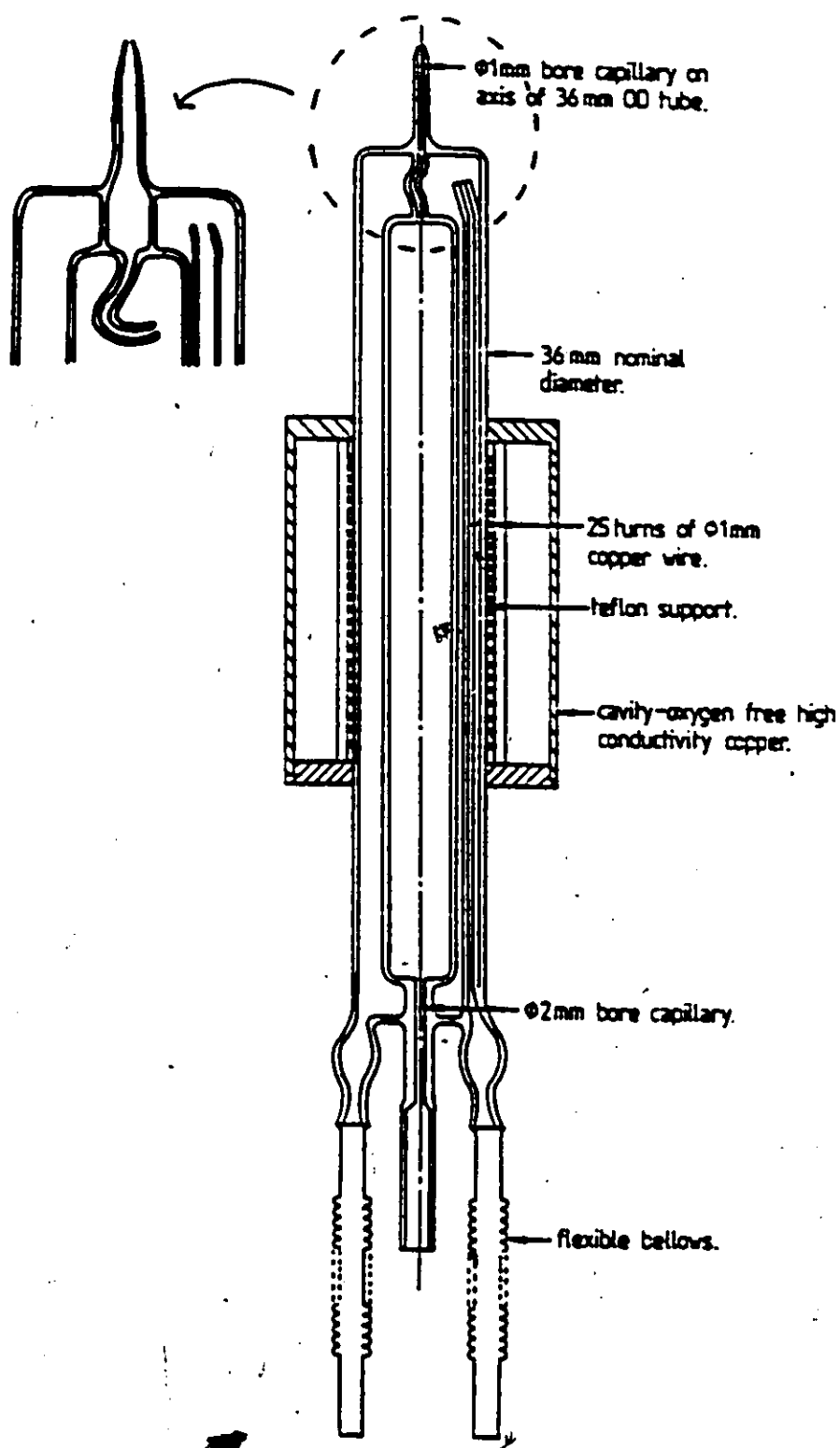
Figure 50: Illustration of the discharge tube and rf cavity. The magnified inset shows our nozzle. It is configured differently from some previous nozzles.

7.3.2.2 RF Cavity and Generator

The coaxial resonator cavity is 70 mm in diameter, 99 mm high and consists of a 25 turn helical inner conductor. The advantage to using a helical resonator is size. An equivalent coaxial line resonator would be about 2.5 m for the wavelengths of about 10 m which are used to drive it. The properties of a helical resonator are discussed by MacAlpine and Schildknecht [55]. The outer part of the cavity is constructed from a solid piece of high conductivity oxygen free copper.

The resonant cavity is driven by an impedance matched RF generator identical to that used by Slevin and Sterling (1991). The generator can deliver a maximum of 80 Watts RF power at about 35 MHz and can be tuned to match the load characteristics of the cavity. Tuning of the cavity is normally performed with a 50 ohm dummy load.

7.3.2.3 The Water Cooling System

A schematic of the water cooling system is shown in Figure 51. The system consists of two separate water lines. Distilled water is circulated through the cooling jacket of the discharge tube and the heat which it is carrying is removed by the heat exchanger. The heat exchanger consists of two concentric copper coils. The distilled water flows through one coil and tap water flows through the other. The flow of water through the cooling jacket is controlled by a flow sensor. If the flow rate drops too low, the RF genera-

tor, water pump, and the two solenoid valves are shut off
until they are reset. Thus, the water system protects the
discharge tube from overheating, and should prevent the
apparatus from acquiring too much water if a leak occurs
inside the vacuum system. The reservoir can hold 1 liter and
the total amount of distilled water in the system is not
more than 2 or 3 liters. The reservoir is used principally
during startup and to replace any water lost through evapo-
ration or due to minor leaks outside the vacuum system.
Inside the vacuum system we have used Swagelok fittings in
order to avoid the possibility of leaks. The advantage of
our design is that the cooling water circulates in a closed
system and by using distilled water we have removed the need
of filtering the mains water. This improves the life of the
source as the water jacket remains much cleaner.
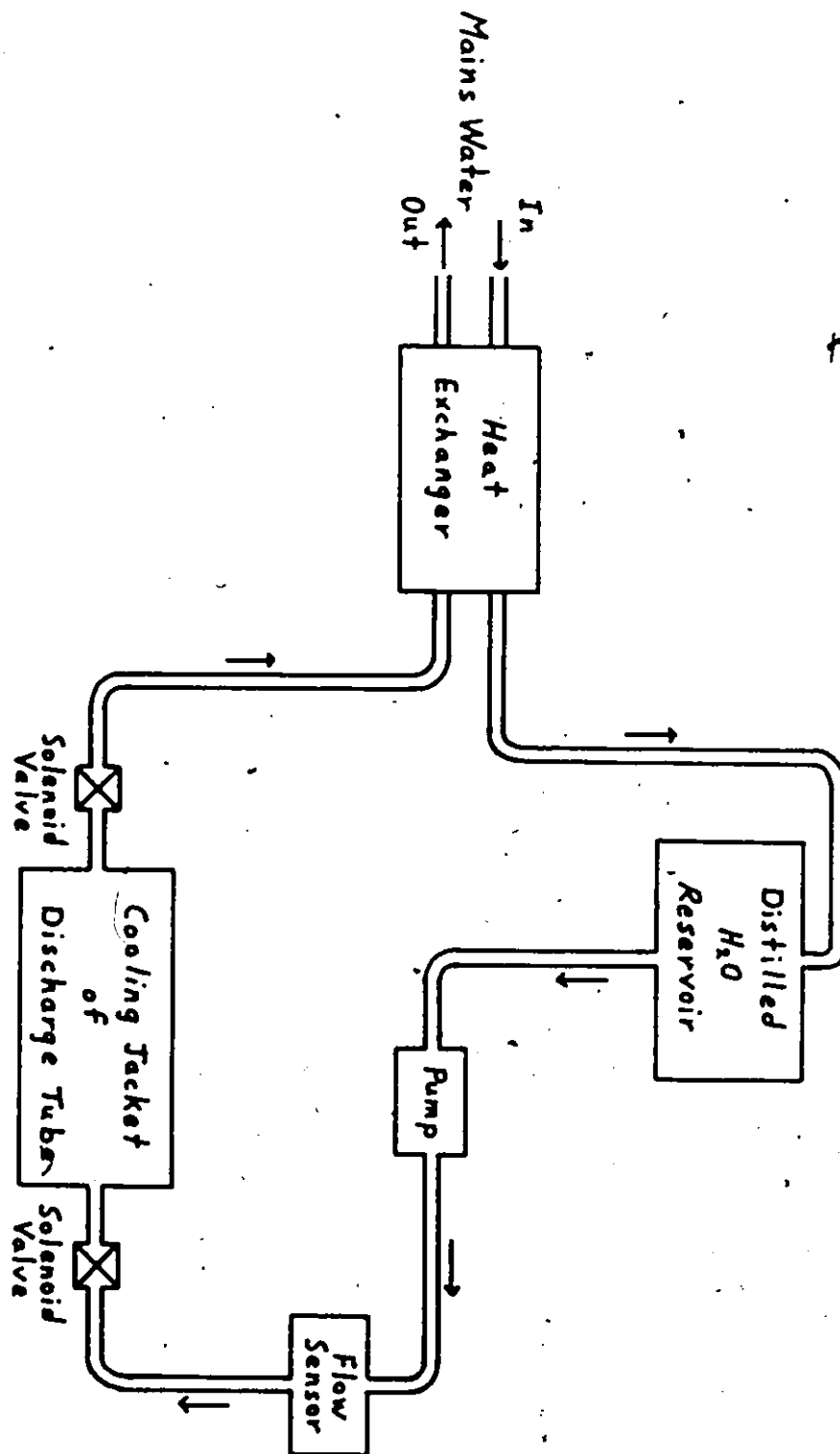
Figure 51: The water cooling system.

7.3.2.4   The Gas Handling System

The gas handling system, shown in Figure 52, is very important. In order to ensure longer life to the source and high dissociation rates, it is necessary to supply clean hydrogen gas to the hydrogen source. All the gas lines which could possibly come into contact with the hydrogen gas were made from 316 stainless steel tubing joined with swage-lok fittings, except for the copper tubing used between the gas cylinder (purity 99.99%) and valve 1. Conflat flanges were used on the cross (gas reservoir). The elements of the gas system were carefully cleaned prior to assembly and tested for leaks after assembly. After being pumped down the system was baked (maximum temperature 450 C) in order to remove any lingering impurities from the system. In order to ensure greater purity of the hydrogen gas admitted to the hydrogen source a palladium leak valve (properties are discussed by Viennet et al (1973) [96]) is used. Only hydrogen diffuses easily through the palladium. The rate of diffusion is controlled by an electrical current which is passed through the palladium (i.e. it is temperature dependent). Thus, by applying a constant current to the palladium leak valve a constant flow of clean hydrogen gas can be supplied to the source. Typical currents are between 1 and 3 amperes.
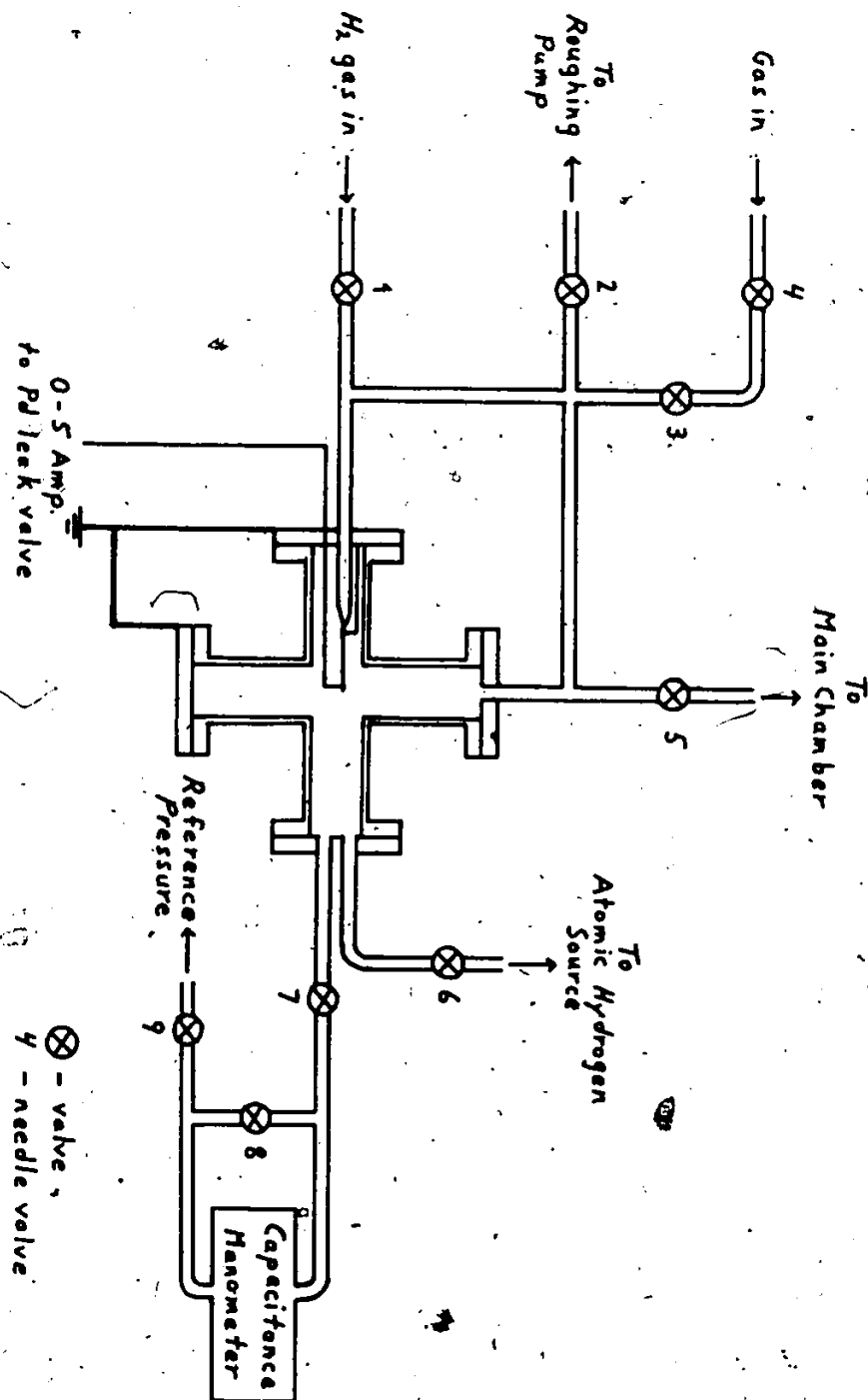
Figure 52: The gas handling system.

7.4   Procedure and Method

The initial development relating the H_2 Lyman alpha emission cross section to the H Lyman alpha emission cross section was done by Fite and Brackmann (1958) [27]. In order to highlight the subtleties involved with the relevant equations, a thorough discussion will be given.

7.4.1   Constant Mass Flow

An important observation, which connects the signal detected when the discharge is off to that detected when it is on, is the condition of constant mass flow through the source. This condition exists due to our fine control of the flow of molecular hydrogen into the gas reservoir (the cross) and consequently into the discharge tube. Secondly, the pressure due to the molecular gas in the reservoir is accurately monitored by a capacitance manometer. By maintaining a constant current (with slight adjustments) to the palladium leak valve, a constant pressure can be maintained in the reservoir, and the flow of molecular hydrogen into and out of the source will remain constant whether the discharge is on or off. Mathematically, the condition of constant mass flow can be stated as follows:

$$F_1(H_2;v) = F_2(H_2;v) = F_1^1(H_2;v)$$

$$= F(H_2;v) \tag{1a}$$

$$\text{and} \quad F(H_2) = \sum_v F(H_2;v) \tag{1b}$$

where the superscript "1" denotes that the discharge is on, and $P(H_2;v)$ is the mass flow of molecular hydrogen in the state, v. The subscripts "1" and "2" denote cross sectional areas at the entrance to the source and at the exit of the source, respectively. This nomenclature will be used from now on. Equation (1a) states that the flow of molecular hydrogen, in the state v, into the source when the discharge is either on or off, and the mass flow of molecular hydrogen out of the source when the discharge is off are equal. Equation (1b) states that the total flow of molecular hydrogen in all states remains constant. A second relation is given by

$$P_1(H_2) = \sum_n F_2^1(H:n) + \sum_{v'} F_2^1(H_2;v') . \tag{2}$$

Equation (2) states that the total mass flow of molecular hydrogen into the source equals the total mass flow of molecular hydrogen and the total mass flow of atomic hydrogen out of the source when the discharge is on. The sums are over the mass flow rates of atomic hydrogen, in the state n, and molecular hydrogen, in the state v'.

As mentioned in the previous section, no significant amount of excited atomic hydrogen flows out of the source. Secondly, the distribution of molecular states in the gas when it flows out of the source is the same whether the discharge is on or off. The basic reason for these observations is due to the ability of the source to thermalize the

emitted gas.   In cther words the gas is in thermal equilib-
rium and the temperature of the emitted gas is the same as
that of the gas entering the scurce.   To prove this asser-
tion we performed the following experiment.   Using helium,
as the gas, we measured the He (58.4 nm) emission signal per
unit electron current with the discharge both on ard off.
Using the results of Chapter 2, Appendix B, and assuming
constant mass flow when the discharge is both on ard off,
the fcllowing equation can be derived.

$$\frac{S}{S^1} = \left(\frac{T^1}{T}\right)^{\frac{1}{2}} \tag{3}$$

S and S^1 are the signals per unit electron current when the
discharge is respectively on and off, and T and T^1 are the
respective kinetic temperatures. Frcm several measurements,
we found a value of 1.00 ± 0.01 for the ratio. The equality
of the population distribution for molecular hydrogen is
further supported by Figure 53 which shows the Lyman series
for atomic hydrogen.   Note how flat and uniform the back-
ground is.   The spectra was formed by subtracting a normal-
ized molecular spectrum (discharge off) from the spectrum
obtained when the discharge is on.   From the above discus-
sion we can confidently rewrite equation (2) as

$$F_2(H_2) = F_2^1(H) + A\ F_2(H_2) \tag{4}$$

where $F_2^1(H)$ = mass flow rate of H(1s) atoms   (5a)

and $F_2^1(H_2;v) \propto F_2(H_2;v)$ (5b)

and*λ is a constant related tc the dissociation fraction.

Figure 53: Spectra from 90 to 125 nm with the discharge
off, on, and the atomic hydrogen Lyman series
(molecular signal removed).

Electron Impact Energy =200 eV, $\Delta\lambda_{FWHM}$ =3.4 Å

Discharge OFF

Discharge ON

INTENSITY (Arb. Units)

LYMAN Series

α

β

γ

δ

ϵ

WAVELENGTH (Å)
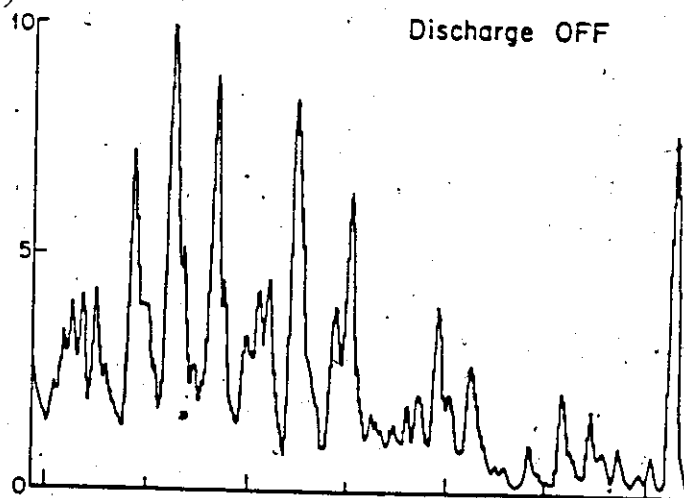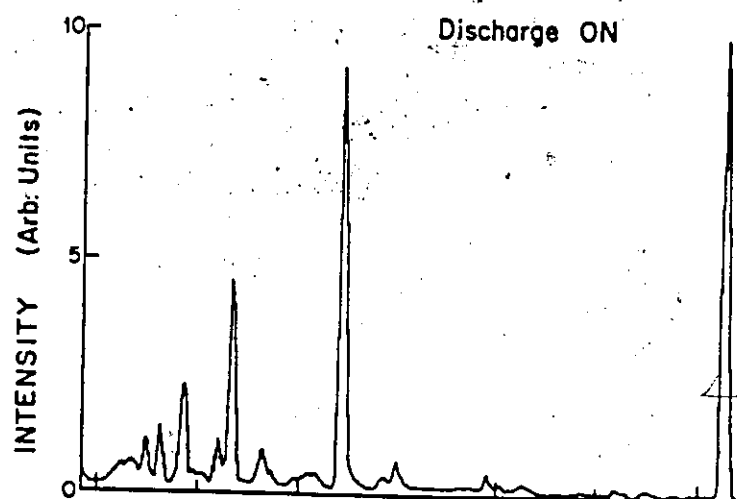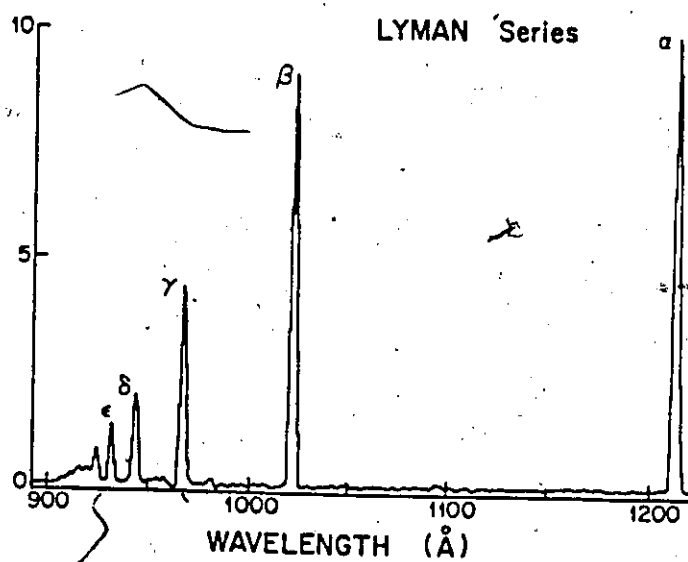
7.4.2   Dissociation Fraction

The dissociation fraction produced by the source is an important quantitative characteristic. It can be defined as the mass flow rate of hydrogen atoms out of the source divided by the total mass flow rate out of the source. Thus

$$
D = \frac{F_2^1(H)}{F_2^1(H) + F_2^1(H_2)} = \frac{F_2^1(H)}{F(H_2)} = 1 - \frac{F_2^1(H_2)}{F(H_2)} \tag{6}
$$

where we have made use of equation (5). Using equation (4) it can be shown that the constant A equals 1-D. In other words it gives the fraction of hydrogen molecules which are not dissociated.

To determine the dissociation fraction we perform two measurements. We measure the same molecular emissions with the discharge both on and off and the ratio gives a measure of the dissociation fraction. This is done by setting the monochromator at a vibrational emission and using wide entrance and exit slits in order to increase the detected signal. Several vibrational transitions were selected throughout our experiment, and as expected, similar values for the dissociation fraction were obtained. The detected signals per unit electron current when the discharge is on and off are given by equations (7a) and (7b) respectively.

$$S(H_2) = \frac{B}{(T \, m(H_2))^{\frac{1}{2}}} \cdot F_2(H_2) \, Q(H_2) \qquad (7a)$$

and

$$S^1(H_2) = \frac{B}{(T^1 \, m(H_2))^{\frac{1}{2}}} \, F_2^1(H_2) \, Q(H_2) \qquad (7b)$$

B is a geometric constant, $m(H_2)$ is the mass of molecular hydrogen and $Q(H_2)$ is the total apparent cross section. The ratio of equations (7a) and (7b) gives

$$\frac{S^1(H_2)}{S(H_2)} = \left(\frac{T}{T^1}\right)^{\frac{1}{2}} \frac{F_2^1(H_2)}{F_2(H_2)} \qquad (8)$$

or

$$D = 1 - \left(\frac{T^1}{T}\right)^{\frac{1}{2}} \frac{S^1(H_2)}{S(H_2)} \qquad (9)$$

Thus, by using our result for the ratio of the temperatures and measuring $S^1(H_2)$ and $S(H_2)$ we are able to determine the dissociation fraction, D.

7.4.3   Apparent Cross Section Ratio

The ratio of the apparent cross sections (not corrected for polarization, cascade or molecular fraction) of the H Lyman alpha emission to the H_2 Lyman alpha emisssion can be determined by two measurements. The two measurements consist of measuring the amount of radiation emitted within the resolution of our monochromator (we use narrow entrance and exit slits) at the Lyman alpha wavelength with the discharge

respectively on and off. The signals per unit electron current for the discharge on and off are given by equations (10a) and (10b) respectively.

$$S_\alpha = \frac{E}{(T\ m(H_2))^{\frac{1}{2}}} Q^\alpha(E_2)\ F(H_2) \tag{10a}$$

$$S_\alpha^1 = \frac{B\ D(H)}{(T^1)^{\frac{1}{2}}} \left[\frac{Q^\alpha(H_2)\ F_2^1(H_2)}{m(H_2)^{\frac{1}{2}}} + \frac{Q^\alpha(H)\ F_2^1(H)}{m(H)^{\frac{1}{2}}} \right] \tag{10b}$$

$m(H)$ is the mass of atomic hydrogen, $Q^\alpha(H_2)$ is the apparent cross section for the molecular hydrogen emissions near Lyman alpha, $Q^\alpha(H)$ is the apparent cross section for atomic Lyman alpha, and $D(H)$ is the trapping factor of the Lyman alpha radiation due to atomic hydrogen. The determination of the trapping factor will be given in the following section.

Taking the ratio of equations (10a) and (10b) gives the following result.

$$\frac{S_\alpha^1}{S_\alpha} = D(H) \left(\frac{T}{T^1}\right)^{\frac{1}{2}} \left[\frac{F_2^1(H_2)}{F(H_2)} + \left(\frac{m(H_2)}{m(H)}\right)^{\frac{1}{2}} \frac{F_2^1(H)}{F(H_2)} \frac{Q^\alpha(H)}{Q^\alpha(H_2)} \right] \tag{11}$$

Rearranging equation (11), using equation (6), and using $m(H_2) = 2m(H)$, we can rewrite it in it's final form;

$$\frac{Q^\alpha(H)}{Q^\alpha(H_2)} = \frac{1}{\sqrt{2}\ D} \left[\left(\frac{T^1}{T}\right)^{\frac{1}{2}} \frac{S^1}{D(H)\ S_\alpha} - (1 - D) \right] \tag{12}$$

which, except for the inclusion of the trapping factor, is identical to that derived by Fite and Brackmann [27].

7.4.4 Trapping Factor

Unlike most gases we can not determine the trapping fac-tor for Lyman alpha by atomic hydrogen directly. This is due to the change in the dissociation fraction with source pressure. However, by using the measured absorption coeffi-cient for the He (58.4 nm) transition and the theoretical trapping coefficient between H(2p-1s) and He(2p-1s), it can be determined. Table 13 gives various fitting parameters, including absorption coefficients, for a number of gases, including helium, which are used in both this and the next chapter. Table 14 lists trapping coefficients connecting the atomic hydrogen Lyman series to He(2p-1s). From Appen-dix B, the trapping factor is given by

$$D(H) = \exp(-K \, G(L) \, n'(H))$$ (13)

where K is a transition dependent constant, $G(L)$ is a geom-etry dependent constant, and $n'(H)$ is the atomic hydrogen target number density. Using equation (6) the atomic hydro-gen number density can be expressed in terms of the molecu-lar number density when the discharge is off. Thus

$$D \, F(H_2) = \sigma(H_2) \, n(H_2) \, v(H_2) \, A \, D$$
$$= \sigma(H) \, n'(H) \, v(H) \, A = F_2^{1}(H)$$ (14)

where $v(H_2)$ and $v(H)$ are the respective flow velocities for molecular and atomic hydrogen, $n(H_2)$ is the molecular hydrogen number density, and A is an appropriate area. Assuming that the flow velocities have a $(T/m)^{\frac{1}{2}}$ dependence, equation (14) can be rewritten as

$$n^1(H) = \left(\frac{2T}{T^1}\right)^{\frac{1}{2}} \Gamma \quad n(H_2) \tag{15}$$

and, the exponent in equation (14) becomes

$$K \, G(L) \, n^1(H) = K \, G(L) \left(\frac{2T}{T^1}\right)^{\frac{1}{2}} D \, n(H_2) \tag{16a}$$

$$= \alpha \left(\frac{2T}{T^1}\right)^{\frac{1}{2}} D \, f(\bar{P}, \bar{P}_i) \tag{16b}$$

where α is the Lyman alpha absorption coefficient, and $f(P, P_1)$ is the form of the number density for molecular hydrogen. It's functional shape is shown in Figure 55 and it's fitting parameters are given in Table 13. Upon using the trapping coefficient, we have our final result for the exponent. It equals

$$\alpha_{He} \gamma \left(\frac{2T}{T^1}\right)^{\frac{1}{2}} D \, f(\bar{P}, \bar{P}_i) \tag{17}$$

where α_{He} is the absorption coefficient for helium and γ is the trapping coefficient. The helium absorption coefficient is calculated from the intensity versus pressure plot of Figure 54.

TABLE 13

Intensity versus pressure fitting parameters[*]
for the discharge source

Molecule (Line)	$S(\lambda)$	P_i (mTorr)	α (mTorr^{-1})
He (58.4 nm)	142.3 ± 1.4%	741.2	0.00338 ± 14.2%
Ar$^+$ (92.0 nm)	39.80 ± 2.1%	265.9 ± 7.9%	0
Ar (104.8 nm)	123.7 ± 4.5%	265.9	0.0425 ± 4.7%
Ar (106.7 nm)	55.4 ± 6.2%	265.9	0.0168 ± 14.3%
H$_2$ (Lyman α)	66.0 ± 1.1%	469.3	0

[*] $S(\lambda,E,P) = S(\lambda,E) \ f(P/2,P_i/2)\exp[-\alpha \ f(P/2,P_i/2)]$

TABLE 14

Oscillator strengths, F values and trapping coefficients,

Line (nm)	Absorption[a] Oscillator Strength	F	γ[b]
He (2p-1s) 58.4 nm	0.2762 ± 1%	1.001	-
H (2p-1s) 121.6 nm	0.4162 ± 1%	1.000	1.5714 ± 2%
H (3p-1s) 102.6 nm	0.0791 ± 1%	1.134	0.2858 ± 2%
H (4p-1s) 97.3 nm	0.0290 ± 1%	1.192	0.1044 ± 2%
H (5p-1s) 95.0 nm	0.0139 ± 1%	1.223	0.0503 ± 2%
H (6p-1s) 93.8 nm	0.0078 ± 1%	1.222	0.0278 ± 2%
H (7p-1s) 93.1 nm	0.0048 ± 1%	1.222[c]	0.0170 ± 2%
H (8p-1s) 92.6 nm	0.0032 ± 1%	1.222[c]	0.0112 ± 2%

(a) From National Bureau of Standards [9].

(b) Assumed equal to that for n = 6.

(c) $\gamma = \alpha_H(np-1s)/\alpha_{He}(2p-1s)$

Figure 54: Intensity of the He 58.4 nm emission following
100 eV electron impact on He versus source
pressure (discharge source).
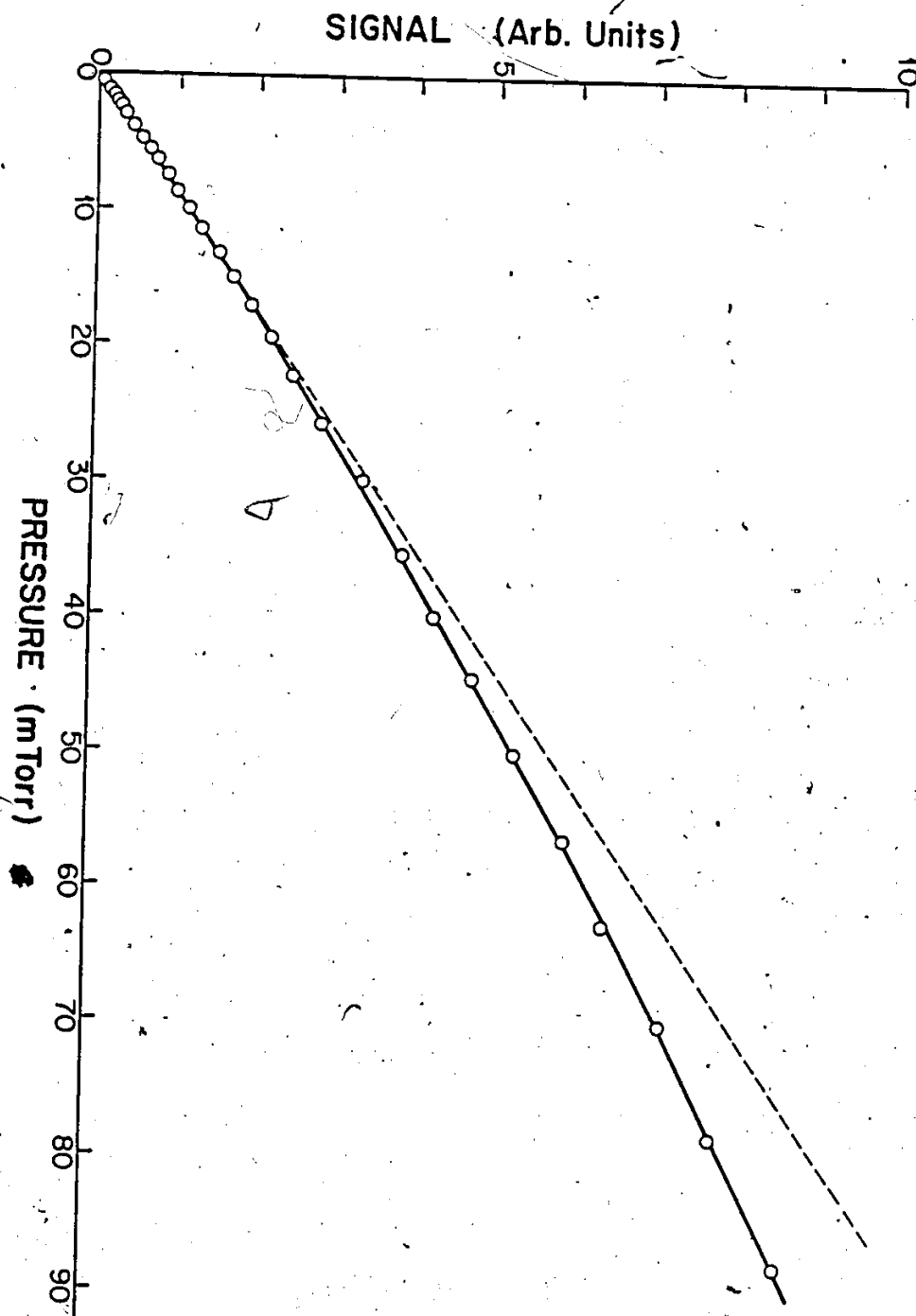
Figure 55: Intensity of the Lyman alpha emission following
100 eV electron impact on H_2 versus source
pressure (discharge source).
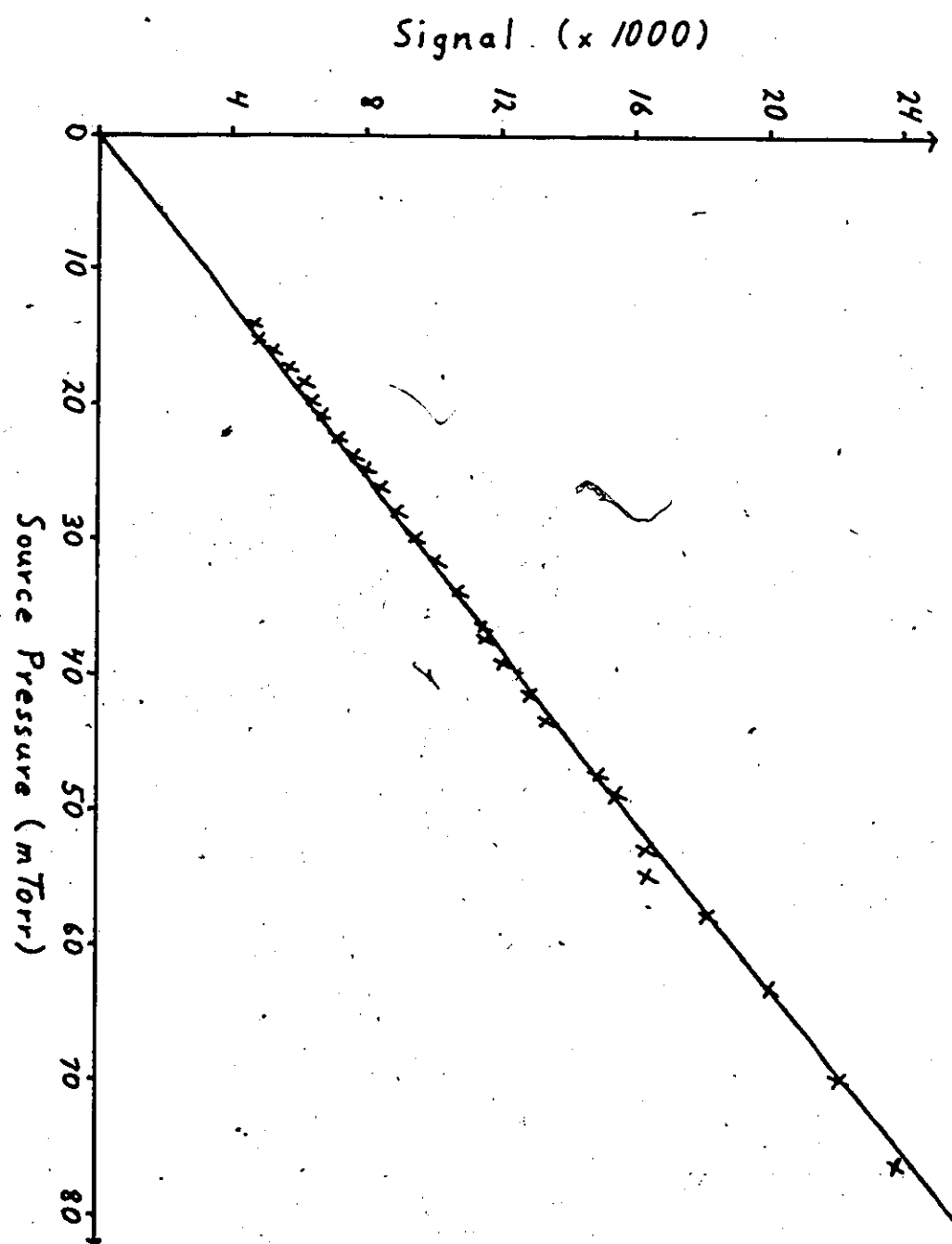
7.4.5   Concluding Remarks

In order to arrive at the absolute H_2 Lyman alpha emission cross section using the apparent cross section ratio, several further steps must be taken. In our case we use the apparent Lyman alpha emission cross section for atomic hydrogen due to Long, Cox and Smith (1968) [53] as our standard at 100 eV electron impact energy. This allows us to determine the apparent H_2 cross section at the Lyman alpha wavelength. To make it absolute two corrections must be applied. First, we must remove any contribution due to molecular vibrational transitions, and second, we must correct for any possible polarization.

The polarization has been determined by Ott et al [71]; however, the molecular fraction is dependent upon the resolution of the monochromator and must be determined for every setting of the monochromator's entrance and exit slits. The molecular fraction was determined using a synthetic model of the Werner and Lyman bands, convoluted with the resolution of our monochromator, and comparing its intensities with that of an experimental spectrum with the same resolution. For equal entrance and exit slits a triangular instrumental transmission function could be used for the synthetic spectrum. A detailed discussion of the synthetic spectrum's construction and an example are given in Appendix C. The following ratio is used to determine the molecular fraction.

$$\frac{I_e(Ly\,\alpha\;;EN;EX)}{I_s(Ly\,\alpha\;;EN;EX)} = \frac{I_e(\lambda\;;EN;EX)}{I_s(\lambda\;;EN;EX)} \qquad (19)$$

EN and EX are the respective entrance and exit slit widths and the subscripts "e" and "s" denote the experimental and synthetic spectra respectively. λ is the wavelength of a vibrational transition adjacent to the Lyman alpha $(Ly\,\alpha)$ wavelength, and the I's are the relevant vibrational intensities. Thus, equation (18) allows us to place the amount of signal due to the vibrational transitions at Lyman alpha on an absolute scale. As a result, the molecular fraction can be expressed as,

$$M(EN;EX) = \frac{I_e(Ly\,\alpha\;;EN;EX)}{I_T(Ly\,\alpha\;;EN;EX)} \qquad (19)$$

such that M is the molecular fraction and I_T is the total intensity (vibrational and H_2 Lyman alpha) at the Lyman alpha wavelength, for entrance and exit slits, EN and EX. Table 15 lists our calculated molecular fractions for several entrance and exit slit widths. The results are not in conflict with those of Shemansky and Ajello [78], who calculate the molecular fraction integrated over the full width of the Lyman alpha profile obtained from a spectral scan. Our measurement corresponds to the molecular fraction at the Lyman alpha wavelength. We do not perform a spectral scan.

* Table 15

Molecular fractions.

Molecular fractions for several entrance and exit slit widths of the monochromator

Slit widths (mm) Entrance/Exit	Molecular Fraction M (EN; EX)
0.01/0.01	0.004 ± 0.004
0.02/0.02	0.025 ± 0.020
0.03/0.03	0.060 ± 0.030

Combining the above results with our value for the ratio of the apparent cross sections, finally gives us the H_2 Lyman alpha emission cross section. It is given by

$$Q^{\alpha}_{em}(H_2) = \frac{\varsigma^{\alpha}(H_2)}{\varsigma^{\alpha}(H)} Q_{LCS}(H) \; (1 - M)(1 - p/3) \qquad (20)$$

where p is the polarization of the radiation and $Q_{LCS}(H)$ is the apparent Lyman alpha emission cross section of Long, Cox and Smith [53].

7.5 Results

The data from a large number of measurements, taken on different days with different source pressures, dissociation fractions, discharge conditions, source tubes, beam interaction geometries, detector slit widths and gratings yielded very consistent results. The final value given in Table 17, $(7.09 ± 0.58) \times 10^{-18}$ cm², is the mean of 24 separate deter-

minations. Table 16 shows a variety of parameters for the different measurements while Figure 56 illustrates their distribution about the mean. We note that if the two extreme values are excluded, so that only 22 separate determinations are considered, a value of $(7.13 \pm 0.47) \times 10^{-18}$ cm^2 is obtained. The errors represent one standard deviation. Errors in the individual determinations came from a combination in quadrature of the error of 3% quoted by Long, Cox and Smith for their H Lyman alpha cross section, and the errors due to fluctuations in the experimentally measured parameters. These errors were all in the 5 to 8% region. It is clear from Table 17, that the present measurement has enabled a considerable reduction in error over most of the previous work.

Table 17 also lists other data so as to illustrate the level of agreement between recent measurements. All four recent measurements are consistent with one another within their combined error limits and all lie significantly below the earlier value given by Mumma and Zipf (1971).
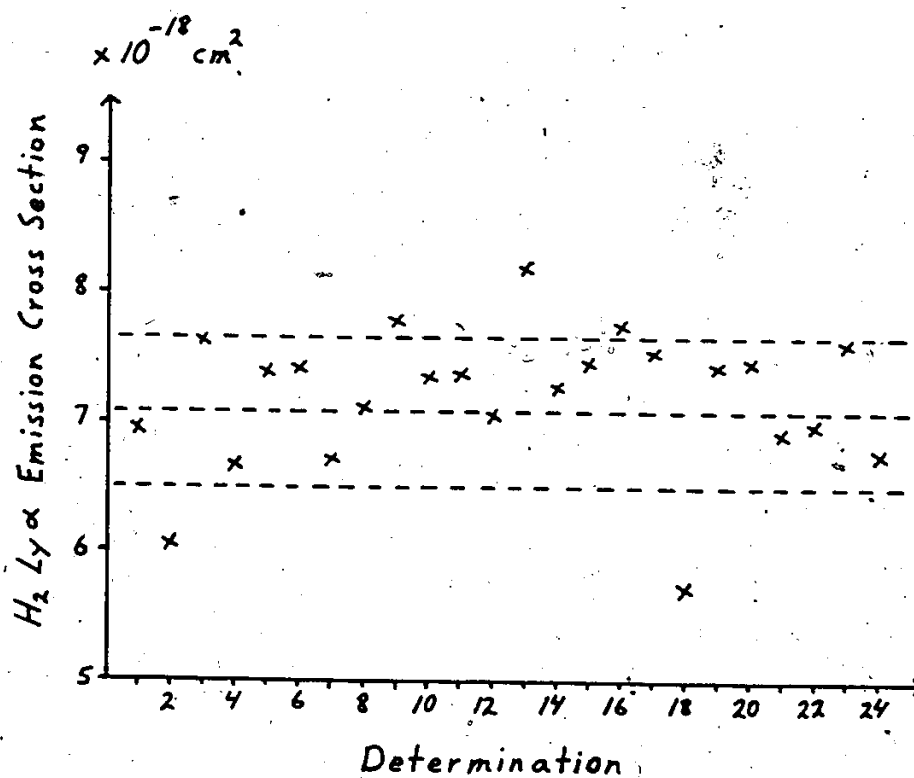
Figure 56: Plot of the 24 separate determinations of
the H_2 Lyman alpha emission cross section.
The dashed lines represent one standard
deviation about the mean (central dashed
line).

TABLE 16

24 separate determinations of the H_2 Ly α emission
cross section and other relevant data

Determination (Date) 1985	Source	Slit Widths Ent./Exit (mm)	Source Pressure (mTorr) ± 0.5	Dissociation Fraction ± 1-3%	H_2 Ly α Cross Section (x 10^{-18} cm^2) ± 5-8%
1. Sept. 16	#1	0.1/0.1	50.3	0.69	6.95
2. Sept. 18	#1	0.1/0.1	50.0	0.67	6.06
3. Sept. 19	#1	0.1/0.1	50.0	0.71	7.63
4. Sept. 20	#1	0.1/0.1	50.0	0.72	6.67
5. Sept. 24	#1	0.1/0.12	49.5	0.67	7.39
6. Sept. 24	#1	0.1/0.12	52.0	0.67	7.42
7. Sept. 25	#1	0.1/0.1	57.0	0.71	6.72
8. Sept. 25	#1	0.1/0.1	56.0	0.68	7.11
9. Sept. 26	#1	0.2/0.2	56.0	0.68	7.78
10. Sept. 27	#1	0.1/0.1	39.5	0.57	7.34
11. Sept. 27	#1	0.15/0.1	37.0	0.50	7.36
12. Oct. 30	#2	0.2/0.2	67.0	0.41	7.05
13. Oct. 30	#2	0.2/0.2	67.0	0.51	8.19
14. Oct. 31	#2	0.2/0.2	50.0	0.45	7.27
15. Oct. 31	#2	0.2/0.2	60.0	0.49	7.46
16. Oct. 31	#2	0.2/0.2	70.0	0.48	7.74
17. Nov. 1	#2	0.3/0.3	50.0	0.49	7.53
18. Nov. 6	#2	0.2/0.2	49.0	0.51	5.72
19. Nov. 7	#2	0.2/0.2	49.6	0.59	7.42
20. Nov. 8	#2	0.2/0.2	49.0	0.59	7.45
21. Nov. 9	#2	0.2/0.2	49.0	0.56	6.91
22. Dec. 9	#2	0.2/0.2	49.8	0.56	6.98
23. Dec. 9	#2	0.2/0.2	40.5	0.51	7.60
24. Dec. 12	#2	0.2/0.2	27.4	0.34	6.75
Weighted Average					7.08

TABLE 17

Cross sections for production of Ly α
following 100 eV electron impact on H_2

References	Q_{H_2} (100eV) $(x\ 10^{-18} cm^2)$
Present work	7.08 ± 0.58
Mumma and Zipf, 1971	12.3 ± 1.4
Van Zyl et al, 1985[a]	7.22 ± 1.36
Shemansky et al, 1985[b]	8.2 ± 1.2
Ligtenberg et al, 1985[c]	6.57 ± 0.53

[a] A somewhat indirect calibration procedure was used here
based on a detailed study of the cascade component of
the Lyman α signal observed in H^+ rare gas collisions.

[b] Calibration was established using the H_2 Rydberg band
systems as standards and is thus traceable back to the
optical oscillator strengths for these transitions
combined with an analysis of the shapes of their exci-
tation functions.

[c] This calibration makes use of a synchrotron as a cali-
brated light source. Full details of the technique
are given in McPherson et al (1986) [62].

7.6   Discussion and Conclusion

One possible source of systematic error in the present
experiment is in the value chosen for the normalizing H
Lyman alpha cross section.   If this value is too high, then
our value for the H_2 Lyman alpha cross section would be
correspondingly high.   However, some evidence exists (as
discussed by Callaway and McDowell, 1983 [17]) in support of
a higher not lower value of the H Lyman alpha cross section
at 100 eV.   They point out that at energies lower than 100
eV, where comparisons can be made, the Long, Cox, and Smith
data lie about 15% lower than the absolute data of Williams
(1975,1981) [101] [102], and many theoretical calculations.
Against this, of course, is the fact that if the Long et al
data were scaled upwards at 100 eV, they would exceed the
Born approximation at higher energies which is very unlike-
ly.   On the other hand, the recent letter of van Wyrgaarden
and Walters (1986) [93] contends that the results of Long,
Cox, and Smith for energies from 13.4 to 200 eV is to be
preferred over the measurements of Williams.   They also
point out where the differences occur between their pseudos-
tate calculations [94], which agrees quite well with the
results of Long, Cox, and Smith, and those of Callaway and
McDowell. We plan to carefully study the energy variation of
the H Lyman alpha cross section in an attempt to resolve
these problems.

In conclusion, Table 17 makes it clear that there is a need for a comprehensive review of V.U.V. excitation cross section measurements, as many of these were calibrated against the earlier result of Mumma and Zipf.

Chapter VIII

HYDROGEN DISCHARGE EXPERIMENT :CALIBRATION

DETERMINATION OF ARGON CROSS SECTIONS

8.1 Introduction

This chapter presents part of a continuing project to use the hydrogen Lyman series emission cross sections following electron impact as a set of standards with which to calibrate optical instruments from 90 nm to 125 nm. As an illustration of its application, we present cross section measurements for the argon resonance lines at 104.8 nm and 106.7 nm, and the argon ion lines at 92.0 nm and 93.2 nm. These emissions were chosen due to their presence near Lyman beta and Lyman epsilon, and because of their importance as possible secondary standards in the V.U.V.. The argon ion lines are especially favourable candidates as they are unpolarized and are unaffected by resonance trapping. This application is especially important in our laboratory as these emission cross sections occur at wavelengths where the detection efficiency of our system (for an example, see Figure 19 or Figure 57) can change rapidly.

8.2 Calibration

The relative efficiency curve, Figure 57, is obtained
from two sources. The principal data points are obtained
from the Lyman series of atomic hydrogen. Secondary points
between 105 nm and 120 nm are obtained using molecular
hydrogen emissions and the molecular branching ratio tech-
nique [57] [1].   The Lyman emissions which are used are
Lyman alpha, Lyman beta, Lyman gamma, Lyman delta, and Lyman
epsilon.   Data relevant to the emissions is given in Table
18.

The total excitation cross sections are taken from the
Born approximation of Vainshtein (1965) [91] at 200 eV (see
also Moiseiwitsch (1968) [64]). As for Lyman alpha, the
Born approximations are expected to be dependable for the
entire Lyman series at 200 eV. To obtain emission cross
sections from the Born excitation cross sections it is nec-
essary to make several corrections.   It must be corrected
for cascade, polarization, and must include the branching
ratio of the upper state.   These terms were discussed in
Chapter 2. The necessary values are given in Table 18.
Details of the branching ratio and cascade calculations are
given in Appendix D.

The relative efficiencies were determined from two sets
of spectra.   One covered the wavelength range 89 to 122 nm
(see Figure 53) with a full-width half-maximum of 0.34 nm.
The second covered the wavelength range from 89 to 105 nm

TABLE 18

Atomic hydrogen Lyman series cross sections (x $10^{-18} cm^2$) and other relevant data at 200 eV

Line Wavelength	Total Excitation Cross Section[a]	Branching Ratio	Cascade %	Apparent Emission Cross Section
Lyman α 121.6 nm	41.6	1	3.4	43.0
Lyman β 102.6 nm	7.10	0.8816	3.1	6.45
Lyman γ 97.3 nm	2.52	0.8390	1.9	2.15
Lyman δ 95.0 nm	1.20	0.8177	0.9	0.99
Lyman ϵ 93.8 nm	0.66	0.8053	0	0.53

(a) Born approximation total excitation cross sections from Vainshtein, 1965 [91].

(b) Polarization equals zero for all emissions.

with a full-width half-maximum of 0.22 nm. The dissociation fractions obtained with the respective spectra were 0.64 and 0.40 respectively. Lyman beta was used as the reference (detection efficiency equal to unity), as it is common to both spectra and because it is near the important argon resonance lines. The formula used to calculate the relative efficiencies is obtained using results from Chapter 5, Chapter 7, and Appendix B. It is

$$\text{Eff}(\lambda) = \frac{D(\text{Ly}\alpha)}{D(\lambda)} \frac{Q_{em}(\text{Ly}\alpha)}{Q_{em}(\lambda)} \frac{S(\lambda)}{S(\text{Ly}\alpha)} \tag{1}$$

where λ represents the wavelength of a Lyman emission, $\text{Eff}(\lambda)$ is it's relative efficiency, $D(\text{Ly}\alpha)$ and $D(\lambda)$ are the respective trapping factors, $Q_{em}(\text{Ly}\alpha)$ and $Q_{em}(\lambda)$ are the respective emission cross sections from Table 18, and $S(\lambda)$ and $S(\text{Ly}\alpha)$ are the respective signals per unit electron current. The trapping factors are calculated as for Lyman alpha in Chapter 8.

Our molecular branching ratio technique consists of dividing the H_2 spectra of Figure 53 by a synthetic spectra (see Appendix C and the figure therein) of the same resolution, and normalizing the relative numbers to the relative detection efficiency at Lyman alpha.
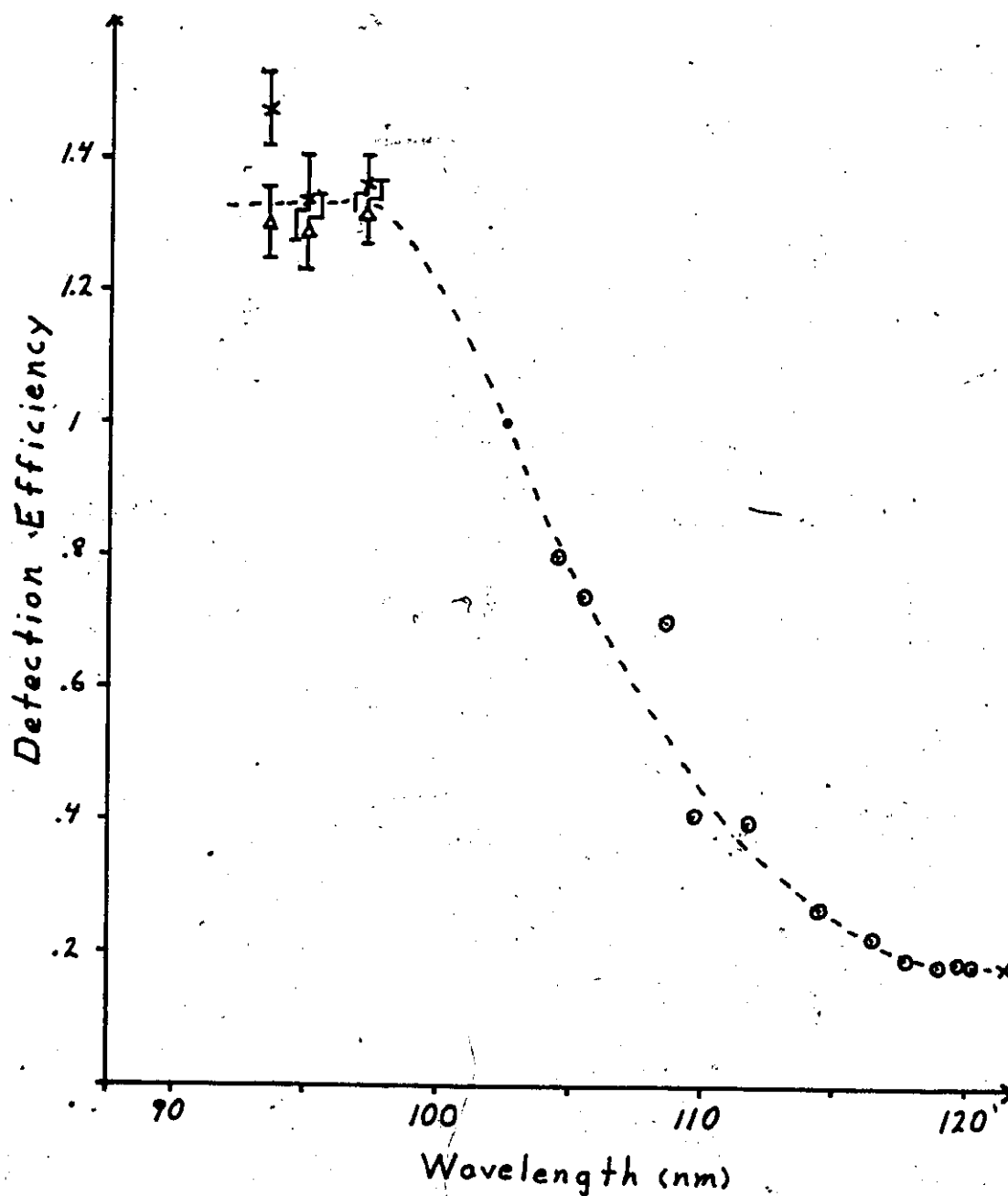
Figure 57: Relative detection efficiency as determined
by using the atomic hydrogen series, (x)
and (Δ), and a branching ratio technique
with H_2, (o). The (x) and (Δ) data points
are calculated using the spectra with
0.51 nm and 0.22 nm resolution, respectively.

8.3 Cross Sections

To determine the emission cross sections of other gases using the Lyman series emissions as standards, we follow a similar procedure to that used in Chapter 5. The scle difference is that instead of using a conventional thermal gas source, we use an atomic hydrogen source. The use of this source increases the number of measurements which have to be made, as our source does not produce 100% atomic hydrogen. In other words, we must also determine the dissociation fraction. Using results from Chapter 5, Chapter 8, and Appendix B, the apparent emission cross section for an emission (Q'_u) using a Lyman series emission as a standard (Q'_r) is given by

$$Q'_u = \frac{Eff_r}{Eff_u} \frac{D_r}{D_u} \left(\frac{2T}{T^1}\right)^{\frac{1}{2}} \frac{f(\overline{F}_r;\overline{F}_{ir})}{f(\overline{F}_u;\overline{F}_{iu})} \frac{S_u}{S_r} D \, Q'_r \qquad (2)$$

where "r" and "u" denote the reference emission and unknown emission cross section respectively. Eff are the detection efficiencies, D_r is the Lyman emission trapping factor, D_u is the trapping factor for the "unknown" emission, D is the dissociation fraction, T is the temperature of the gas for the "unknown" emission, T^1 is the temperature from the discharge source, S_r and S_u are the respective signals per unit electron current, $f(\overline{P}_u,\overline{P}_{iu})$ is the number density form for the "unknown" emission, and $f(\overline{F}_r,\overline{F}_{ir})$ is the number density form for molecular hydrogen. Parameters for many of these

terms are given in Chapter 7 (see Table 13 and Table 14). The number density form for the argon ion lines and the argon resonance lines are also given in Table 13. They are determined from the intensity versus pressure curves of Figure 58 and Figure 59.

Figure 58: Intensity of the 104.8 nm (o), and 106.7 nm (x) emissions following 100 eV electron impact on Ar versus source pressure (discharge source).
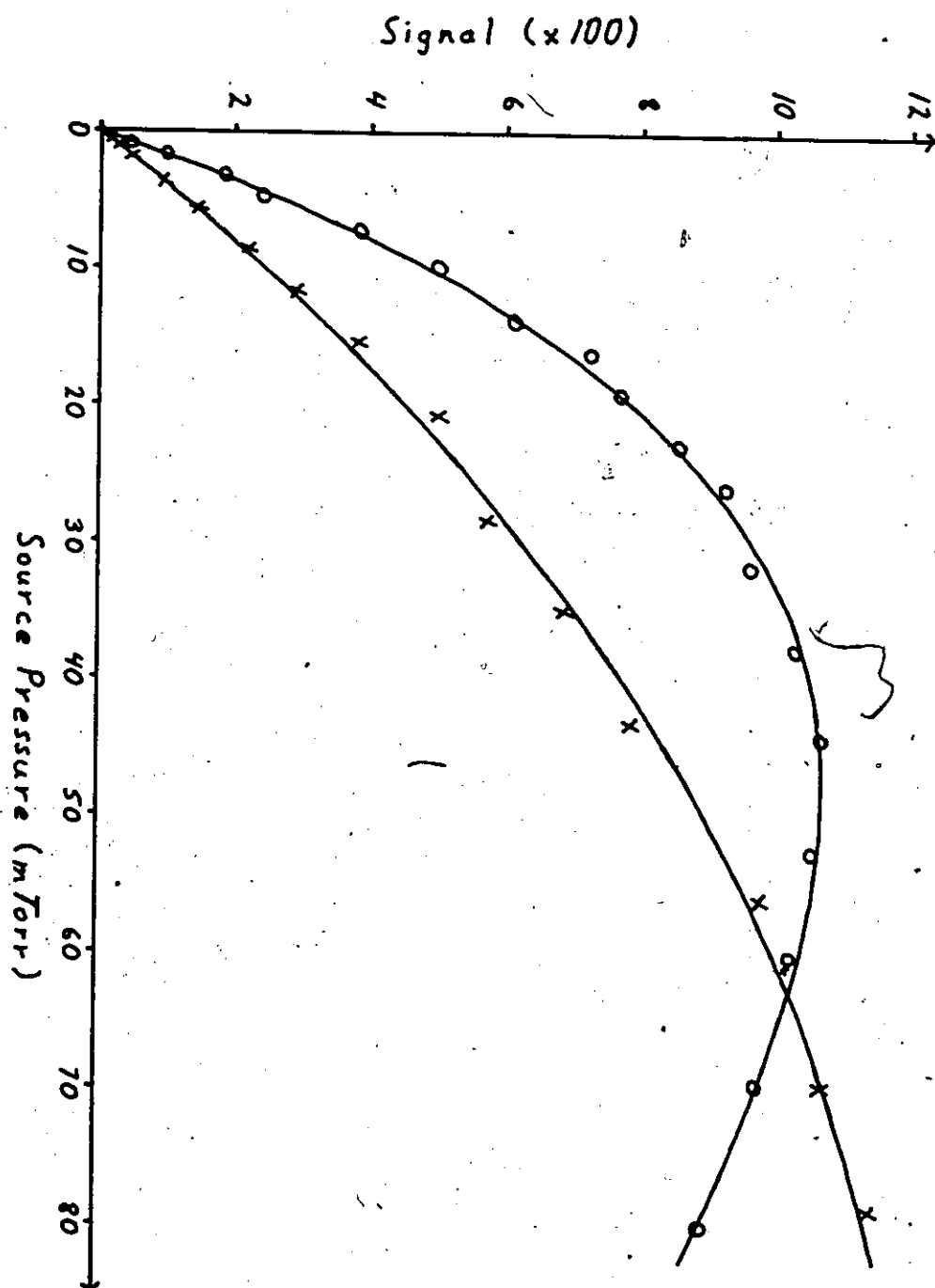
Figure 59: Intensity of the Ar$^+$ 92.0 nm emissions following
100 eV electron impact on Ar versus source
pressure (discharge source).

Signal (x 10.00) vs Source Pressure (m Torr)
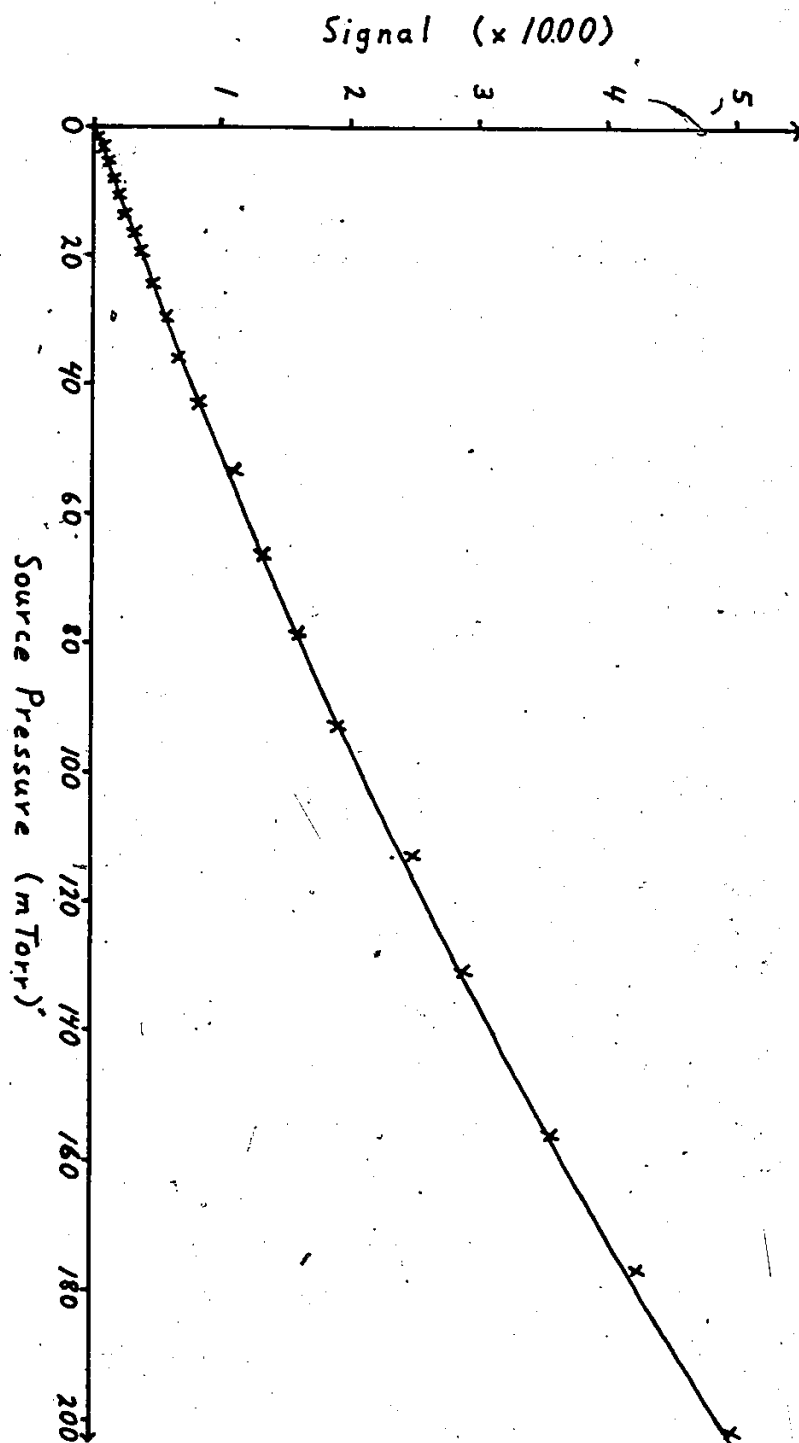
8.4   Results and Conclusions

Our present results, along with those from several other
groups are presented in Table 18.   Two sets of numbers are
given corresponding to whether Lyman beta or Lyman epsilon
is used as the reference cross section. Also shown are data
due to Ajello [5], Westerveld [99], Mentall and Mcrgan
(1976) [63], de Jongh (1971) [23], and previous work at the
University of Windsor by McConkey et al [58] and Tan et al
[85]. The data of Mentall and Morgan was originally normal-
ized to the NI 120 nm emission cross section following elec-
tron impact of Mumma and Ziff (1971) [68]. In order to com-
pare their cross section with our's we have renormalized
their cross section to our value for the NI 120 nm emission
cross section (see Chapter 6).   Similarly we have renormal-
ized the data of Ajello from his H_2 Lyman alpha emission
cross section to our present emission cross section (see
Chapter 7).

Our results compare favourably with those of Westerveld,
Mentall and Morgan, McConkey and Donaldson, and de Jongh for
the argon resonance lines.   However,   for the argcr ior
lines, we only agree with the results of Westerveld. We are
much higher than all the other results.   One reason for the
discrepancy,   at least with respect to Morgan and Mentall,
and Ajello,   may be due to systematic problems where they
extend the detection efficiency of their monochromators to
lower wavelengths.   At the same time, the variance may be

due to systematic problems of our own. For example, our
ratio of the two argon ion cross sections is definitely
greater than the others. It may be that this is due to the
flatness of the detection efficiency curve below 95 nm. If
the curve was to continue increasing, then our ratio would
be reduced.

Our results are preliminary in nature and require addi-
tional measurements in order to verify our results and the
method. In order to remove some of the uncertainty in the
shape of the detection efficiency below 95 nm, we intend to
extend the molecular branching ratio technique. This
requires the inclusion of additional molecular bands into
our synthetic model.

TABLE 19

Argon ion and resonance emission cross sections
for 200 eV electron impact

Emission Cross Sections ($\times 10^{-18}$ cm^2)

Emission	Present Results Reference Line		Present Results Average	(a)	(b)	(c)	(d)	(e)
	Ly β	Ly ε	Average					
Ar$^+$ 92.0 nm	5.1 ± 8%	6.0 ± 10%	5.6	2.06	2.62	3.7	5.5	-
Ar$^+$ 93.2 nm	2.1 ± 8%	2.5 ± 10%	2.3	1.17	1.26	1.9	2.75	-
Ar 104.8 nm	11.8 ± 10%	13.8 ± 12%	12.8	14.6	10.6	16.0	-	16.5
Ar 106.7 nm	5.1 ± 13%	5.9 ± 14%	5.5	5.74	4.30	6.3	-	6.5

(a) Mentall and Morgan [63]. They normalized their cross sections to the NI 120 nm emission cross section of Mumma and Zipf [68]. We have renormalized their values using our NI 120 nm emission cross section (see Chapter 6). The correction factor is 0.58.

(b) Ajello (private communication). Normalized to our H$_2$ Ly α emission cross section.

(c) McConkey and Donaldson [58], Ar, and Tan et al [85], Ar.

(d) Westerveld (private communication).

(e) de Jongh (unpublished Ph.D. thesis) [23].

Appendix A

GAS FLOW: DETERMINATION OF MOLECULAR DIAMETERS

NON-RESONANCE EMISSIONS

Using results from Chapter 2, it is possible to determine the molecular-viscous intersection pressure from our plots of signal versus driving pressure (see Chapter 5 for examples) for different gases and sources. From determinations of the molecular-viscous intersection pressure for two different gases, it is possible to determine the relative molecular diameters for the gases. The molecular diameters can be made absolute if a standard is assumed. For the two different gases, their respective signals can be expressed by

$$S_1(P,\lambda) = S_1(\lambda) \, f(\overline{P}, \overline{P}_{i1}) \qquad (A.1a)$$

$$S_2(P,\lambda) = S_2(\lambda) \, f(\overline{P}, \overline{P}_{i2}) \qquad (A.1b)$$

If the outlet pressure is much smaller than the inlet pressure equations (A.1) can be written as

$$S_1(P,\lambda) = S_1(\lambda) \, f(P/2, P_{i1}/2) \qquad (A.2a)$$

$$S_2(P,\lambda) = S_2(\lambda) \, f(P/2, P_{i2}/2) \qquad (A.2b)$$

- 191 -

Performing a least squares fit of the appropriate equation
to our plots we can determine the scale factors, S, and the
molecular-viscous intersection pressure, $\overline{P}_i$.

Using equation (56) from Chapter 2 it is possible to
determine either the molecular-viscous intersection pressure
for a source, or the molecular diameter of the gas under
study, given a standard. If no standard is available only
relative values are obtainable unless the diameter of the
source, D, can be determined. Thus for two different gases
the following ratio can be considered.

$$\overline{P}_{i1} D = 3.1 \times 10^{-19} \ T / \xi_1^2 \qquad \text{Torr-cm} \qquad (A.4a)$$

and
$$\overline{P}_{i2} D = 3.1 \times 10^{-19} \ T / \xi_2^2 \qquad \text{Torr-cm} \qquad (A.4b)$$

$$\frac{P_{i1}}{P_{i2}} = \frac{T_1}{T_2} \left(\frac{\xi_2}{\xi_1} \right)^2 \qquad (A.5)$$

If the gases are studied at the same temperature $(T_1 = T_2)$
then

$$\frac{P_{i1}}{P_{i2}} = \left(\frac{\xi_2}{\xi_1} \right)^2 \qquad (A.6)$$

Values which we have determined from our plots using the
above equations are given in the following tables. One
should also note, that the ratio $S_1(\lambda)/S_2(\lambda)$ is related to
the ratio of the respective effective cross sections.

TABLE 20

Molecular data for Chapters 5 and 6

Molecule (Line)	Theoretical		Experimental	
	Diameter[a] $(x\ 10^{-8} cm)$	P_i (mTorr)	Diameter $(x\ 10^{-8} cm)$	P_i (mTorr)
Ar (ArII 92.0 nm)	3.64	127.4	3.63 $\pm$ 3.7%	127.9 $\pm$ 4.0%
Ar (ArII 93.2 nm)	3.64	127.4	3.65 $\pm$ 4.3%	126.6 $\pm$ 5.0%
Ar[b] (Average)	3.64	127.4	3.64	127.4 $\pm$ 3.3%
H_2 (Lyman α)	2.74	224.8	2.73 $\pm$ 6.4%	226.0 $\pm$ 8.4%
SF_6 (FI 95.6 nm)	?		5.77 $\pm$ 3.7%	50.76 $\pm$ 4.0%
N_2 (NI 120.0 nm)	3.75	120.0	3.59 $\pm$ 12.3%	133 $\pm$ 17%
He	2.18	355.2	-	-
Ne	2.59	251.6	-	-

(a) Values for the diameters are taken from Kennard [44].

(b) The average of the two ArII results is used as the standard.

TABLE 21

Molecular data for Chapters 7 and 8

Molecule (Line)	Theoretical		Experimental	
	Diameter $(x\ 10^{-8} cm)$	P_i (mTorr)	Diameter $(x\ 10^{-8} cm)$	P_i (mTorr)
$Ar^{(c)}$ (ArII 92.0 nm)	$3.64^{(a)}$	265.9	3.64	265.9 ± 7.9%
H_2 (Lyman α)	$2.74^{(a)}$	469.3	–	–
He	$2.18^{(a)}$	741.2	–	–
H	$1.06^{(b)}$	3136	–.	–

(a) Values for the diameters are taken from Kennard [44].

(b) Diameter of first Bohr orbit.

(c) ArII is used as the standard.

Appendix B

GAS FLOW: TRAPPING MODEL
RESONANCE EMISSIONS

B.1   Development

This appendix deals with a procedure for applying a correction due to the non-linear effect which resonance trapping has on the detection of resonance emission as a function of the target number density. The method also provides a means by which relative oscillator strengths can be determined.

The system to be modelled consists of a monoenergetic electron beam impacting a target gas which subsequently emits radiation.   The radiation is detected a distance, L, in the z-direction, from the interaction region.

In order to derive an analytical expression, four assumptions are made.

I. the system is in equilibrium

II. the emitted radiation is weak $(B_{ij}\bar{W}_{ji}/A_{ij} << 1)$

III. the initial light production process can be considered separately from the trapping mechanism

IV. the spatial distribution of the gas beam is identical for all gases

For a gas target composed of similar atoms with m quantum states, the rate at which the number density of atoms in state r, N_r, changes due to an incident light beam is given by (see Loudon [54])

$$\frac{dN_r}{dt} = \sum_{i=1}^{r-1} N_i B_{ir} \overline{W}_{ri} + \sum_{j=r+1}^{m} N_j (A_{jr} + B_{jr} \overline{W}_{jr})$$

$$- \sum_{k=1}^{r-1} N_r (A_{rk} + B_{rk} \overline{W}_{rk}) - \sum_{l=r+1}^{m} N_r B_{rl} \overline{W}_{lr} \qquad \text{(A2.1a)}$$

$$= 0 \quad \text{for all } r \text{ (steady-state condition)} \qquad \text{(A2.1b)}$$

where $\overline{W}_{ij}$ is the energy density corresponding to radiation of wavelength $v_{ij} = (E_i - E_j)/h$, and A and B are the Einstein coefficients. The terms on the right-hand side correspond to excitation to state r by the radiation field, cascade into state r, decay out of state r, and excitation out of state r by the radiation field.

Under steady-state conditions the following equations are valid.

$$\frac{N_i}{N_j} = \frac{B_{ji} \overline{W}_{ji}}{A_{ij} + B_{ij} \overline{W}_{ji}} \qquad i > j \qquad \text{(A2.2)}$$

and

$$N(P;z) = \sum_i N_i (P;z) \qquad \text{(A2.3)}$$

where N is the total number density of atoms and is a function of the driving pressure of the source, P, and is a function of position. For simplicity of notation these dependences will not be explicitly shown. That equation

(A2.2) is a solution to equation (A2.1) can be checked by substitution.

Under steady-state conditions, the rate at which energy of frequency w_{ts} is lost from the radiation field, is given by $(t > s)$

$$\frac{\partial W_{st}}{\partial t} = \frac{\partial I_{st}}{\partial z} = -N_t \hbar w_{ts} G(w_{ts})[\sum_{i=1}^{t-1} A_{ti} + \sum_{\substack{j=1 \\ j \neq s}}^{t-1} B_{tj} \overline{W}_{jt}] \quad (A2.4)$$

where I is the radiant energy crossing a unit area per second. It is proportional to the signal measured by a detector and $G(w)$ is the line shape for absorption. The first term corresponds to loss through spontaneous decay while the second term corresponds to loss through stimulated emission. Multiplying equation (A2.4) by N_s/N_t and using equation (A2.2) gives

$$\frac{\partial I_{st}}{\partial z} = \frac{-N_s \hbar w_{ts} B_{st} \overline{W}_{st} G(w_{ts})}{A_{ts} + B_{ts} \overline{W}_{st}}[\sum_{i=1}^{t-1} A_{ti} + \sum_{\substack{j=1 \\ j \neq s}}^{t-1} B_{tj} \overline{W}_{jt}] \quad (A2.5a)$$

$$= \frac{-N_s \hbar w_{ts} B_{st} \overline{W}_{st} G(w_{ts}) P_{st}}{(1 + B_{ts} \overline{W}_{st}/A_{ts})} \quad (A2.5b)$$

where
$$P_{st} = 1 + \sum_{j=1}^{t-1} (1 + B_{tj} \overline{W}_{jt}/A_{tj}) A_{tj}/A_{ts} \quad (A2.6)$$

For weak light sources equation (A2.5) can be simplified to

$$\frac{\partial I_{st}}{\partial z} = -N_s \, h w_{ts} \, B_{st} \, \bar{w}_{st} \, G(w_{ts}) \sum_{j=1}^{t-1} A_{tj}/A_{ts} \tag{A2.7a}$$

$$= -N_s \, h w_{ts} \, B_{st} \, \bar{w}_{st} \, G(w_{ts}) \cdot F_{st} \tag{A2.7b}$$

$$\text{where} \quad F_{st} = \sum_{j=1}^{t-1} A_{tj}/A_{ts} \tag{A2.8}$$

Using the following two relations

$$\bar{w} = I/c \tag{A2.9}$$

and

$$h w_{ts} \, B_{st} = 6.6702 \times 10^{15} \, \pi c f_{st}/\eta \tag{A2.10}$$

where c is the speed of light, η the index of refraction, and f_{st} the absorption oscillator strength, equation (A2.7) can be expressed as

$$\frac{\partial I_{st}}{\partial z} = -6.6702 \times 10^{15} \, \frac{\pi \, N_s}{\eta} \, G(w_{ts}) F_{st} \, f_{st} \, I_{st} \tag{A2.11a}$$

$$= -K_{st} \, N_s \, I_{st} \tag{A2.11b}$$

where

$$K_{st} = 6.6702 \times 10^{15} \, \frac{\pi \, G(w_{ts}) F_{st} \, f_{st}}{\eta} \tag{A2.12}$$

For resonance radiation, $s=1$ where 1 represents the ground state of the atom, equations (A2.11) to (A2.12) become

$$\frac{\partial I_{1t}}{\partial z} = -K_{1t} N_1 I_{1t}$$

(A2.13)

where

$$K_{1t} = 6.6702 \times 10^{15} \frac{\pi G(w_{t1}) P_{1t} f_{1t}}{\eta}$$

(A2.14)

As a first approximation the line shape for absorption can be assumed to be Doppler-broadened. We will also assume that the gas is governed by a Maxwell-Boltzmann distribution. Therefore

$$G(w) = [2\pi\delta^2]^{-\frac{1}{2}} \exp\{-(w - w_0)^2/2\delta^2\}$$

(A2.15)

where

$$\delta^2 = w_0^2 kT/Mc^2$$

(A2.16)

Making the further approximation $(w = w_0)$, $G(w)$ can be written as

$$G(w) = \{2\pi\delta^2\}^{-\frac{1}{2}}$$

(A2.17)

This assumption corresponds to assuming that the incident radiation is a delta function. Due to our use of gas beams it is very difficult to know the exact form of both the emission and absorption line shapes. However, the above approximation gives acceptable results. Using (A2.17) our expression for K becomes

$$K_{1t} = 6.6702 \times 10^{15} \frac{\pi P_{1t} f_{1t}}{\eta (2\pi\delta^2)^{\frac{1}{2}}}$$

(A2.18)

Since our source outputs atoms in their ground state an expression for N_1 which is a function of the pressure, P, and the distance from the interaction region, z, is needed. Using results from Chapter 2, $N(P,z)$, can be expressed in terms of the number density at the interaction region (target), $N_1(P)$ and the conductance, $C(z)$, between the interaction region and the point z. Thus

$$N_1(P;z) = N_1(P) \frac{C(z)}{C(z) + vA} \qquad (A2.19)$$

where v is the flow velocity, and A is an element of area at z. Assuming molecular flow between the target and point z, one derives

$$N_1(P;z) = N_1(P) \frac{G(z)}{G(z) + 1.128(2k)A} \qquad (A2.20a)$$

$$= N_1(P)\, g(z) \qquad (A2.20b)$$

where $g(z)$ gives the functional variation with respect to z and is gas independent. Naturally $N(P;z)$ will depend on the gas source and experimental geometry. Substituting equation (A2.20b) into equation (A2.13) gives

$$\frac{dI_{1t}}{I_{1t}} = - K_{1t} N_1(P)\, g(z)\, dz \qquad (A2.21)$$

Integrating equation (A2.21) gives

$$\ln(I_{1t}/I_{1t}^{o}) = -K_{1t} N_1 (P) \; G(L) \qquad (A2.22a)$$

or

$$I_{1t} (P) = I_{1t}^{o} (P) \; \exp(-K_{1t} N_1(P) G(L)) \qquad (A2.22b)$$

where

$$G(L) = \int_{0}^{L} g(z) \; dz \qquad (A2.23)$$

Using equation (61) from Chapter 2, the exponent can be expressed as

$$K_{1t} N_1 (P) G(L) = K_{1t} G(L) H \; f(\overline{P},\overline{P}_i)/kT \qquad (A2.24a)$$

$$= \alpha_{1t} f(\overline{P},\overline{P}_i) T_r/T \qquad (A2.24b)$$

where

and

$$\alpha_{1t} = K_{1t} G(L) H/kT_r \qquad (A2.25)$$

$$I_{1t} (P) = I_{1t}^{o} (P) \exp(-\alpha_{1t} f(\overline{P},\overline{P}_i) T_r/T) \qquad (A2.26)$$

T_r is a reference temperature (for example room temperature) and α_{1t} will be called the absorption coefficient. Note that it is independent of both pressure and temperature. When T equals the the reference temperature, T_r, equation (A2.26) is simplified. For the remainder of this discussion this equality will be assumed as this was always the case in our experiments. Thus, equation (A2.26) becomes

$$I_{1t} (P) = I_{1t}^{o} (P) \exp(-\alpha_{1t} f(\overline{P},\overline{P}_i)) \qquad (A2.27)$$

As I is proportional to the detected signal, S, we have

$$S_{1t} (P,\lambda) = S_{1t}^{o} (P,\lambda) \exp(-\alpha_{1t} f(\overline{P},\overline{P}_i)) \qquad (A2.28)$$

If α_{1t} equals zero there is no resonance trapping and

$$S_{1t}(P,\lambda) = S_{1t}^{O}(P,\lambda) \qquad\qquad (A2.29)$$

$$= S_{1t}^{O}(\lambda)\ f(\overline{P},\overline{P}_i) \qquad\qquad (A2.30)$$

where $S_{1t}(\lambda)$ is the constant of proportionality for the emission. Combining the previous results we finally have

$$S_{1t}(P,\lambda) = S_{1t}^{O}(\lambda)\ f(\overline{P},\overline{P}_i)\ \exp[-\alpha_{1t}f(\overline{P},\overline{P}_i)] \qquad (A2.31a)$$

$$= S_{1t}^{O}(\lambda)\ f(\overline{P},\overline{P}_i)\ D(1t,\overline{P},\overline{P}_i) \qquad\qquad (A2.31b)$$

where

$$D(1t,\overline{P},\overline{P}_i) = \exp[-\alpha_{1t}f(\overline{P},\overline{P}_i)]. \qquad\qquad (A2.32)$$

$D(1t;\overline{P},\overline{P}_i)$ is called the trapping factor. If molecular flow conditions prevail, we have the trivial result.

$$S_{1t}(P,\lambda) = S_{1t}^{O}(\lambda)\ \overline{P}\ \exp[-\alpha_{1t}\overline{P}] \qquad\qquad (A2.33)$$

B.2 Special Applications

Two applications are of special interest. The first involves determining an "unknown" trapping factor from a "known" trapping factor. From the preceding results the following relationship can be derived.

where

$$D_u(1t;\overline{P}_u,\overline{P}_{iu}) = D_r(1s,\overline{P}_r,\overline{P}_{ir})^{\gamma_{ur}(\overline{P}_u,\overline{P}_r)} \qquad (A2.34)$$

$$\gamma_{ur}(\overline{P}_u,\overline{P}_r) = \alpha_{1t}^{u}f(\overline{P}_u,\overline{P}_{iu})/\alpha_{1s}^{r}f(\overline{P}_r,\overline{P}_{ir}) \qquad (A2.35a)$$

$$= \gamma_{ur}\ f(\overline{P}_u,\overline{P}_{iu})/f(\overline{P}_r,\overline{P}_{ir}) \qquad (A2.35b)$$

and

$$\gamma_{ur} = \alpha_{1t}^{u}/\alpha_{1s}^{r} \qquad\qquad (A2.36)$$

γ_{ur} is called the trapping coefficient. Note that equation (A2.35b) reduces to γ_{ur} when molecular flow conditions prevail and equal pressures $(\bar{P}_r = \bar{P}_u)$ are used..

The second involves determining relative oscillator strengths using two known absorption coefficients. The converse is also feasible. The resultant relationship is (assuming equal temperatures)

$$\frac{\alpha_{1t}^u}{\alpha_{1s}^r} = \frac{F_{1t} f_{1t} \lambda_{1t} M_u^{\frac{1}{2}}}{F_{1s} f_{1s} \lambda_{1s} M_r^{\frac{1}{2}}} \qquad (A2.37)$$

where λ_{1t} and λ_{1s} are the corresponding wavelengths, and M_r and M_u are the corresponding atomic (molecular) masses.

Table 22 to Table 24 list results relevant to Chapters 4 to 6.

TABLE 22

Oscillator strengths, F values, trapping factors, and trapping coefficients for the helium experiment of Chapter 4.

He Line Wavelength (nm)	Absorption(a) Oscillator Strengths	F	Trapping(b) Coefficients γ	Trapping Factors P = 1.4 μTorr	Trapping Factors P = 4.9 μTorr
2p – 1s 58.4	0.2762 ± 1%	1.001	1	0.944 ± 4.3%	0.803 ± 11.2%
3p – 1s 53.7	0.0734 ± 1%	1.024	0.2500 ± 2%	0.986 ± 2.3%	0.947 ± 5.9%
4p – 1s 52.2	0.0302 ± 3%	1.035	0.1011 ± 4%	0.994 ± 1.5%	0.978 ± 3.8%
n≥5p – 1s	0.0153(c) ± 5%	1.039(c)	0.0508(c) ± 6%	0.997 ± 1.1%	0.989 ± 2.7%

(a) From National Bureau of Standards [9].

(b) $\gamma = \alpha / \alpha_{He}(2p-1s)$; α = absorption coefficient.

(c) We have used the value for n = 5.

TABLE 23

Absorption coefficients, oscillator strengths, and F values
for Chapters 5 and 6

Atom Wavelength (nm)	Absorption Oscillator Strengths NBS[a]	Experimental	F	Absorption Coefficients ($mTorr^{-1}$)
He 53.7	0.0734 ± 1%	0.078 ± 5.3%	1.024	0.0223 ± 3.8%
He[b] 58.4	0.2762 ± 1%	0.276 ± 1%	1.001	0.0843 ± 3.6%
Ne 73.6	0.162 ± 25%	0.11 ± 4.7%	1.000	0.0923 ± 2.9%
Ar 104.8	0.254 ± 20%	0.16 ± 5.2%	1.000	0.275 ± 3.7%
Ar 106.7	0.061 ± 20%	0.048 ± 5.0%	1.000	0.0825 ± 3.4%

(a) From National Bureau of Standards [9] [10].

(b) He (58.4 nm) is used as the standard.

TABLE 24

Absorption coefficients, oscillator strengths, and F values

for Chapters 7 and 8

Atom Wavelength (nm)	Absorption Oscillator Strengths		F	Absorption Coefficients $(mTorr^{-1})$
	NBS[a]	Experimental		
He[b] 58.4	0.0734 ± 1%	0.0734	1.024	0.00338 ± 14.2%
Ar 104.8	0.254 ± 20%	0.166 ± 15%	1.000	0.0425 ± 4.7%
Ar 106.7	0.061 ± 20%	0.065 ± 20%	1.000	0.0168 ± 14.3%

(a) From National Bureau of Standards [9] [10].

(b) He (58.4) is used as the standard.

Appendix C

H₂ SYNTHETIC SPECTRUM: MOLECULAR EMISSIONS

This appendix illustrates the technique which we have used to create our molecular hydrogen synthetic spectrum. Only vibrational transitions are considered. Our starting place is a paper by McConkey (1969) [57]. Accordingly, the intensity of a vibrational transition for a given band is

$$I_{v'v''} = C \ N_{v'} \ E^3_{v'v''} \ \overline{R}^2_e \ q_{v'v''} \quad \text{(photons/s)} \quad \text{(A3.1)}$$

where C is a constant, $N_{v'}$ is the population of the vibrational level v' of the upper electronic state, v'' is the vibrational level of the lower electronic state, $E_{v'v''}$ is the energy difference between v' and v'', $\overline{R}_e$ is the average value of the electronic transition moment and $q_{v'v''}$ is the Franck-Condon factor. As $\overline{R}^2_e$ varies slowly within a given band system, it may be effectively regarded as a constant. Consequently, we may rewrite equation (A3.1) as the proportionality

$$I_{v'v''} \propto N_{v'} \ q_{v'v''} / \lambda^3 \quad \text{(A3.2)}$$

where λ is the wavelength of the v', v'' transition.

Likewise, the rate of excitation by electron impact of level v' from level v of the ground state of the molecule is given by

$$R_{vv'} \propto i \, N_v \, q_{vv'} \, G^2(v,v') \qquad \text{(molecules/s)} \qquad \text{(A3.3)}$$

where i is the electron current, N_v is the ground state population in level v, and $G^2(v,v')$ is a further electronic factor which may vary slowly with internuclear separation provided the electron energy is well above the threshold for the process (see Nicholls [69] for more details). Assuming it to be constant for a given band, and assuming that electron impact excitation and radiative decay are the dominant processes involving the v' level, then in equilibrium, the population of the v' level is given by

$$N_{v'} \propto i \, N_v \, q_{vv'} \qquad \qquad \text{(A3.4)}$$

Combining equations (A3.2) and (A3.3) we have

$$I_{v'v''} \propto i \, N_v \, q_{vv'} q_{v'v''}/\lambda^3 \qquad \qquad \text{(A3.5)}$$

In general, the molecules can be in more than one level of the ground state, thus equation (A3.5) is a sum. In other words

$$I_{v'v''} \propto \frac{q_{v'v''}}{\lambda^3} \sum_v N_v \, q_{vv'} \qquad \qquad \text{(A3.6a)}$$

and

$$N_{v'} \propto i \sum_v N_v \, q_{vv'} \qquad \qquad \text{(A3.6b)}$$

If equation (A3.6b) is written in terms of a probability, then

$$N_{v'} = \sum_v N_v P(v,v') \qquad (A3.7)$$

where

$$P(v,v') = q_{vv'} / \sum_{v'} q_{vv'} \qquad (A3.8)$$

$P(v,v')$ is the probability that a molecule in level v will end up in level v'. Thus, given an initial ground state level distribution $\{N_v\}$, and the Franck-Condon factors, the population of the excited level can be calculated.

In order to put the intensities on an absolute scale, equation (A3.6a) is normalized to the total band intensity. Thus

$$I^0_{v'v''} = \frac{I_{v'v''}}{\sum_{v'v''} I_{v'v''}} = \frac{q_{v'v} N_{v'}/\lambda^3}{\sum_{v'v''} q_{v'v''} N_{v'}/\lambda^3} \qquad (A3.9)$$

In other words $I^0_{v'v''}$ is the relative intensity for a level transition within a band to that for the entire band. The sum is over all final and initial levels within the band.

We have calculated the relative intensities for both the Lyman and Werner bands for a variety of initial ground state population distributions. However, due to the temperatures at which we operate (near room temperature), no significant population of excited ground state levels is expected. At 300 K, the ratio of molecules in the first excited level (v=1) to that in the zeroth level (v=0) is 2.16×10^{-9}. Hence equations (A3.7) and (A3.8) can be simplified to

$$\text{and} \quad N_{v'} = N_0 \, P(0,v') \tag{A3.10}$$

$$P(0,v') = q_{ov'} \Big/ \sum_{v'} q_{ov'} \tag{A3.11}$$

The Franck-Condon factors can be calculated using the transition probabilities and oscillator strengths of Allison and Dalgarno (1970) [8]. The equation relating them is

$$q_{vv'} = \frac{3}{2hc} \; \frac{6.6702 \times 10^{15}}{G} \; \frac{f^3_{vv'}}{A_{v'v}} \tag{A3.12}$$

where h is Planck's constant, c is the speed of light, $f_{vv'}$ the oscillator strength, and $A_{v'v}$ the transition probability. G is a factor which is constant within a band. It is given by the degeneracies of the electronic levels involved in the transition. The Lyman band $(B^1\Sigma_u^+ - X^1\Sigma_g^+)$ has nondegenerate upper and lower electronic states; hence G=1. The Werner band $(C^1\Pi_u^+ - X^1\Sigma_g^+)$ involves a transition from a doubly degenerate upper state to a nondegenerate lower state; thus G=2.

To obtain spectra resembling our experimental spectra it is necessary to incorporate the resolution of our monochromator. A triangular instrumental transmission function is used for each vibrational transition within a specified wavelength range. Figure 60 shows an example of our synthetic spectrum from 100 to 130 nm using a resolution of 0.34 nm full-width half maximum. With our gratings this corresponds to slit widths of 0.2 mm. The top figure shows the Werner

band, the middle figure shows the Lyman band, and the bottom
figure shows their sum. The figure also shows the position
of the Lyman alpha wavelength. A straight sum is used due
to the near equality between the total Lyman band emission
cross section and the total Werner band emission cross sec-
tion [6]. According to Ajello et al (1985) [6], these cross
sections are 2.67 x 10^{-17} cm^2 and 2.78 x 10^{-17} cm^2 respec-
tively.

Figure 60: Sample synthetic H_2 spectra with 0.34 nm
resolution. The spectra depict the Werner
band, the Lyman band, and their sum.
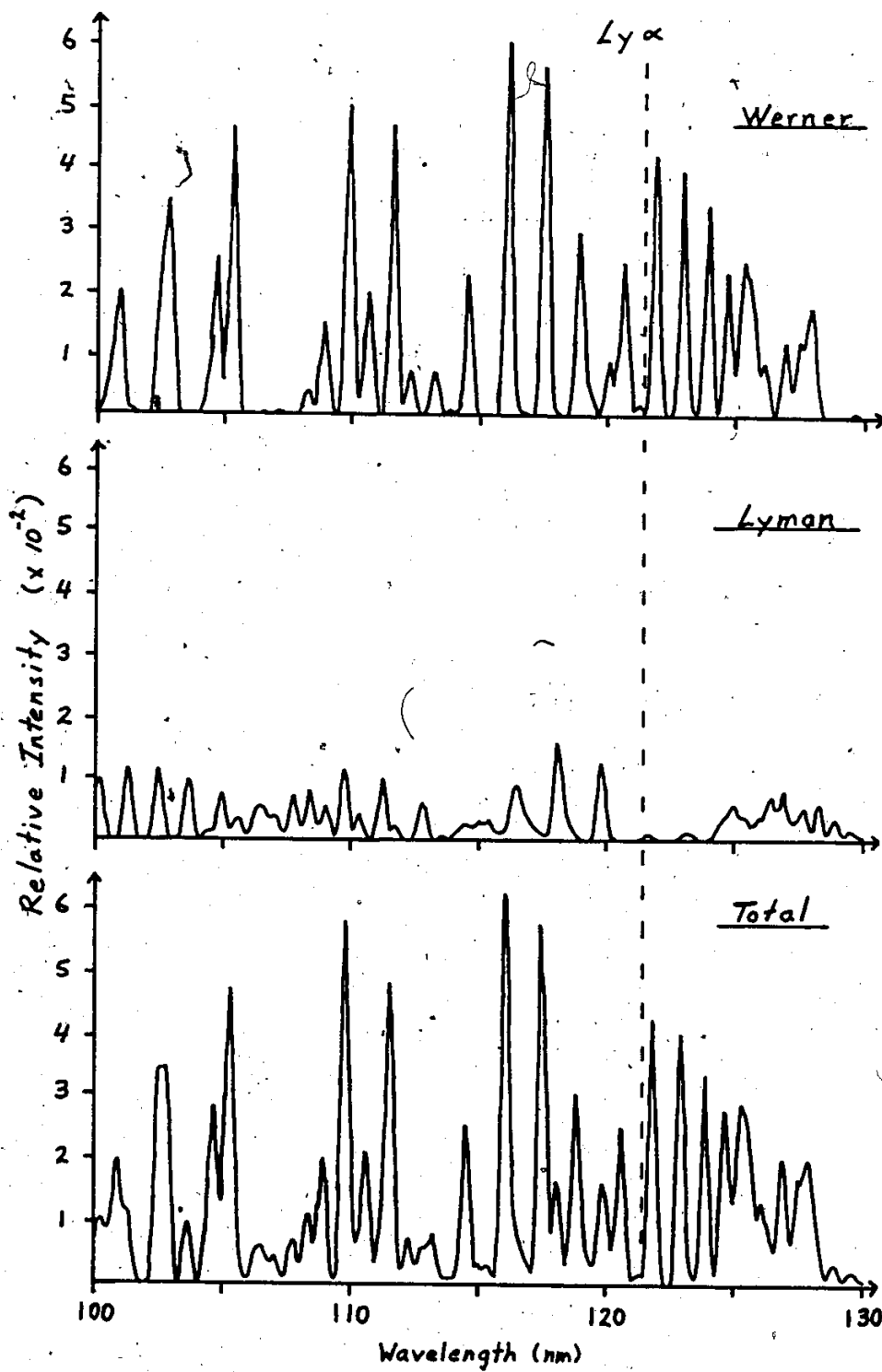
Appendix D

BRANCHING RATIO AND CASCADE CALCULATIONS.

This appendix describes the method used to calculate the branching ratios and cascade contributions for the atomic hydrogen Lyman series.

The branching ratios are calculated using transition probabilities (Einstein A coefficient) from the National Bureau of Standards [9] and equation (7a) of Chapter 2. For convenience it is presented again.

$$B(n'l'nl) = A(n'l'nl) / \sum_{n''l''} A(n'l'n''l'') \qquad (A4.1)$$

$B(n'l'nl)$ is the branching ratio and $A(n'l'nl)$ is the transition probability for the $n'l' \rightarrow nl$ transition in atomic hydrogen.

The apparent cross section (cascade included) for a Lyman series emission can be given by

$$Q'(np \rightarrow 1s) = B(np1s) [Q(np1s) + Q_c(np)] \qquad (A4.2)$$

where $Q(np1s)$ is the total excitation cross section and $Q_c(np)$ is the amount of cascade into the state np from higher states. It can be expressed by the following recursive relation in which normal spectroscopic notation is used.

$$Q_c(n_0 \ell_0) = \sum_{n_1=n_0+1}^{\infty} \sum_{\substack{\ell_1=\ell_0-1 \\ \ell_1 \neq 1 \\ \ell_1 \geq 0}}^{\ell_0+1} B(n_1\ell_1 n_0\ell_0)[Q(n_1\ell_1 10) +$$

$$\sum_{n_2=n_1+1}^{\infty} \sum_{\substack{\ell_2=\ell_1-1 \\ \ell_2 \neq 1 \\ \ell_2 \geq 0}}^{\ell_1+1} B(n_2\ell_2 n_1\ell_1)[Q(n_2\ell_2 10) +$$

$$\dots\dots\dots\dots\dots]] \qquad\qquad (A4.3)$$

While the sequence is infinite, only a finite number of states is used, because the total excitation cross sections for higher states fall off approximately as n^{-3}. Each successive term is determined by increasing the indices of the previous term by 1.

Cascade contributions for 200 eV electron impact can be estimated by using the Born approximation cross sections of Vainshtein [91] (or see Moiseiwitsch [64]) for the total excitation cross sections. Table 25 lists these cross sections along with their branching ratios and cascade percentages. Note that we have only included terms up to n=6. The cascade percentage is defined to be

$$\% \text{ cascade} = Q_c(np)/Q(np1s) \qquad\qquad (A4.4)$$

Table 25

Cross sections used for cascade calculations

Born approximation total excitation cross sections (Vainshtein, 1965) for 200 eV electron impact

Transition	Cross Section (x 10^{-18}cm^2)
H(1s --> 2p)	41.6
H(1s --> 3s)	0.51
H(1s --> 3p)	7.10
H(1s --> 3d)	0.38
H(1s --> 4s)	0.19
H(1s --> 4p)	2.52
H(1s --> 4d)	0.18
H(1s --> 5s)	0.09
H(1s --> 5p)	1.20
H(1s --> 5d)	0.09
H(1s --> 6s)	0.05
H(1s --> 6p)	0.66
H(1s --> 6d)	0.06

BIBLIOGRAPHY

1. Aarts,J.F.M. and de Heer,F.J., 1968, J. Optical Soc. of America 58 1666.

2. Aarts,J.F.M. and de Heer,F.J., 1971, Physica (Utrecht) 52 45.

3. Aarts,J.F.M. and de Heer,F.J., 1970, J. Chem. Phys. 52 5354.

4. Ajello,J.M. and Shemansky,D.E., 1985, Abstracts 14th I.C.P.E.A.C., Palo Alto, p.248.

5. Ajello,J.M.,1984, private communication.

6. Ajello,J.M. and Shemansky,D.E., 1985, J. Geophysical Res. 90 9845-9861.

7. Ajello, J.M., 1970, J. Chem. Phys. 53 1156.

8. Allison,A.C. and Dalgarno,A., 1970, Atomic Data 1 289-304.

9. Atomic Transition Probabilities, 1966, Natl. Stand. Ref. Data Ser., Natl. Bur. Stand. 1.

10. Atomic Transition Probabilities, 1969, Natl. Stand. Ref. Data Ser., Natl. Bur. Stand. 2.

11. Becker,K. and McConkey,J.W., 1984, Can. J. Phys. 62 1-9.

12. Becker,K., van Wijngaarden ,W. and McConkey J.W., 1983, Planet. Space Sci. 31 197-206.

13. Bethe,H.A., 1930, Ann. Phys., Lpz., 5 325.

14. Blechschmidt,B., Haensel,R., Kock,E.E., Nielsen,V. and
    Sagawa,T., 1972, Chem. Phys. Lett. 14 33.

15. Bloemen,E.W.P., Winter,H., Mark,T., Dijkkamp,D., Bar-
    rends,D. and de Heer,F.J., 1981, J. Phys. B 14 717-725.

16. Brinkman,R.T. and Trajmar,S., 1981, J. Phys. E 14 245.

17. Callaway,J. and McDowell,M.R.C., 1983, Comm. At. Mol.
    Phys. 13 19-35.

18. Carriere,J.D. and de Heer,F.J., 1972, J. Chem. Phys. 55
    2993.

19. Connolly,J.W.D. and Johnson,K.H.,1971,Chem. Phys.
    Letts. 10 616 and references therein.

20. Corr,J.J., Khakoo,M.A. and McConkey, J.W., 1986, to be
    submitted to J. Phys. B.

21. Corrigan,S.J.B., 1965, J. Chem. Phys. 43 4381-4386.

22. Dassen,H., Malcolm,I.C. and McConkey,J.W., 1977, J.
    Phys. B 10 L493-L945.

23. de Jongh,J.F., 1971, Ph.D. thesis, University of
    Utrecht, Netherlands.

24. Dibeler,V.H. and Mohler,F.L., 1949 ,J. of Res., Nat.
    Bur. of Stand. 40 25.

25. Donaldson,F.G., Hender,M.A. and McConkey,J.W., 1972, J.
    Phys. B 5 1192-1210.

26. Elenbaas,W., 1930, Z. Phys. 59 289-305.

27. Fite,W.L. and Brackmann,R.T., 1958, Phys. Rev. 112
    1151-1156.

28. Forand,J.L., Becker,K. and McConkey,J.W., 1985, J. Phys. B 18 1409-1418.

29. Forand,J.L., Becker,K. and McConkey,J.W., 1986, Can. J. Phys. 64 269-276.

30. Ganas,P.S. and Green,A.E.S., 1971, Phys. Rev. A 4 182

31. Gelius,U., 1974, J. Electron Spectrosc. Relat. Phenom. 5 985.

32. Gentieu,E.P., Feldman,P.D., and Meier,R.R., 1979, Geophys. Res. Lett. 6 325.

33. Haidt,D. and Kleinpoppen,H., 1966, Z. Phys. 196 72-76.

34. Hammond, P., 1986, University of Windsor (private communication).

35. Hay,P.J., 1977, J. Am. Chem. Soc. 99 1003.

36. Hay,P.J., 1977, J. Am. Chem. Soc. 99 1013.

37. Heddle,D.W.C. and Keesing,R.G.W., 1968, Adv. At. Mol. Phys. 4 267-298.

38. Heddle,D.W.O. and Lucas,C.B., 1963, Proc. R. Soc. A 271 129-135.

39. Houver,J.C., Fayeton,J. and Barat,M., 1974, J. Phys. B 7 1358.

40. Huffman,R.E., LeBlanc,F.J., Larrabee,J.C., and Paulsen,D.E., 1980, J. Geophys. Res. 85 2201.

41. Huschilt,J.C., Dassen,H.W. and McConkey,J.W., 1981, Can. J. Phys. 59 1893.

42. JANAF Thermochemical Tables, 2nd Ed., 1970, Natl. Stand. Ref. Data Ser., Natl. Bur. Stand. 37.

43. Kauppila,W.E., Teubner,P.J.O., Fite,W.L. and Girnius,R.J., 1971, J. Chem. Phys. 55 1670-1672.

44. Kennard,E.H. _Kinetic Theory of Gases_ New York, McGraw-Hill Book Company, Inc., 1938.

45. Lassettre,E.N. and Silverman,S.M., 1964, J. Chem. Phys. 40 1256-1261.

46. Lassettre,E.N. and Skerbele,A., 1970, J. Chem. Phys. 54, 1597-1607.

47. LaVilla,R.E., 1972, J. Chem. Phys. 57 899.

48. LaVilla,R.E. and Deslattes,R.D., 1966, J. Chem. Phys. 44 4398.

49. Lee,E.T.P. and Lin,C.C., 1965, Phys. Rev. 138 A301-304.

50. Ligtenberg,R.C.G., McPherson,A., Rouze,N., Westerveld,W.B. and Risley,J.S., 1985, Bull. Amer. Phys. Soc. 30 881.

51. Ligtenberg,R.C.G., McPherson,A., Rouze,N., Westerveld,W.B. and Risley,J.S., Abstracts 14th I.C.P.E.A.C., Palo Alto, p.276.

52. Liu,T.K., Moe,G. and Duncan,A.B.F., 1951, J. Chem. Phys. 19 71.

53. Long,R.L., Cox,D.M. and Smith,S.J., 1968, J. Res. Natl. Bur. Stand. 72A 521-535.

54. Loudon,R. _The Quantum Theory of Light_ Oxford, Oxford University Press, 1979.

55. MacAlpine,W.W. and Schildkne███████, 1959, Proc. IRE 2099.

56. Malcolm,I.C., Dassen,H.W. and McConkey,J.W., 1979, J. Phys. B 12 1003-1017.

57. McConkey,J.W., 1969, J. Optical Soc. of America 59 110.

58. McConkey,J.W. and Donaldson,F.G., 1973, Can. J. Phys. 51 914.

59. McConkey,J.W. and Donaldson,F.G., 1972, Can. J. Phys. 50 2211-2216.

60. McGowan,J.W. and Williams,J.F., 1969, 6th Interr. Conf. Phys. Electron Atomic Collisions, Boston, Mass., p. 431.

61. McGuire,E.J., 1971, Phys. Rev. A 3 267

62. McPherson,A., Rouze,N., Westerveld,W.B. and Risley,J.S., 1986, Appl. Opt. 25 298-310.

63. Mentall,J.E. and Morgan,H.D., 1976, Phys. Rev. A 14 954

64. Moiseiwitsch,B.L. and Smith,S.J., 1968, Rev. of Mod. Phys. 40 238-352.

65. Moustafa Moussa,H.R. and de Heer,F.J., 1967, Physica 36 646-654.

66. Mumma,M. and Zipf,E.C., 1970, J. Chem Phys. 53 1156.

67. Mumma,M. and Zipf,E.C., 1971, J. Chem. Phys. 55 1661-1669.

68. Mumma,M.J. and Zipf,E.C., 1971, J. Chem. Phys. 55 5582-5588.

69. Nicholls,R.W., 1962, Quant. Spectry. Radiat. Transfer 2 433.

70. Nostrand,E.D. and Duncan,A.B.F., 1954, J. Am. Chem. Soc. 76 3377.

71. Ott,W.R., Kauppila,W.E. and Fite,W.L., 1970, Phys. Rev. A 1 1099.

72. Falenius,H.P., 1969, Ark. Fizs. 39 15.

73. Percival,I.C. and Seaton,M.J., 1958, Phil. Trans. R. Soc. 251 113-138.

74. Pettersson,J.E., 1983, Physica Scripta 28 421.

75. Potts,A.W., Lempka,H.J., Streets,D.G. and Price,W.C., 1970, Philos. Trans. R. Soc. London, Ser. A, 268 59.

76. Pullen,B.P. and Stockdale,J.A.D., 1976, Inter. J. of Mass Spectrometry and Ion Phys. 19 35-42.

77. Roth, A. Vacuum Technology Amsterdam, North Holland, 1982.

78. Shemansky,D.E., Ajello,J.M. and Hall,D.T., 1985, Astrophys. J. 296 765-773.

79. Shemansky,D.E., Ajello,J.M., Hall,D.T. and Franklin,B., 1984, Astrophys. J. 296 774-783.

80. Siegbahn,K. et. al. ESCA Applied to Free Molecules Amsterdam, North Holland, 1969.

81. Simpson,J.A., Kuyatt,C.E. and Mielczarek,S.R., 1966, J. Chem. Phys. 44 4403.

82. Slevin,J.A. and Stirling,W.D., 1981, Rev. Sci. Instrum. 52 1780-1782.

83. Striganov,A.R. and Sventitskii,N.S. Tables of Spectral Lines of Neutral and Ionized Atoms New York, Plenum, 1968.

84. Sutton,J.P. and Kay,B.E., 1974, Phys. Rev. A 9 697-703.

85. Tan,K.H., Donaldson,F.G. and McConkey,J.W., 1974, Can.
    J. Phys. 52 786.

86. Tang,R. and Callaway,J., May, 1986, private communica-
    tion.

87. Taylor,J.R. Scattering Theory: The Quantum Theory of
    Nonrelativistic Collisions Malabar, Florida, Robert E.
    Krieger Publishing Company, Inc., 1983.

88. Timothy,J.G. and Lapson,L.E., 1974, Applied Optics 13
    1427-1430.

89. Tonnies,J.P., Welz,W., and Wolf,G., 1974, J. Chem.
    Phys. 61 2461.

90. Trajmar,S. and Chutjian,A., 1977, J. Phys. B 10 2943.

91. Vainshtein,L.A., 1965, Opt. Spectrosc. USSR (Eng.
    transl.) 18 538.

92. van Eck,J. and de Jongh,J.P., 1970, Physica 47 141-158.

93. van Wyngaarden,W.L. and Walters,H.R.J., 1986, J. Phys.
    B 19 L53-58.

94. van Wyngaarden,W.L. and Walters,H.R.J., 1986, J. Phys.
    B 19 929-968.

95. van Zyl,B., Gealy,M.W. and Neumann,H., 1985, Phys.
    Rev. A 31 2922-2931.

96. Viennet,J., Petit,P., and Audoin,C., 1973, J. Phys. E 6
    257-261.

97. Vinogradov,A.S. and Zimkina,T.M., 1972, Opt.
    Spectr.(Eng. Tran.) 32 17.

98. Weller,C.S. and Young,J.M., 1970, Appl. Opt. 9 505-506.

99. Westerveld,W.B. (private communication).

100. Westerveld,W.B., Heideman,H.E. and van Eck,J., 1979, J. Phys. B 12 115-135.

101. Williams,J.F., 1976, J. Phys. B 9 1519-1527.

102. Williams,J.F., 1981, J. Phys. B 14 1197-1217.

103. Wood,P.J. and Wise,H., 1962, J. Phys. Chem. 66 1049.

104. Woolsey,J.M., Forand,J.L. and McConkey,J.W., 1986, J. Phys. B 19 L493-L497.

105. Zimkina,T.M. and Fomichev,V.A., 1966, Sov. Phys. Dokl.(Eng. Tran.) 11 726.

PUBLICATIONS

1. Woolsey,J.M., Forand,J.L. and McConkey,J.W. Lyman-Alpha Revisited 1986, J. Phys. B. 19 L493-L497.

2. Forand,J.L., Becker,K. and McConkey,J.W. Dissociative Excitation of SF_6 by Controlled Electron Impact 1986, Can. J. Phys. 64 269-276.

3. Khakoo,M.A., Becker,K., Forand,J.L. and McConkey,J.W. Circular Polarization Study of He 2^1P Excitation using Electron-Photon Coincidence Techniques 1986, J. Phys B. 19 L209-213.

4. Forand,J.L., Becker,K. and McConkey,J.W. Absolute Electron Impact Emission Cross Section of the He^+ 2^2P --> 1^2S Line at 304 A Produced by Simultaneous Ionization-Excitation 1985, J. Phys. B 18 1409-1418.

5. Forand,J.L., Mitchell,J.B.A. and McGowan,J.W. Triatomic Molecular Dissociation: A Method for Measuring Individual Decay Channel Cross Sections 1985, J. Phys. B 18 623-626.

6. Becker,K., Forand,J.L., Zetner,P.W. and McConkey,J.W. Dipole and Non-Dipole Excitation in Collisions of Low Energy Electrons with Diatomic Molecules 1984, J. Phys. B 17 L915-919.

7. Mitchell,J.E.A., Ng,C.T., Forand,J.L., Janssen,E. and
    McGowan,J.W. Total Cross-Sections for the Dissociative
    Recombination of H_3^+, HD_2^+ and D_3^+ 1984, J. Phys. E 19
    I909-913.

8. Mitchell,J.B.A., Ng,C.T., Forand,J.L., Levac,D.F.,
    Mitchell,R.E., Sen,A., Miko,D.B. and McGowan,J.E. Die-
    lectronic Recombination Cross Section Measurement for
    C^+ Ions 1983, Phys. Rev. Lett. 50 335-338.

9. Mitchell,J.B.A., Forand,J.L., Ng,C.T., Levac,D.F.,
    Mitchell,R.E., Mul,P.M., Claeys,W., Sen,A. and McGow-
    an,J.W. Measurement of the Branching Ratio for the
    Dissociative Recombination of H_3^+ + e 1983, Phys. Rev.
    Lett. 51 885-888.

10. Forand,J.L. A First Determination of the H_3^+ Branching
    Ratios 1983, M.Sc. thesis, Univ. of Western Ontario.

VITA AUCTORIS

I was born on the 24th of January, 1959, in the city of
Halifax, Nova Scotia. Until 1963 our family resided in
either Sydney or Halifax, Nova Scotia. In 1963 we were
transferred to the Canadian Armed Forces base near Metz,
France. During the year which we spent in Metz, I attended
french kindergarten. In 1964, when the base was finally
closed, we moved across the border to another military base
at Baden Soelingen, West Germany. During the four years
which we spent in the region I completed grades 1 to 4. In
1969 we returned to Canada. For the next eight years my
father was stationed in the Montreal, Quebec region. I com-
pleted grade 5 while we lived in what is now part of Lon-
gueil, but was formerly called Jacques Cartier. The remain-
der of my elementary and Quebec secondary education was
attained while we lived in the small community of Otterburn
Park on the Richelieu river. In 1976 my father was trans-
ferred to Halifax, Nova Scotia, so instead of attending a
preliminary year at Acadia University, I decided to attend
grade 12 in Halifax. After my second high school graduation
I applied to several universities in Nova Scotia and finally
accepted the offer from Dalhousie. This include an entrance
scholarship. In my third year I also recieved a general

scholarship. In the spring of 1981, I graduated with a B.Sc. with honours in physics. During the summer of 1981, I was employed by the acoustics division of NRC in Ottawa. This opportunity was possible due to an NSERC summer scholarship. In the fall of 1981 I enrolled at the University of Western Ontario. In the spring of 1983 I graduated with an M.SC. in Physics. During this period I worked under the supervision of Dr. J.W. McGowan. In March I was also awarded a Post-graduate scholarship, which I first used when I commenced my Ph.D. program, in the fall of 1983, under the supervision of Dr. J.W. McConkey at the University of Windsor.